Assimilating novel geophysical datasets into ice-sheet models: Experiments at the margins and interior of West Antarctica

Andrew Hoffman

A dissertation submitted in partial fulfillment of the
requirements for the degree of

Doctor of Philosophy

University of Washington

2023

Reading Committee:

Knut Christianson, Chair

Michelle Koutnik

Daniel Shapero

Program Authorized to Offer Degree:
Earth and Space Sciences

University of Washington

Abstract

Assimilating novel geophysical datasets into ice-sheet models: Experiments at the margins and interior of West Antarctica

Andrew Hoffman

Chair of the Supervisory Committee:
Knut Christianson
Earth and Space Sciences

This thesis uses novel remote-sensing datasets in conjunction with focused modeling efforts to contextualize present and past changes in the mechanical behavior of the West Antarctic Ice Sheet. In the second and third chapters of the thesis, we explore the controls for sliding beneath Thwaites Glacier using surface velocity and elevation time series and the first swath radar scans of the subglacial topography in the ice-sheet interior. Observations of surface velocity and surface elevation over the last 10 years reveal that a system of subglacial lakes on Thwaites Glacier filled and drained without substantially changing the traction of the glacier to the ice-sheet bed. From swath topography recovered near these lakes, we diagnose the relationship between unresolved topography and basal shear stress inferred from ice geometry and surface velocity. In the fourth chapter, we present data collected at Hercules Dome, where swath radar data reveal bedforms and landscapes consistent with a marine proximal glaciated alpine valley network. These bed features require faster flow speeds for formation than the speeds observed at Hercules Dome today and suggest Hercules Dome may have been a nucleation center for ice-sheet growth preceding glaciation. In Chapter 5, we move downstream of Hercules Dome to Conway Ridge (formerly Ridge A), which sits between the van der Veen and Mercer Ice Streams. Encoded in the layer stratigraphy at Conway Ridge are signals that suggest ice flow around Conway Ridge has slowed as the ice sheet and bed topography isostatically equilibrated. Much of this evidence is linked to

buried crevasse patterns that constrain past surface strain rates. These past surface crevasse features motivated the investigation of modern surface features and the focus of the sixth chapter concerned with crevasse area change on Thwaites Glacier.

TABLE OF CONTENTS

LIST OF FIGURES

LIST OF TABLES

ACKNOWLEDGMENTS

I wish to thank my family, specifically my mom and dad for supporting me through this Ph.D. I also thank my friends in the graduate program at the University of Washington and folks at the British Antarctic Survey, who welcomed me into their group. Finally, I wish to thank Knut Christianson, my advisor, for his help and continued support and my committee, Michelle Koutnik and Daniel Shapero, whose help and guidance throughout graduate school made this thesis possible.

DEDICATION

to my parents, Barbara and Kurt, and my brothers, John and Peter.

Chapter 1

INTRODUCTION

Over the last three decades, observations have revealed sustained acceleration of Antarctic Ice-Sheet mass loss primarily through enhanced ice discharge through rapidly thinning outlet glaciers and ice streams. These changes observed at the periphery of the Antarctic Ice Sheet have been linked to enhanced ocean-driven melt beneath ice shelves, which reduces the capacity of floating glacier termini to buttress grounded ice. The need to understand these changes and assess their implications for sea-level rise has caused a growing shift in the methods and questions that drive glaciological research. They have also motivated unprecedented ground-based, air- and satellite-borne data collection efforts to observe these changes and monitor ice-sheet contributions to sea-level rise.

In this thesis, we use novel datasets to understand the nature of present and past controls on ice discharge. First, we focus on the periphery of the continent at changes happening presently on Thwaites Glacier in the Amundsen Sea and use swath radar data to understand sliding over highly resolved basal topography. We use these same swath radar datasets to connect observations of subglacial bedforms observed at the ice-sheet margins to bedforms we observe in the interior of the continent at Hercules Dome, where we hypothesize ice once flowed more rapidly than it does today. We then move to Conway Ridge adjacent to the Mercer and van der Veen ice streams that likely transport interior ice from Hercules Dome to the Ross Embayment. Near this ridge, we observe buried crevasses and layer shapes that suggest the region once flowed more quickly than it does today. We then turn back to the Amundsen Sea where we study surface crevasses and build a surface crevasse identification algorithm using satellite synthetic aperture radar imagery and neural networks. We apply this algorithm to map the evolution of surface crevasses in a region that has monotonically thinned and accelerated in the last twenty years and where the fracture mechanics of grounded ice has been hypothesized to make the region vulnerable to rapid disintegration.

Chapter 2

HETEROGENEOUS THINNING AND SUBGLACIAL LAKE ACTIVITY ON THWAITES GLACIER, ANTARCTICA

We begin by investigating one of the most peculiar signals observed in time series of surface altimetry: subglacial lake activity. Subglacial lakes, known to exist for decades, have been revealed to be active by radar and laser altimetry time series. Active subglacial lakes fill and drain on different timescales and sequester large volumes of subglacial melt water (> 1 km^3) that periodically drain through the subglacial hydrology system to the ocean. For much of the last twenty years, the significance of subglacial lakes and lake fill-drain cycles on the mechanics of glacier sliding and glacier discharge has remained unclear. The location of subglacial lakes and the timing of subglacial lake drainage are related to local stresses at the ice-sheet/bed interface. Here we use the expression of lake drainage on Thwaites Glacier to understand and characterize the basal environment near these features.

Chapter 2, Sections 2.1–2.7 and Appendix A, is a reprint of "Brief communication: Heterogenous thinning and subglacial lake activity on Thwaites Glacier, West Antarctica," authored by A. O. Hoffman, K. Christianson, D. Shapero, B. E. Smith, and I. Joughin, as it appears in *The Cryosphere*, 14, 4603–4609, 2020. The dissertation author was the primary investigator and author of this paper.

2.1 Introduction

Although subglacial lakes beneath the Antarctic Ice Sheet were first discovered more than 50 years ago (Robin et al., 1969; Oswald and Robin, 1973), they remain one of the most enigmatic components of the subglacial hydrology system. Initially identified in ice-penetrating radar data as flat, bright specular reflectors (Oswald and Robin, 1973; Carter et al., 2007), subglacial lakes were thought to be relatively steady-state features of the basal hydrology system with little impact on the dynamics of the overlying ice on multi-year timescales. The advent of high-precision repeat satellite observations in the 1990s, however, revealed an en-

tirely new class of active subglacial lakes that fill and drain on annual to decadal timescales and possibly affect the flow of the overlying ice (Gray et al., 2005; Wingham et al., 2006; Fricker et al., 2007; Smith et al., 2009). Under the central trunk of Thwaites Glacier, in particular, satellite radar altimetry revealed a large (~ 4 km^3 volume discharge), connected subglacial lake drainage event from 2012–2014 (Smith et al., 2017). Initial subglacial lake recharge estimates suggested lake drainages of this magnitude should occur every 20-80 years. To better constrain refill and discharge time, we extended the Thwaites Glacier velocity and altimetry record to include the most recent drainage events. We also expanded the spatial coverage to include Haynes Glacier and the western tributary of Thwaites Glacier (Fig. 2.1). Here, we describe the recent subglacial lake behavior in these regions and discuss the impact of these subglacial lake systems on slip velocity at the ice–bed interface.

2.2 Methods

We used in situ Global Navigation Satellite System (GNSS), satellite synthetic aperture radar (SAR) and satellite radar altimetry data to derive velocity and elevation-change time series.

2.2.1 Ice velocity and vertical displacement

We used the speed anomalies recorded by two long-term on-ice GNSS receivers, LTHW and UTHW, deployed on Thwaites Glacier from 2009 to present to augment Eulerian velocity products derived from Sentinel-1A and Sentinel-1B synthetic aperture radar (SAR) imagery of the Thwaites Glacier catchment collected between 2015–2019 (Fig. 2.1). Processing of GNSS data follows the workflow of Christianson et al. (2016a). We first created a position time series with sub-5 cm uncertainties in all dimensions by calculating geodetic positions every 30 s relative to two fixed rock sites located 200 km (Backer Island) and 300 km (Howard Nunatak) away from the LTHW site, using differential carrier phase positioning as implemented in the Track Software (Chen, 1998). We then constructed velocity time series from these geodetic solutions using 3-day Savitzky–Golay filtered moving averages (Press et al., 2007). Finally, we subtracted the SAR-derived Eulerian speed at each GNSS

position to solve for the Lagrangian velocity anomaly relative to the mean 2015–2019 velocity, omitting periods of lake activity (reference velocity field in Figure 2.1).

Following the methods of Joughin (2019) and Joughin et al. (2010), we constructed a speckle-tracked velocity time series of Thwaites Glacier from 2015 through the austral winter of 2019 using SAR data collected by the European Union's Copernicus Sentinel-1A and Sentinel-1B satellites and processed by the European Space Agency (ESA). We also computed the component of motion in the satellite line-of-sight (LOS) direction (Gray et al., 2005; Friedl et al., 2019). The bulk of this signal is due to relatively steady horizontal displacements, but it is also influenced by potentially more temporally variable vertical displacements. Thus, we computed the mean LOS component for the full-time series and subtracted it from each individual estimate. Since the horizontal and surface-parallel flow components are relatively steady, the residual line-of-sight estimate should largely be due to vertical motion, which we corrected for incidence angle effects to produce an approximate vertical displacement rate (V_z). Because we only subtracted the mean, a small component of the horizontal velocity may map into the vertical velocity due to the glacier's acceleration; however, this contribution is generally in the noise during periods with no lake activity and small relative to the vertical signal during times of active lake change (Fig. 2.2). To more tightly constrain the timing of the drainage events, we spatially interpolated the time series of Sentinel-1-derived V_z to fill gaps in coverage and integrated the result during a period of filling/draining (see solid vertical bars in Figure 2.2c) to produce estimates of net uplift and subsidence shown in Figure 2.2a.

2.2.2 Elevation and lake volume change

We also extended the previous time series of ESA CryoSat2 radar altimetry data (Smith et al., 2017) through austral winter 2019, as shown in Figures 2.2b and 2.3. Elevation models were derived by fitting surfaces of elevation change to CryoSat-2 swath-processed elevation retrievals and points-of-closest-approach relative to a reference elevation model from the first quarter of 2011 (Smith et al., 2017). The fitting procedure minimized an objective functional that considered data misfit, spatial gradients in the constructed reference

elevation model, elevation-change rate fields, temporal gradients in elevation-change rate and the magnitude of model bias parameters. In this scheme, three expected elevation statistics are used to choose weight parameters that regularize the least-squares fit. The elevation statistics, $E\left(\frac{\partial^2 z_0}{\partial x^2}\right)$, $E\left(\frac{\partial^3 z}{\partial x^2 \partial t}\right)$, and $E\left(\frac{\partial^2 z}{\partial t^2}\right)$, represent expected values for spatial and temporal derivatives of the reference elevation model, z_0 and the time-dependent height-change field, z. The values chosen for this study are $E\left(\frac{\partial^2 z_0}{\partial x^2}\right) = 6.7 \times 10^{-8}$, $E\left(\frac{\partial^3 z}{\partial x^2 \partial t}\right) = 6 \times 10^{-9}$, and $E\left(\frac{\partial^2 z}{\partial t^2}\right) = 1.0$ m^{2}yr^{-2} and tighten the spatial variations in the least-squares elevation time series, $E\left(\frac{\partial^2 z_0}{\partial x^2}\right)$ and $E\left(\frac{\partial^3 z}{\partial x^2 \partial t}\right)$, compared to the original Smith et al. (2017) implementation by factors of 5 and 10, respectively. These radar altimetry measurements complement SAR observations of integrated vertical displacement, which we use together to understand the character of new lake drainage activity.

2.3 Results: new observations of lake activity

We developed a complete chronology of progressive thinning and lake activity across Thwaites Glacier from the extended CryoSat-2 time series is shown in the video in Supplement Movie 1 (SV1) in Hoffman et al. (2020). These new observations reveal that the upper Thwaites Lakes, Thw$_{170}$ and Thw$_{142}$, drained in 2017, filling Thw$_{124}$ (Fig. 2.1 and 2.2). The SAR-derived elevation-change data show that the largest lake, Thw$_{124}$, filled by 1.9 km^3 during the 2017 drainage, roughly balancing the volume that drained from Thw$_{142}$ (0.6 km^3) and Thw$_{170}$ (1.4 km^3). The quarterly CryoSat-2 results show less clear evidence of water budget balance (Fig. 2.2 and A.2), which may be due to the degree of smoothing used in producing the time series. From CryoSat2 elevation-change data, between 2015 and before the 2017 drainage event, the areas inside the Thw$_{124}$, Thw$_{142}$ and Thw$_{170}$ lake outlines increase in elevation, which is strong evidence of filling (Fig. 2.3 and A.2).

The extended elevation time series (Fig. 2.3 and A.2) also reveals the fill-drain cycle of two new lake systems: one in the western shear margin of Haynes Glacier and another in the western tributary of Thwaites Glacier (Fig. 2.1). From these combined observations, the western Thwaites tributary lake (WT) drained by 1.1 km^3 in 2013 and the Haynes Glacier lake system (HG) drained by 0.2 km^3 in 2017 (Figures A.1 and A.2). Complete fill-drain cycles of the Haynes Glacier lakes and the western Thwaites Glacier lake are not observed

in the existing altimetry record, and the Haynes Glacier lakes do not discernibly refill after draining in 2017 (Fig. A.2). The western Thwaites tributary lake, however, fills significantly at a rate of 0.1 km^3 yr^{-1} after draining in 2014.

2.4 Discussion

Cascading lake drainages have been observed under many Antarctic ice–stream systems (e.g., Wingham et al., 2006; Fricker et al., 2007). The positions of all identified lakes beneath Thwaites Glacier, including the new lakes in the Haynes Glacier shear margin and western tributary of Thwaites Glacier, appear to be controlled primarily by the bed and associated surface geometry (Smith et al., 2017). There are large topographic ridges at the bed with corresponding expressions at the surface that are oriented orthogonal to flow and likely act as hydraulic baffles trapping water and sediments (Holschuh et al., 2020), causing hundred kilopascal-scale deviations in basal traction (Fig. A.5a; Joughin et al., 2014). The weak basal shear stress in these till-draped basins combines with large-scale catchment topography to promote variations in ice thickness and surface slope that form large hydropotential lows (Fig. A.4; Smith et al., 2017; Holschuh et al., 2020). In these hydropotential lows, the lakes remain disconnected from their neighbors as they fill until cascading drainages driven by the upstream lakes interrupt the background fill rate in the cycle. Densely sampled SAR vertical displacement rates from 2017 (V_z in Figure 2.2c) demonstrate this process, capturing the Thw_{170} drainage that initiated a combined drainage with Thw_{142} into Thw_{124} (Fig. 2.2).

The controls on lake filling are less clear. From the altimetry observations of the Thw_{170} fill cycle, the average fill rate is ~ 0.16 km^3 yr^{-1} (Fig. A.2). This agrees with the fill rate (~ 0.14 km^3 yr^{-1}) we calculate by routing modeled basal meltwater production (Joughin et al., 2009) down the glaciostatic hydropotential gradient (Shreve, 1972) into Thw_{170} but requires inflow of all melt water produced upstream into the Thw_{170} lake basin (Fig. A.4). The glaciostatic hydropotential also routes water around Thw_{170} into downstream lakes Thw_{142} and Thw_{124}, but the fill rates associated with these flow paths (~ 0.44 and ~ 0.27 km^3 yr^{-1}, respectively) are much larger than the fill rates derived from surface height change (Fig. A.4). These discrepant observations may reflect limitations of the static hydropotential assumption and the modeled catchment meltwater budget, but they also suggest current bed-

elevation models do not resolve small-scale (< 1 km) bed topography important for routing subglacial water into the upper most lake, Thw_{170}.

2.5 Lake impact on ice flow and coupled drainage morphology

The inland SAR and GNSS observations show a general pattern of acceleration at the LTHW and UTHW sites, consistent with an increase in driving stress due to inland propagation of thinning caused by ungrounding and loss of ice-shelf buttressing (Rignot et al., 2014; Joughin et al., 2014). Figure 2.3 shows the velocity anomaly at LTHW after subtracting the 2010 glacier velocity (340 m yr^{-1}). At LTHW, this secular trend is punctuated by two signals associated with the Thwaites Lakes drainage events, first in September 2012 and again in May 2017 (Fig. 2.3). During the 2012 drainage documented by Smith et al. (2017), surface velocities initially spike by 2% over a several-day period but then decline by 3% over the following 6 months. Loss of receiver power interrupted this record in March 2013. When the receiver began telemetering data again in 2015, the relative change in position suggests the speed anomaly in 2014 remained below what would be expected from the 2010–2012 trend. From January 2016 to May 2017, the LTHW receiver continued to accelerate at a rate of 4 m yr^{-2}. As Thw_{142} and Thw_{170} drained in the austral winter 2017, filling Thw_{124}, there was a nearly stepwise 1% increase in glacier speed at LTHW (Fig. 2.3). Speed remained elevated at the LTHW site after Thw_{124} stopped filling, coinciding with a 2° shift in ice-flow direction to the grid-north (clockwise), toward Thw_{124} (Fig. 2.3); however, this speed change is imperceptible in distributed velocity maps before and after Thw_{124} filled in 2017 (Fig. A.3). The UTHW site also exhibits subtle velocity fluctuations with a magnitude less than 1% of the mean velocity (105 m yr^{-1}) after correcting for the spatial ice-velocity gradient. These fluctuations are small relative to the background acceleration we observe at the UTHW site, 0.75 m yr^{-2}.

The transient velocity anomalies that depart from the trend observed at LTHW are likely related to subglacial lake dynamics. During lake filling in 2017, the areal extent of the Thw_{124} lake increases. This increase should reduce traction at the lake boundary, both at the margins (near the LTHW site) of the lake and inside the lake as unresolved topographic pinning points are submerged. In 2017, changes in basal traction occur almost immediately,

causing a step increase in velocity (Fig. 2.3). As the lakes drain, traction is restored as ice regrounds, reducing basal slip, which we observe in the months following the 2012 lake drainage near Thw_{124}.

The positive GNSS acceleration observed in September 2012 (Fig. 2.3) suggests that Thw_{124} began to drain in 2012 before the quarterly resolved subsidence associated with the lake drainage becomes distinguishable in the CryoSat-2 surface elevation time series (Fig. 2.3). The cause of the acceleration we observe at Thw_{124} before the bulk drainage cannot be unambiguously attributed to a discrete set of processes with these data, but the finite duration of the velocity increase ($\sim$ 10 days) suggests that a distributed drainage system may have been established at the downstream edge of the lake preceding bulk drainage. Glaciostatic hydraulic water routing indicates that Thw_{124} would likely drain at the grid-south edge of the lake near the LTHW GNSS receiver (Fig. A.4). Enhanced lubrication outside the low-drag Thw_{124} basin as the lake begins to drain likely increases local slip and drives the subtle change in ice-flow direction that we observe in the austral winter of 2012 before the peak drainage in 2013, when flow direction shifts back to the mean flow direction between 2010–2012. Non-steady effective pressure likely also affects the basal shear stress as the drainage system initially forms, then empties and closes. Similar to lake drainages under the Siple Coast ice streams (Siegfried et al., 2014, 2016), changes in basal slip speed due to lake activity are small ($\sim 1 - 2$ %) relative to the average sliding speed.

Regardless of the exact drainage mechanism, the locations of the lakes are governed by ice-flow response to the underlying bed topography, which promotes hydropotential basins that form as ice flows over ridges. Once a connected drainage begins, differences in water pressure in the conduits between lakes promote efficient drainage down the hydraulic gradient. During drainage, each lake is likely in local equilibrium with the ends of the conduits that directly connect to it; however, the large hydropotential differences between lakes ($\sim$ 1 MPa) cannot equilibrate along the entire length of the drainage path, which implies that the pressure difference over the length of the conduit is likely more important in determining whether water flows into or out of the lakes than the small variations in the hydraulic potential in the lakes as they fill and drain. Conversely, drainage of upstream lakes may disrupt the steady-state drainage morphology by temporarily increasing the hydraulic conductivity

of the conduits, bringing additional water into the lower lakes and allowing drainage from adjacent lakes that share the same downstream conduit. The processes governing changes in subglacial hydraulic connectivity are poorly understood but likely depend on the local dynamic hydropotential and the evolution of conduit morphology, which we do not try to infer from our observations of the fill-drain cycle. We only note that these processes likely contribute to the variability in lake fill-drain levels observed elsewhere over multiple fill-drain cycles (Fig. A.2; Siegfried et al., 2014, 2016), which cannot be explained by the evolving glaciostatic hydropotential alone.

2.6 Implications for basin-wide change

The velocity changes in Figure 2.3 that we attribute to lake drainage events represent the dominant, albeit small (0.3%), inland sub-annual velocity variability. The lakes sequester water and thus likely play some not well-understood role in maintaining distributed low effective pressures that control long-term flow rates, but the fill-drain cycles have little transient effect on the flow behavior of the overlying ice. On decadal timescales important for understanding ice-sheet behavior and contribution to sea level, the lakes do not appear to control inland ice-flow variation. Static inversions for bed resistance before and after the 2017 lake drainage event (see Section A.4 for details) are not sensitive to the subtle surface velocity changes we measure with GNSS (Fig. A.5), and the lakes identified by Smith et al. (2017) have no discernible effect on ice velocity at the UTHW site. These new observations suggest that the observed speedup at the grounding zone of the main trunk of Thwaites Glacier following the 2013 drainage (Smith et al., 2017) was associated with warming ocean conditions following anomalous Amundsen Sea wide ocean cooling from 2012/13 (Christianson et al., 2016a). These warm ocean conditions likely enhanced sub-ice-shelf melt and led to increased ungrounding and acceleration. Our observations and model experiment (Sect. A.4; Shapero et al., 2020)) invalidate proposed geoengineering solutions that seek to drain large volumes of water from beneath Amundsen Sea Embayment glaciers to increase basal resistance (Moore et al., 2018). These results further demonstrate that capturing the details of lake fill-drain cycles, and at least some elements of the associated basal hydrology system, may not be that important for modeling Thwaites Glacier's contribution to sea level on

decadal to centennial timescales.

2.7 Conclusions

We document the temporal change in velocity and elevation far from the grounding zone in response to the steepening of Thwaites Glacier and three distinct systems of active lakes: one on the main Thwaites Glacier trunk, another in the western shear margin of Haynes Glacier and a third in the westernmost tributary of Thwaites Glacier. At the LTHW GNSS site, over 100 km from the grounding line, ice velocity has accelerated at a nearly constant rate over the last decade. This background acceleration was interrupted in 2012 by the connected drainage of lakes Thw_{124}, Thw_{142} and Thw_{170} and, in 2017, by the partial filling of Thw_{124} via drainage of Thw_{142} and Thw_{170}. Our observations suggest that the transport of $\sim$2 km^3 of water beneath Thwaites Glacier, which represents approximately half the annual basal meltwater production for the entire Thwaites catchment (Joughin et al., 2009), has only a small and transient effect on glacier speed relative to ongoing thinning driven by ocean melt.

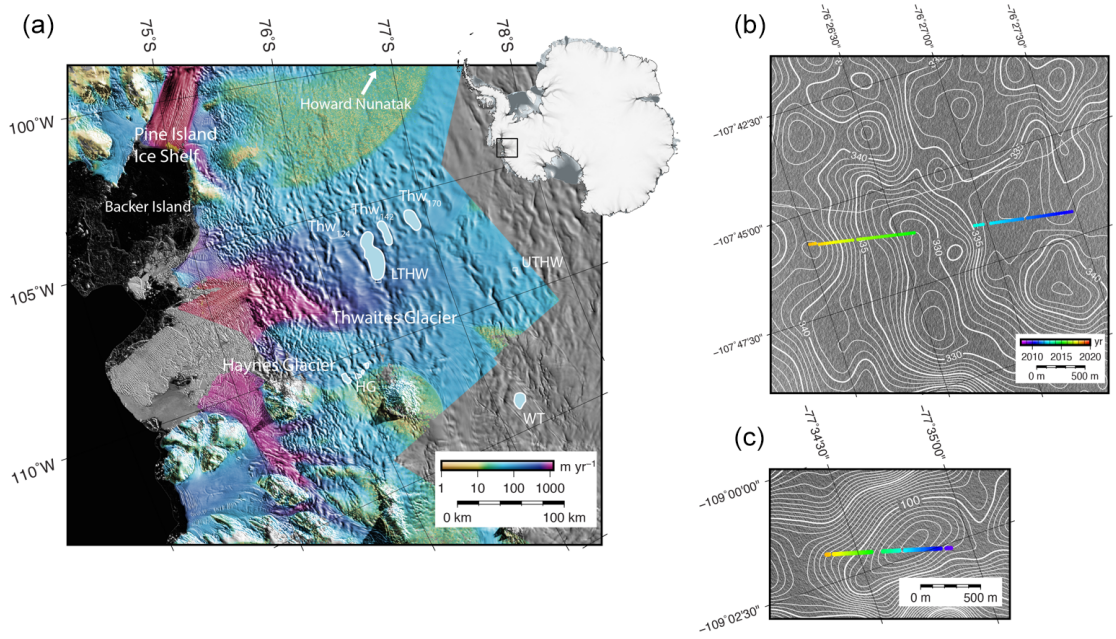

Figure 2.1: Location map of Thwaites Glacier and subglacial Thwaites lakes. (a) Average ice speed between 2015–2019 omitting period when lakes were active (color) plotted over Moderate Resolution Imaging Spectroradiometer (MODIS) image mosaic (Haran et al., 2018). Thwaites Glacier, Thwaites Lake 124 (Thw_{124}), Thwaites Lake 142 (Thw_{142}), Thwaites Lake 170 ($_{170}$), Haynes Glacier (HG) lake, western Thwaites (WT) lake and GNSS sites (LTHW and UTHW) are labeled. Thwaites lakes are named by their approximate distance from the grounding line. (b) LTHW and (c) UTHW GNSS position plotted over time (color) with contoured mean velocity between 2015–2019.

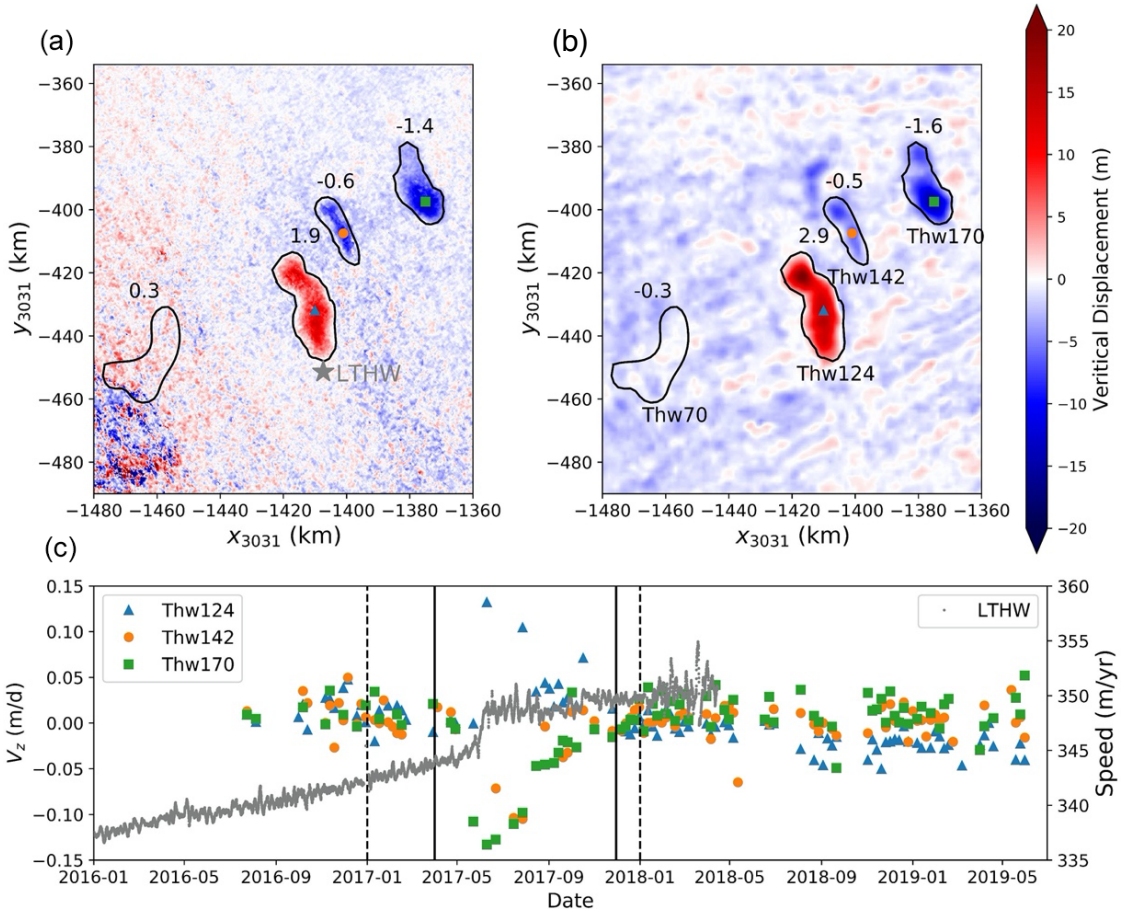

Figure 2.2: Surface elevation-change time series over the Thwaites Glacier lakes showing the 2017 drainage cascade from (a) vertical displacement computed from integrated vertical displacement rates (V_z) from Sentinel-1 SAR data and (b) swath-processed radar altimetry in a polar stereographic projection (EPSG:3031). Water volume (km^3) associated with observed vertical displacement is labeled for each lake. (c) Time series of uplift rates (V_z) from SAR LOS results (colored dots, left abscissa); locations marked in (a) and (b) and horizontal speed from GNSS observations (right abscissa). Solid lines represent period over which SAR vertical displacements (V_z) were integrated to produce the vertical displacements shown in (a). Dotted lines represent the quarters of gridded CryoSat-2 data differenced to create (b).

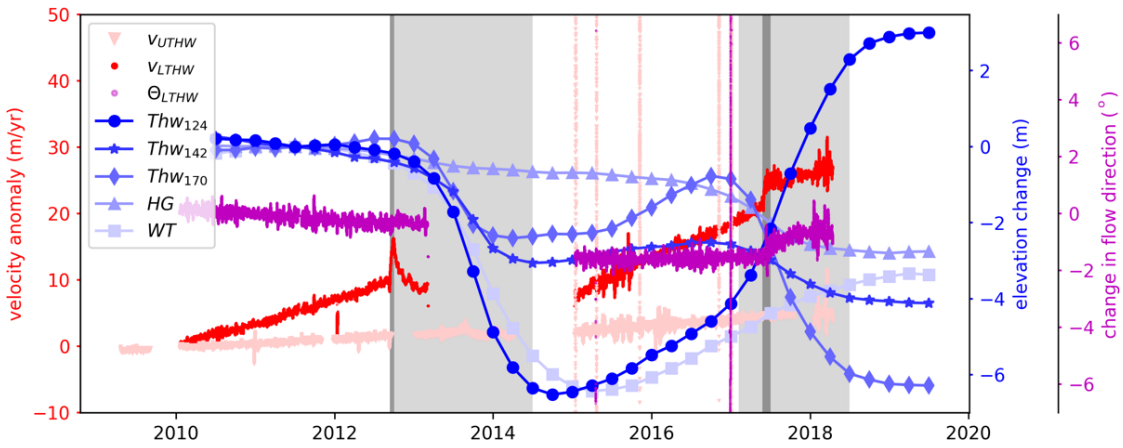

Figure 2.3: Time series of GNSS velocity anomalies at UTHW and LTHW corrected for advection using the Eulerian velocity products and CryoSat-2 lake elevation change averaged over each lake area. See Figure 2.1 for site locations and abbreviations. Also plotted are LTHW GNSS clockwise direction change relative to 2010 flow direction (purple). The dark grey shaded periods indicate intervals when the LTHW GNSS accelerated significantly (99% confidence), while the light grey periods indicate when the $\text{Thw}_{124,142,170}$ lakes are active. When the largest lake fills in 2017, the LTHW GNSS closest to the lake accelerates and flows towards the lake.

Chapter 3

THE IMPACT OF BASAL ROUGHNESS ON INLAND THWAITES GLACIER SLIDING

In Chapter 2, we showed that basal resistance on Thwaites Glacier is relatively insensitive to lake dynamics and lake fill and drain cycles. From observations of surface velocity throughout a lake fill cycle, we observe that basal slip speed is relatively insensitive to the subglacial lake high stand, suggesting that the environments that harbor subglacial lakes on Thwaites occupy regions of relatively low basal resistance. These observations also suggest that the networks of connection between the lakes do little to change distributed basal resistance across the Thwaites catchment. Taken together, this is evidence that subglacial lake fill-drain cycles have a limited effect on changes in distributed glacier discharge. This raises the question: what does control basal resistance beneath Thwaites Glacier?

In this Chapter, we use unprecedented high-resolution images of the glacier bed generated with swath radar technology (Paden et al., 2010; Jezek et al., 2011; Holschuh et al., 2020) to understand the relationship between the morphology of the subglacial landscape and the basal shear stress inferred using full-Stokes models of ice flow. Model experiments conducted in this region as part of this study are some of the most highly resolved slip experiments to date (100 m element sizes) for one of the very few regions where bed topography is resolved below the resolution limits of typical catchment-scale model experiments.

Chapter 3, Sections 3.1–3.5 and Appendix B, is a reprint of "The Impact of Basal Roughness on Inland Thwaites Glacier Sliding," authored by A. O. Hoffman, K. Christianson, N. Holschuh, E. Case, J. Kingslake, and R. Arthern, as it appears in *Geophysical Research Letters*, 49, e2021GL096564, 2022. The dissertation author was the primary investigator and author of this paper.

3.1 Introduction

A primary question driving glaciological research today is: how much and how fast will global sea-level rise due to Antarctic Ice Sheet mass loss (Scambos et al., 2017)? The Amundsen Sea Embayment in West Antarctica has long been considered geometrically prone to collapse (Clark and Lingle, 1977; Hughes, 1981). Thwaites Glacier (Fig. 3.1), the largest glacier in the Amundsen Sea Embayment and the glacier projected to contribute the most to sea-level rise in West Antarctica beyond the next century, is likely in the early stages of this marine ice-sheet instability (Joughin et al., 2014; Rignot et al., 2014; Shepherd et al., 2012). The pacing of Thwaites Glacier retreat remains uncertain in part due to poorly constrained solutions for the parameters that control glacier sliding. Assumptions underlying the mechanics that define the boundary condition at the ice-bed interface affect the glacier's modeled response to ocean forcing, increasing glaciological sources of uncertainty in predictions of the West Antarctic Ice Sheet's contribution to sea level over decadal timescales (Brondex et al., 2019).

To simulate catchment-scale glacier discharge and retreat, time-evolving prognostic ice-flow simulations must define the boundary condition at the ice-bed interface, usually as part of a diagnostic optimization experiment. It is customary to assume the velocity normal to the bed is zero – ice cannot penetrate the bed. The form of the friction law, also described as the sliding law, or sliding relation in the literature, is then typically defined to condition the tangent component of the sliding velocity, relating the bed-parallel basal velocity, $\boldsymbol{u}_{\boldsymbol{b}}^{\parallel}$, to the shear stress at the interface, $\boldsymbol{T}_{\boldsymbol{b}}^{\parallel} = f\left(\boldsymbol{u}_{\boldsymbol{b}}^{\parallel}\right)$.

Assuming some sliding relation, $f\left(\boldsymbol{u}_{\boldsymbol{b}}^{\parallel}\right)$, ice-sheet models can be used with inverse methods (e.g., Joughin et al., 2004; Morlighem, 2011; Seroussi et al., 2014; Riel et al., 2021) to solve for the glacier sliding velocity and the parameters that define the sliding relation. An example sliding parameter is the friction coefficient, β, in the linear law proposed by MacAyeal (1989), $\boldsymbol{T}_{\boldsymbol{b}}^{\parallel} = \beta \boldsymbol{u}_{\boldsymbol{b}}^{\parallel}$, built on the work of Weertman (1964). The domain geometry defined by the ice thickness and elevation is often assumed to be known perfectly in the ice-sheet model inversion. The result is a velocity and parameter solution consistent with surface observations that relies on assumptions made about the bed geometry, defined, crucially, by ice-penetrating radar data and the resolution of the model domain.

Theoretical descriptions of the basal boundary condition often separate the contributions from the material friction at the ice-bed interface (skin drag) and the enhanced stresses within the ice required to overcome geometric obstacles to flow (form drag; Kyrke-Smith et al., 2018). Models that lack sufficient resolution to capture small-scale features of the ice-sheet bed have no way to disentangle these two controls on ice flow. The result is a basal friction proxy that misrepresents sources of stress at the ice-bed interface.

Because the sliding law is poorly understood, it is customary to use the shear stress associated with an inferred friction proxy field (for instance, β) to initialize simulations with alternative representations of sliding physics. Some sliding relations that parameterize skin drag are fundamentally based on assumptions for unresolved bed roughness and depend strongly on flow speed (Weertman, 1957). Other sliding relations include linkages to independent fields such as effective pressure (i.e., Fleurian et al., 2018), subglacial temperature (i.e., McCarthy et al., 2017), and till porosity (i.e., Minchew and Meyer, 2020) that evolve independently in time and produce different glacier responses in prognostic simulations driven by the same climate forcing. Even for models wherein the total drag is made to be rate-dependent – governed by form drag at slow speeds and effective-pressure-dependent skin drag at faster speeds (i.e., Zoet and Iverson, 2020) – skin drag and form drag may remain mispartitioned in inferred resistance proxies due to the prescribed model geometry. The inability to accurately partition basal drag into form drag and time-variable skin drag is a major challenge for prognostic ice-flow modeling that remains understudied.

Higher resolution models should theoretically better constrain form drag and thus improve estimates for skin drag (Kyrke-Smith et al., 2018). In this study, we use a series of smoothed swath-mapped topographies for two subdomains of Thwaites Glacier (Holschuh et al., 2020) to determine the influence of the bed roughness wavenumber, which describes both the spatial frequency of the roughness and roughness orientation on the inferred friction proxy. We first describe the model physics and the equations solved in the inversion. Then, we introduce the data and describe the experimental framework used to explore the convolution of form drag and skin drag before interpreting the resulting friction proxies in the context of analytic form-drag theory.

3.2 Methods

3.2.1 Ice Flow Model

Ice flow can be modeled using the Stokes equations by introducing a non-Newtonian constitutive law (Glen's flow law) that describes the non-linear deformation of ice under an applied stress (Cuffey and Paterson, 2010). In our study, we use the full-Stokes solver implemented in Elmer/Ice (Gagliardini et al., 2013) to interrogate stresses at the ice-bedrock interface (see Table B.1 for all parameters used in the inversion). The sliding relation defines the boundary condition at the bed interface and relates the basal shear stress, $\boldsymbol{\tau_b}$, along flow to the glacier's sliding speed. In this study, we assume a sliding relation of the form

$$\boldsymbol{\tau_b^{\parallel}} = \beta \left| \boldsymbol{u_b^{\parallel}} \right|^{\frac{1}{m}} \tag{3.1}$$

where $\boldsymbol{u_b}$ is the sliding velocity at the bed, β is the friction coefficient, and m is the glacier sliding exponent (Weertman, 1964). Solutions for β and m are not unique and cannot be distinguished from snapshot inversions of a single bed-friction proxy. In many studies, m is assumed to be uniformly 3, though spatially variable values for the glacier slip coefficient and the sliding exponent have been inferred using time-dependent data assimilation from time series of ice surface elevation and velocity (Goldberg et al., 2015). Here, we set $m = 1$ but focus analysis on the inferred patterns of the shear stress, $\boldsymbol{\tau_b}$, which, in the limit of plug flow, theoretically does not depend on the coupled assumptions made for β and m.

Robin Inverse Method

We use the Robin inverse method, described by Arthern and Gudmundsson (2010) and implemented in Elmer/Ice, to infer the value of the friction coefficient, β, by solving the constrained optimization problem defined by the objective functional,

$$\boldsymbol{J}(\boldsymbol{\kappa}) = \frac{1}{2}\int_{\Gamma_s} \hat{\boldsymbol{n}} \cdot \left(\boldsymbol{\sigma^N} - \boldsymbol{\sigma^D}\right) \cdot \left(\boldsymbol{u^N} - \boldsymbol{u^D}\right) d\boldsymbol{A} + \lambda \frac{1}{2}\int_{\Gamma_b} \left(\frac{\partial \boldsymbol{\kappa}}{\partial \boldsymbol{x}}\right)^2 + \left(\frac{\partial \boldsymbol{\kappa}}{\partial \boldsymbol{y}}\right)^2 d\boldsymbol{A} \tag{3.2}$$

where $\hat{\boldsymbol{n}}$ is the unit outward normal vector, $\boldsymbol{\sigma^N}$ and $\boldsymbol{\sigma^D}$ are the full Cauchy stress tensors for the velocity solutions, $\boldsymbol{u^N}$ and $\boldsymbol{u^D}$, which are constrained by Neumann and Dirichlet

conditions at the ice-sheet surface, respectively, and κ is the friction proxy varied in each inversion across the ice-sheet base. An exponential map relating the friction coefficient and the control parameters, $\beta(\kappa) = 10^{\kappa}$, is used to ensure the inferred friction coefficient is strictly positive.

3.2.2 Observational Data

The model-data misfit and resulting inference of the spatially distributed friction proxy is limited by the assumptions made about the ice viscosity, as well as the accuracy of surface velocity, surface elevation, and ice-thickness observations. The ice viscosity was calculated from the Arrhenius relation described by Cuffey and Paterson (2010) using the temperature profile from the WAIS Divide borehole assuming a thawed bed (Orsi et al., 2012). The surface velocities used to constrain the inversions are averaged from the first quarter of 2016 and were computed using synthetic aperture radar (SAR) data from the European Space Agency's (ESA) Copernicus Sentinel-1A and Sentinel-1B satellites following the methods of (Joughin et al., 2018, 2021). The surface elevation used in the model was derived from the spatiotemporal least squares fitting procedure described by Smith et al. (2017) applied to Cryosat-2 radar altimetry, optical satellite stereo-imagery, and IceBridge airborne laser altimetry from the first quarter of 2016 when subglacial lakes beneath Thwaites Glacier were inactive (Hoffman et al., 2020).

To test the sensitivity of model-derived friction proxies on the resolution of the basal topography, we produce 15 topographic datasets of varying resolutions from each original swath topography (Holschuh et al., 2020) for a total of 30 different topographies, which we use in 15 simulations of the upper Thwaites grid and 15 simulations of the lower Thwaites grid (Fig. 3.1). For each swath grid, 13 topographies were smoothed isotropically using smoothing kernels that filtered wavenumbers (inverse of wavelength) from 1/1,300 m^{-1} to 1/200 m^{-1}. Roughness is often anisotropic in areas of elongated bed features, which are present in both swath-mapped subdomains of Thwaites Glacier. To test the influence of roughness orientation on the inferred friction proxy, two additional topographies were smoothed preferentially along and across flow. The anisotropically smoothed topographies were filtered

relative to the flow direction, as defined by the reference surface velocities, using a weighted Gaussian kernel. The ratio of the Gaussian kernel smoothing in the along-flow and across-flow directions was varied between 1:1 and 4:1 to preserve the total spectral power relative to grids smoothed in the transverse flow direction. All 30 smoothed topographies are included in the Appendix B along with the surface elevation model and surface velocities used to constrain the inversion (Fig. B.1–B.3).

3.3 Results

The inferred distributed basal drag (the bed-parallel shear) is shown in Figure 3.2 for selected isotropically filtered grids. These results represent the best fit to the surface velocity data filtered by the surface-to-bed transfer function we solve in our inversion. We also plot the distributed normal pressure and the domain average normal pressure. The Tikhonov regularization curves used to select these shear stress fields are included in Appendix B (Fig. B.6; Shapero et al., 2016). For both the lower and upper Thwaites Glacier model domains, the misfit between the observed and modeled horizontal surface velocity was reduced as the resolution of the bed topography increased.

To better isolate the relationship between bed roughness (see Section B.1) and the inferred friction coefficient, we interpolate the inferred friction proxy to a regularly spaced grid and correlate the friction coefficient with the total spectral roughness energy for the suite of isotropically smoothed grids. The windowed power spectral roughness for the native 25 m^2 resolution grids is shown in Figure 3.3. The regression slope of the inferred friction proxy is shown in Figure 3.4. From the regression slopes, we can identify regions where smoothing the basal topography has a strong effect on the magnitude of the inferred friction coefficient (relationship indicated by sign of slope).

3.4 Discussion

Our discussion is organized into four parts. We first discuss the normal pressure and quantify the impact of topographic smoothing on form drag. We then characterize the general patterns in the inferred friction fields, which remain largely unchanged across degrees of topographic smoothing. Finally, we discuss the effect of anisotropic smoothing on the in-

ferred resistance field and compare the numerically derived slip lengths with predictions from analytic theory along flow lines.

3.4.1 Normal Pressure, a Measure of Form Drag

Using a full-Stokes model that resolves all components of the stress tensor, we can determine the influence of form drag directly by integrating the normal pressure. Following Schoof (2002), stress at the ice-bed interface can be broken down into the sum of form drag exerted by the undulating topography and tangential stress associated with skin drag

$$-\int_{\Gamma_b} \boldsymbol{\sigma}\hat{\boldsymbol{n}}d\boldsymbol{A} = -\int_{\Gamma_b} \hat{\boldsymbol{n}}\cdot\boldsymbol{\sigma}\hat{\boldsymbol{n}}d\boldsymbol{A} - \int_{\Gamma_b} \hat{\boldsymbol{t}}\cdot\boldsymbol{\sigma}\hat{\boldsymbol{n}}d\boldsymbol{A} \tag{3.3}$$

where $\boldsymbol{\tau}$ is the stress tensor, $\hat{\boldsymbol{n}}$ is the unit vector normal to the bed, and $\hat{\boldsymbol{t}}$ is the unit vector tangent to the bed in the direction of flow. In Weertman's original formulation, the tangent stress is assumed to be zero, and this assumption is invoked in many subsequent framings of basal sliding (i.e., Schoof, 2002). The influence of form drag can therefore be measured by comparing the solutions for normal pressure at the glacier bed. Our simulations show that the normal pressure decreases as the bed topographies are progressively smoothed, changing on average by 10 kPa as the maximum bed roughness wavenumber (minimum wavelength) is filtered from 1/100 m^{-1} to 1/1,000 m^{-1} (Fig. 3.2). We next turn to the patterns of skin drag that remain unchanged across degrees of smoothing to understand the resistance from features that are not resolved in the radar data.

3.4.2 Patterns of Basal Friction Inferred for Swath Mapped Topographies

The bed topography of each swath-mapped grid can be clustered into two subdomains based on the roughness characteristics of the basal topography (Fig. 3.4) One subdomain includes ridge-like features with roughness oriented equally in all directions with roughness wavelengths that span the width of the grid. The other includes lineated features with roughness oriented primarily orthogonal to flow with roughness anisotropy that is well captured by the swath topographies.

The spatial coverage of these clustered domains aligns with the unchanging patterns

of skin drag we solve in our inversions. The lineated regions of each domain provide less resistance than the rest of the glacier bed and isolated patches of high resistivity control cumulative basal drag (Fig. B.4 and B.5). In the lower Thwaites grid, we infer a two-order reduction in basal resistance in the lineated basin where we observe ongoing thinning in satellite altimetry time series referenced to the upstream ridge (Hoffman et al., 2020). The combined observations of significant inland thinning, low inferred basal drag that is independent of basal velocity, and independent measurements of low acoustic impedance (Clyne et al., 2020; Muto et al., 2019) consistent with water-saturated till suggest that the strength of the bed is relatively independent of the rate of deformation, or that the bed deforms more plastically in these regions (Clyne et al., 2020; Muto et al., 2019).

3.4.3 The Effects of Smoothing on Skin Drag

From the friction coefficients inferred for the anisotropically filtered grids, we find that along-flow smoothing increases the inferred skin drag at the ice-sheet bed. Smoothing the bed along flow reduces form-drag induced stresses in the ice, which are subsequently mapped into the friction proxy (skin drag). To quantify this, we compare the difference in inferred basal friction coefficient for along-versus across-flow-smoothed beds. The difference between the average friction coefficient for the transverse-flow filtered roughness and the along-flow filtered roughness is 203 Pa·(m/a)$^{-1}$ and 217 Pa·(m/a)$^{-1}$ for the lower Thwaites and upper Thwaites grids, respectively (transverse-flow filtered – along-flow filtered).

A similar relationship might be expected to manifest in the isotropic smoothing experiment: an increase in inferred basal friction coefficient in grids with reduced spectral roughness power. The relative magnitude of this relationship should be controlled by changes in unresolved form drag across the smoothed topographies, which would present as significant and negative regression slopes after correlating total spectral power of each grid with each pixel of inferred friction coefficients. Instead, we found weak and variable relationships between roughness and inferred basal drag across the domains (Fig. 3.4). The regression slopes are steepest in the lineated regions of each basin, as identified from k-means clustering of the unfiltered bed topography (Fig. 3.3) In these areas, the friction coefficient increases

by a factor of two as the roughness of the bed topography decreases across the 13 isotropically filtered simulations. But over the ridges where the overall inferred basal drag was high, the relationship between roughness reduction and inferred drag was weak, with very small changes in inferred values across the suite of topographies tested. The insensitivity to smoothing could imply that form drag is dominated by features smaller than < 100 m wavelength (the highest resolution grid tested). To evaluate this hypothesis, we examine analytic theory for form drag and its agreement with the numerically inferred friction field.

3.4.4 Agreement Between Numerical Results and Analytic Theory of Form Drag

The Weertman sliding relation we use to map distributed resistance assumes that a film of water between the ice and bedrock facilitates free slip at the microscopic scale, $\boldsymbol{\tau_{bmicro}} = 0$, which can be used to derive relationships between area-averaged shear stress and unresolved roughness at larger scales, $\boldsymbol{\tau_{bmicro}} = f\left(\boldsymbol{u_b}\right)$. Based on this area-averaged assumption, analytic descriptions of ice flow over a spatially variable ice-sheet bed can be used to understand the influence of roughness at different spatial scales on basal resistance to ice motion.

We apply analytic theory first described by Fowler (1986) and expanded by Schoof (2002) and Hogan et al. (2020) that formulates form drag as a function of topographic roughness. Assuming a linear friction law of the form $\boldsymbol{\tau_b} = \beta \boldsymbol{u_b}$, consistent with the law used to infer the basal resistance field in our model experiments and assuming that bed roughness is dominated by small wavelength features, the friction coefficient (β) can be expressed as the sum of contributions (β_n) from features of angular wavenumber ($k_n = 2\pi f_n$) as:

$$\beta_n = 4\frac{\eta}{H}\left(\frac{k}{k_n}\right)^3 F\left(\frac{k_n}{k}\right)\frac{\left|\hat{h_n}\right|^2}{H^2} \tag{3.4}$$

where k_n is the integer wavenumber corresponding to the frequency $f_n = n/a$, $\hat{h_n}$ is the Fourier component of the bed topography at spatial frequency f_n, η is the ice viscosity, $k^* = 1/H$ is the inverse characteristic thickness, H, taken to be the mean thickness over the window length, a, and $F\left(k_n/k^*\right)$ is a transfer function that relates the surface expression of basal drag to the friction coefficient (Schoof, 2002).

Following Hogan et al. (2020), we use periodogram coefficients as an approximation to

Fourier coefficients as the glacier's bed includes substantial spatial variability in frequency content over the length of a flowline. Using frequency bins of width $1/a$ centered at $f_n = n/a$ from $n = 1$ to $n = 256$, we use an inverse-square law to fit periodogram coefficients to the power spectrum periodogram of the swath topography along flowlines. Like other studies (Hogan et al., 2020; Jordan et al., 2017; MacGregor et al., 2013), we find that the power spectrum (periodogram, P_n) can be fit well by an inverse-square law as a function of frequency ($P_n = Af_n$ correlation coefficient $r = 0.78$ for the upper Thwaites grid and $r = 0.73$ for the lower Thwaites grid). Assuming this relationship holds for all frequencies, total drag would be unbounded unless the bed becomes smooth at some scale smaller than a given wavelength (λ_N, here assumed to be the limit of the radar resolution, 25 m), and the basal friction coefficient can be approximated by a truncated sum that simplifies to $\beta = 8\eta\pi^3 A\lambda_N^2$.

The slip length is defined as the effective ice viscosity divided by the basal friction coefficient ($L = \eta/\beta$). For slip lengths much greater than the ice thickness, the basal drag is too small compared to the ice viscosity to induce substantial shear in the ice column, and the ice slides over its base in plug flow. For slip lengths much smaller than the ice thickness, drag is large enough compared to the viscosity to induce shearing throughout the ice column. We calculated slip lengths from the analytic linear sliding coefficients and use the full-Stokes solutions to calculate the modeled slip lengths from the friction coefficient and the effective ice viscosity determined from modeled strain rates at the ice-sheet bed (Fig. 3.5). The effective viscosity

$$\eta = 2A^{-\frac{1}{n}}\dot{\epsilon}_e^{\frac{-(n-1)}{n}} \tag{3.5}$$

was computed using modeled effective strain rates, $\dot{\epsilon}_e = \sqrt{\dot{\boldsymbol{\epsilon}}_{\boldsymbol{ij}}\dot{\boldsymbol{\epsilon}}_{\boldsymbol{ij}}/2}$, and modeled enhancement factor $A = A_0 e^{-Q/RT}$ (see Table B.1 for parameters used in the inversion). The agreement between analytically and numerically derived slip lengths suggests:

- Bed roughness resolved by the swath radar is well characterized by a power-law fit, indicating roughness resolved by swath radar may provide information about roughness below the swath radar measurement resolution.

- Analytical predictions of basal resistance associated with form drag are consistent with the flow dynamics at Thwaites Glacier.

Our isotropic smoothing experiment shows that in the lineated regions of Thwaites, form drag remains at scales captured by the swath radar, and the inferred basal drag falls with smoothing. The roughest regions of the bed (the ridges) provide the most resistance to flow. In these regions (identified in red; Fig. 3.4), the patterns and magnitude of the inferred friction coefficient remain unchanged across degrees of smoothing, and the ratio of the bed tangent stress to normal pressure is high. This could suggest that fine-scale roughness that is unresolved in the highest resolution swath radar topographies controls the total basal drag budget. The static drag budget associated with the ridge surrounding the largest subglacial Thwaites lake (hashed region in Figure 3.1, Thw_{124}) provides much of the resistance we observe in static inversions for basal shear stress. This may also explain why local ice dynamics are relatively insensitive to changes in effective pressure inferred from satellite altimetry time series of the lake fill-drain cycle (Hoffman et al., 2020).

3.5 Conclusion

Our analysis shows that form drag and skin drag remain convolved in ice-sheet model inversions for basal shear stress at resolutions finer than the limits prescribed in most ice-sheet models and new radar swath-mapped bed topography (the highest resolution mapping currently possible). High resolution radar mapping cannot yield a topography that captures all of the form drag, and thus it seems likely that form and skin drag will always be blurred in numerical models. However, going forward, self-similarity in the basal roughness and the inferred basal resistance field may allow for a parameterization of form drag from swath radar.

The results of our study also have implications for controlled analog experiments (i.e., ring shears; Zoet and Iverson, 2020) that aim to partition total drag into form drag (for slow basal slip rates) and skin friction (at faster slip rates). The application of these models is always going to be limited by the reality that sliding relations in ice-sheet models must also capture the effects of sub-resolved bed morphology. Consistency between the numerically

and analytically calculated slip lengths suggests that high-frequency ($<\sim$ 100 m wavelength) roughness controls bed resistance across inland portions of Thwaites Glacier; however, the feature size of the flow-controlling obstacles remains unknown. Our results suggest that the controlling behavior and empirical form of the sliding relation associated with cm-scale clasts at low-slip speeds should be evaluated with larger-scale features that are still unresolved in modern ice-sheet topography. Idealized prognostic model experiments are also needed to better understand the sensitivity of glacier retreat and mass change due to the convolution of form drag and skin drag from the effects of unresolvable roughness.

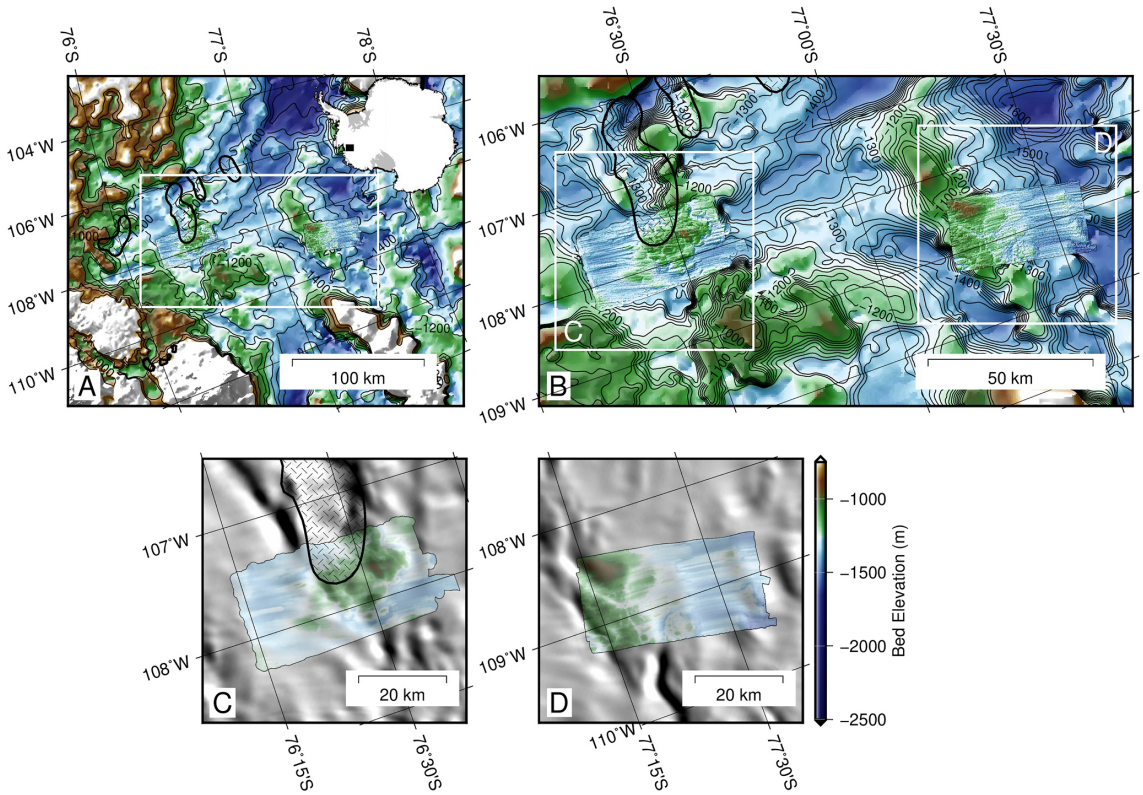

Figure 3.1: Overview map of Thwaites Glacier showing locations of the two model domains. (a) Thwaites Glacier regional subglacial topography from BedMachine Antarctica (Morlighem et al., 2020) with swath radar topography (Holschuh et al., 2020) superimposed for both model domains. Inset shows map location in Antarctica. (b) Local subglacial topography (white box in A) in the vicinity of the model subdomains. Radar swath-mapped topographies are plotted on MODIS image mosaic of Antarctica (Haran et al., 2018) for the (c) lower Thwaites grid and (d) upper Thwaites grid, which highlights influence of bed topography on ice surface geometry. Positions of active subglacial lakes, most recently observed to be active in 2017 (Hoffman et al., 2020; Smith et al., 2017), are marked by hashed polygons. Projection is polar stereographic (EPSG: 3031) and contours denote bed elevation relative to WGS84 ellipsoid.

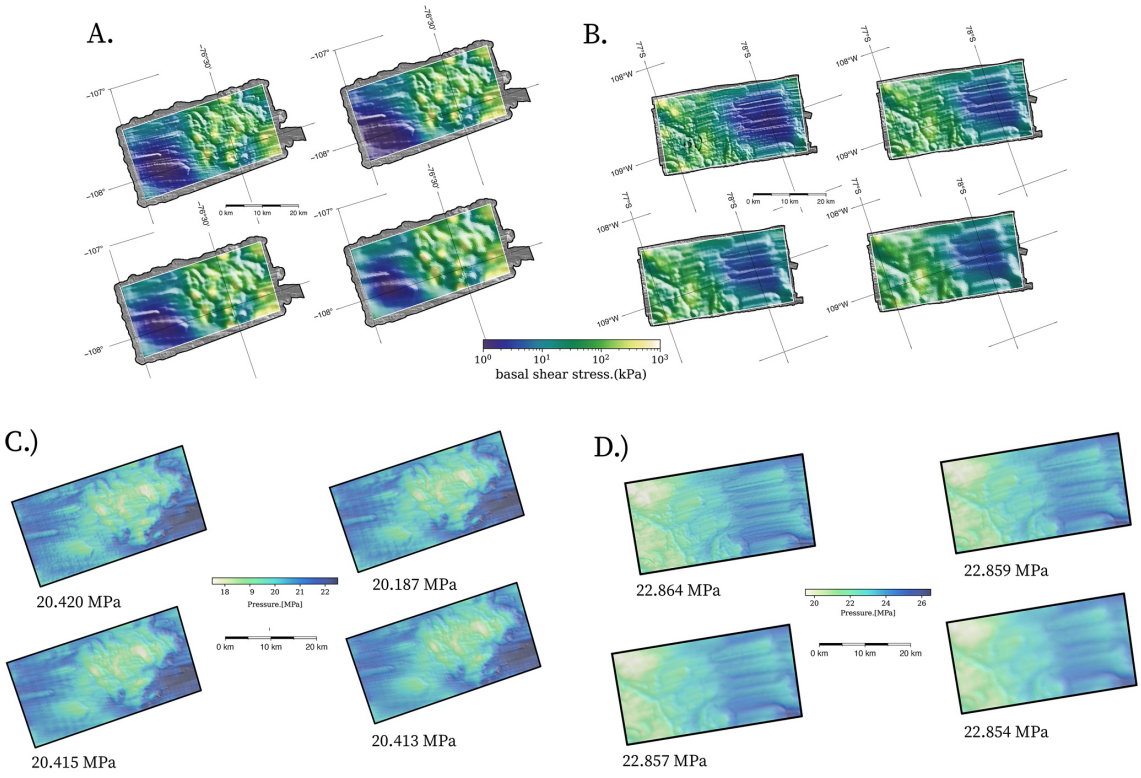

Figure 3.2: Inferred basal shear stress for the 1/200 m^{-1}, 1/400 m^{-1}, 1/600 m^{-1}, and 1/1,000 m^{-1} wavenumber isotropically filtered grids, overlaying the filtered topography (hillshade) used in each experiment for the (a) lower Thwaites grid and (b) upper Thwaites grid. Also, shown is the normal pressure at the ice-bottom boundary for the (c) lower Thwaites and (d) upper Thwaites grids with the mean normal pressure solution printed below each grid.

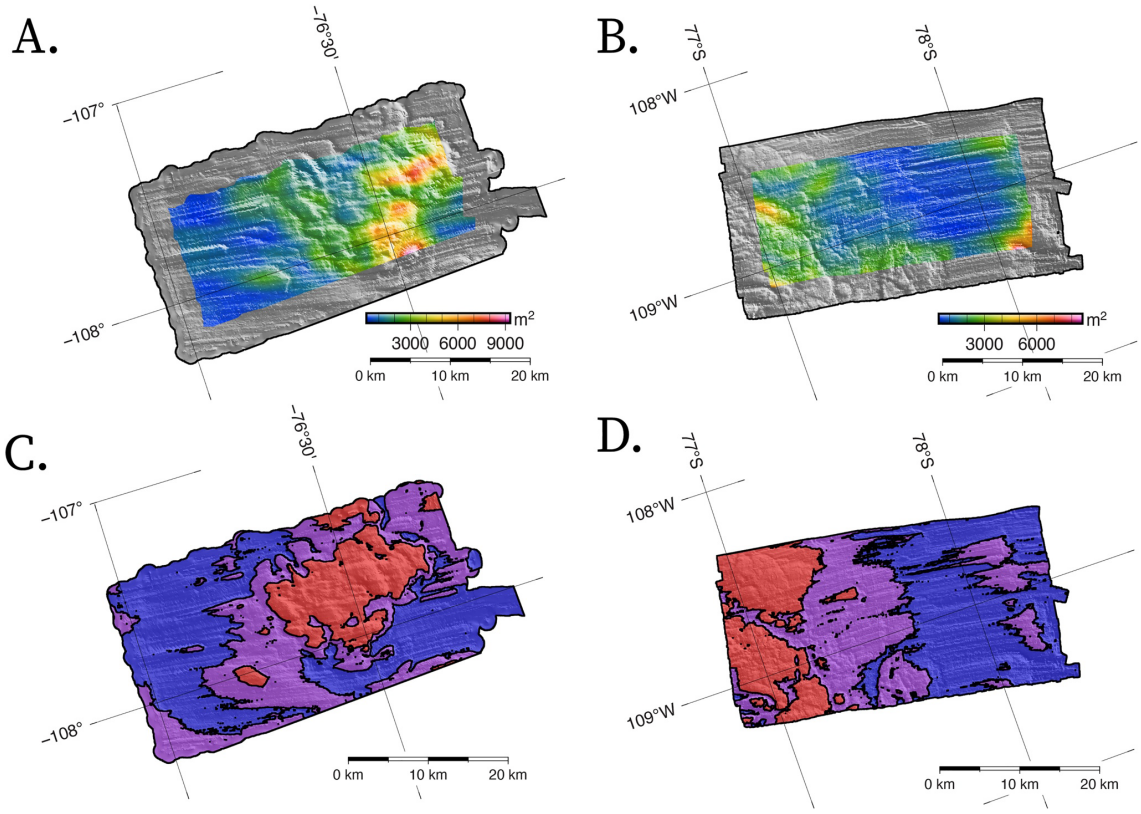

Figure 3.3: Total two-dimensional spectral variance of 6.0 km windowed bed topography for the (a) lower and (b) upper Thwaites grids with the (c), (d) k-means clustered regions, which we use to identify lineations (blue), ridges (red), and intermediary classes of bedforms and subglacial canyons (purple).

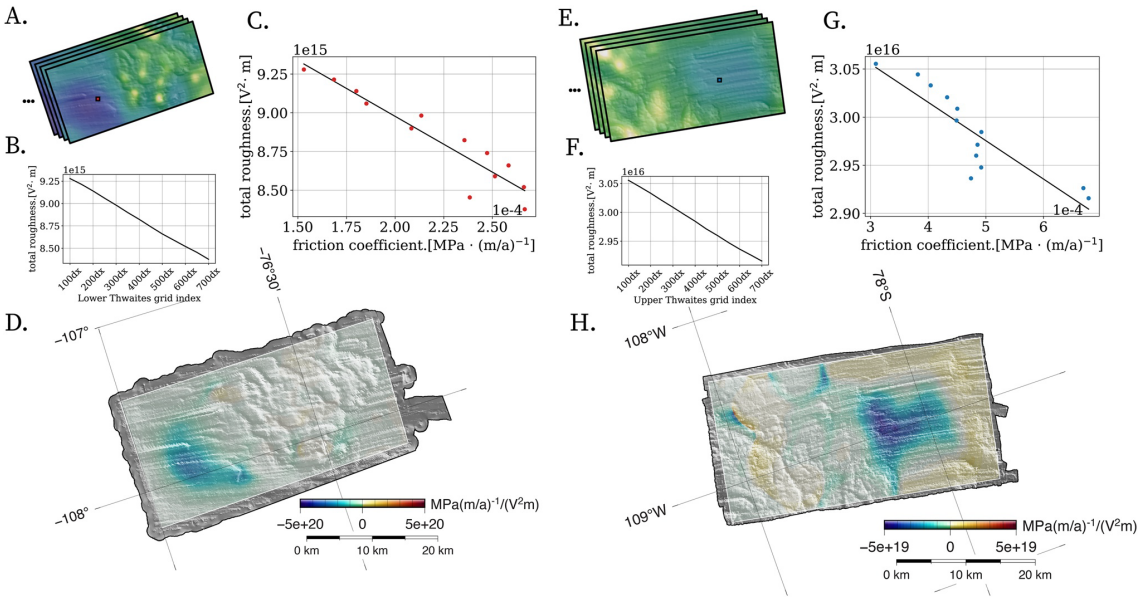

Figure 3.4: Grids of (a, e) the friction coefficient ordered by filtered roughness were correlated with the (b, f) total spectral roughness of each grid. The grid index label (x-axis of (b, f) indicates the approximate scale of quarter wavelength features preserved in the smoothed topography. Sample correlations (c, g) are shown for two indices in regions of the lineations. Regression slope of the inferred friction coefficient with the total power spectral energy of the bed topography used in each simulation for all thirteen isotropically filtered grids for (d) lower Thwaites and (h) upper Thwaites grid.

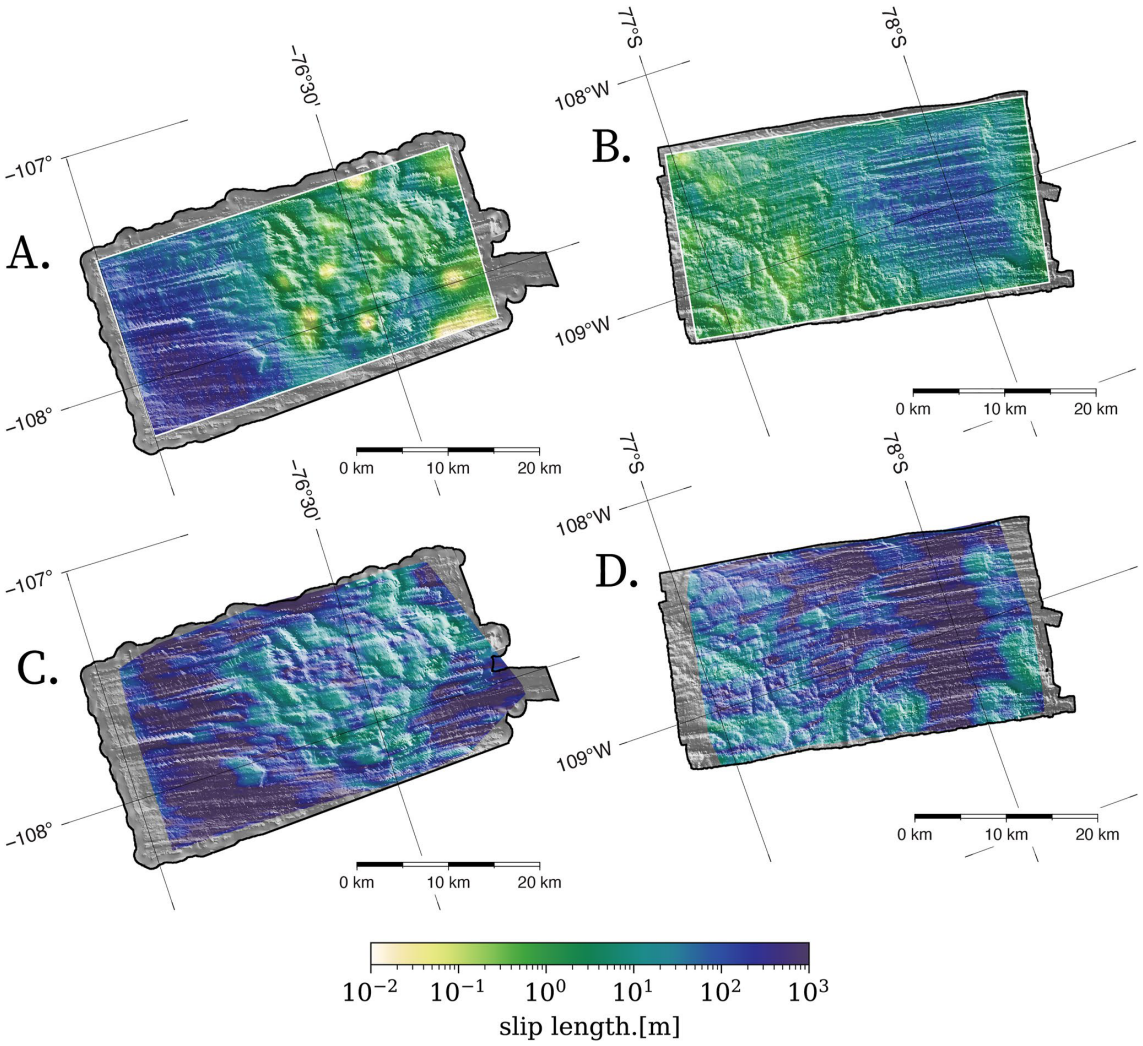

Figure 3.5: Numeric slip lengths calculated for the (a) lower and (b) upper Thwaites grids shown with (c), (d) analytic slip lengths calculated with 6 km moving windows (see Section B.1 for details).

Chapter 4

SCARS OF TECTONISM PROMOTE ICE-SHEET NUCLEATION FROM HERCULES DOME INTO WEST ANTARCTICA

In this Chapter, we move geographically from the margins of the West Antarctic Ice Sheet, where ice is flowing quickly (1-5 km yr^{-1}) and changing most rapidly today, and turn to interpretations of three-dimensional swath radar data (Paden et al., 2010; Jezek et al., 2011; Holschuh et al., 2020) that were collected in the slow-flowing regions of the Antarctic interior at Hercules Dome. The data from Hercules Dome were obtained with a ground-based radar platform that is the evolved successor to a similar ground-based array deployed on Thwaites Glacier in the 2008-2009 field season and airborne radar antennas installed on a fixed-wing aircraft (Twin Otter) in the 2009-2010 austral summer (Holschuh et al., 2020). These systems all use linear-chirped FMCW radar antenna arrays with a center frequency near 300 MHz and bandwidth between 100 MHz and 300 MHz, and represent a new evolution of radar technology, which has been used in glaciology for ∼100 years.

Radar use in glaciological applications has a history that spans nearly a century. The first radio transmissions in Antarctica were made from the Little America II base in the early 1930s. Although these high-frequency radio transmissions were for communication and were successfully received on consumer radios in the United States, members of the Byrd Antarctic Expedition noted that the signals could also be received in the subsurface, in the buried Little America I base. This initial observation that radio waves could effectively penetrate snow and ice was further bolstered by confounding readings from radar altimeters on US Army Air Force aircraft over Antarctica, Greenland, and Arctic Canada in the 1940s and 1950s, which indicated that very-high-frequency radio waves may reflect from dielectic interfaces within and possibly at the base of the large masses of ice. These anecdotal suggestions that radar could penetrate and image the interior and basal boundary of glaciers and ice sheets were confirmed by Waite and Schmidt (1962), who used a radio altimeter to measure the

thickness of an Arctic glacier in 1959.

Following these initial discoveries, use of radar to image ice thickness, ice-sheet internal architecture, and topography beneath the ice proliferated widely over the next 40 years (Schroeder et al., 2020). Between the 1970s and the 1990s, airborne radar arrays were commonly used to map ice-sheet internal layer structure, ice thickness, and bed topography (Schroeder et al., 2020). These airborne antenna arrays used synthetic aperture focusing following the assumption that targets are stationary. Under this assumption, the phase differences in the arrival of the back-scattered energy in sequential acquisitions are typically used to position subsurface targets in the along-track direction, with along-track resolution enhanced through azimuthal processing (Gogineni et al., 1998; Paden et al., 2010). However, if there are multiple antenna phase centers in the cross-track direction and the cross-track beam resolution if fine enough, phase differences in the arrival of energy in the cross-track receiver elements can be tracked in sequential acquisitions, allowing mapping of direction of arrival for energy in both the along- and across-track directions (Paden et al., 2010; Holschuh et al., 2020). By the early 2000s, radar hardware and processing technology had advanced enough to allow simultaneous along- and across-track mapping, i.e., three-dimensional swath mapping within the imaging aperture of the antenna array. This technology was first employed near the summit of the Greenland Ice Sheet in 2005 and resulted in three-dimensional maps of the ice-sheet bed topography, akin to terrestrial laser scanning maps of surface topography (Paden et al., 2010). Maps of the bed topography of glaciers and ice sheets were previously limited in cross-track resolution to the survey line spacing, but now true three-dimensional mapping of the ice-sheet internal structure and bed topography is possible. In Chapter 3, I used swath maps of the Thwaites Glacier bed as input into a full-Stokes model run at unprecedented resolution, which determined that short-wavelength bed topography is an important control on Thwaites Glacier basal sliding (Hoffman et al., 2022). Here, I apply this new swath-mapping radar technology to investigate the bed topography of the Antarctic interior at Hercules Dome.

Our swath survey at Hercules Dome reveals large glacier valleys of similar scale to Yosemite Valley. Within these valleys, there are bedforms similar to those seen under the fast-flowing ice of Thwaites Glacier. This suggests ice flowed quickly sometime in the past

in this presently slow-flowing area. We show that reduced models of glacier flow suggest that the glacier's bed in this region could act to facilitate relatively rapid ice-sheet response to forcing at the terminus, and that these glacier valleys and large troughs that they flow into likely facilitate glacier advance following ice-sheet deglaciation. Using gravity data that were collected as part of the PolarGAP survey (Winter et al., 2018; Jordan et al., 2018), we connect the glacier valleys we image at Hercules Dome to deeper geologic structures that still appear to control the position of downstream fast-flowing ice streams today (Anandakrishnan et al., 1998; Bell et al., 1998).

Chapter 4, Sections 4.1–4.5, is a reprint of "Scars of tectonism promote ice-sheet nucleation from Hercules Dome into West Antarctica," authored by A. Hoffman, N. Holschuh, M. Mueller, J. Paden, A. Muto, G. Ariho, C. Brigham, J. Christian, L. Davidge, E. Heitmann, B. Hills, A. Horlings. S. Morey, G. O'Connor, T.J. Fudge, E. Steig, and K. Christianson, as it appears in review at *Nature Geoscience* in 2023. The dissertation author was the primary investigator and author of this paper.

4.1 Introduction

The West Antarctic ice sheet (WAIS) has long been considered susceptible to collapse. The capacity for the WAIS to rapidly change volume is linked to the marine ice-sheet instability – a nonlinear relationship between ice flux and ice thickness that drives models of marine-terminating glaciers to either advance or retreat from grounding zones positioned on topography that deepens inland. The WAIS is vulnerable to this instability in the marine basin confined by the TransAntarctic Mountains, coastal mountains of Marie Byrd Land, the Whitmore Block, and the subglacial highlands of the Ellsworth and Thiel Mountains where ice flows into Ross and Filchner-Ronne ice streams.

Despite the well-understood capacity for the WAIS to retreat into the interior, very little is known about the confining subglacial highlands that likely serve as ice-sheet refugia during deglaciation and as nucleation centers during readvance (Bentley et al., 1960; Ross et al., 2014). Three-dimensional model simulations of the West Antarctic ice sheet, paleo sea-level change observations, and reconstructions of ice volume during recent interglacials suggest that the ice sheet's instability response may permit the ice sheet to deglaciate faster than it

can reglaciate (Pollard and DeConto, 2009; Rohling et al., 2009). This asymmetry has been linked to large interior surface mass balance fluxes required to promote WAIS regrounding across ocean-separated West Antarctic highland regions that include the Ellsworth Mountains and the coastal mountains of Marie Byrd Land (Ross et al., 2014; Holschuh et al., 2014). Ice transport from the larger East Antarctic margin was instrumental for the early formation of the WAIS in the Miocene. The ice-covered extensions of the Horlick and Thiel Mountains near Hercules Dome have also long been recognized as key sites for ice-sheet regrowth (Bentley et al., 1960; Winter et al., 2018), likely facilitating ice transport to the WAIS when it was smaller than it is today.

Following previous studies that used subglacial morphology to understand ice-marginal behavior when the Antarctic ice sheet was smaller (Bo et al., 2009; Young et al., 2011; Rose et al., 2013; Holschuh et al., 2014), we use new geophysical data collected near Hercules Dome to better constrain the past behavior in the upstream reaches of the Ross and Filchner-Ronne ice streams (Fig. 4.1). Using high-frequency impulse and multi-element ice-penetrating radar, we produce the first three-dimensional (swath) bed topographies of the slow-flowing Antarctic interior (Fig. 4.1b, 4.2). The features revealed by the radar swaths combined with regional airborne gravity data (Winter et al., 2018; Jordan et al., 2018) provide new insight into tectonic controls on glaciation at the junction of East and West Antarctica and the initiation of past ice ages when ice near Hercules Dome flowed more rapidly than it does today.

4.2 Survey overview and high-resolution subglacial topography mapping

Hercules Dome, located in East Antarctica at ~86°S, 105°W (Fig. 4.1a, b), is a compelling candidate location for a deep ice core (Jacobel et al., 2005; Steig et al., 2015) that would provide information on the configuration of the WAIS during the last interglacial (Steig et al., 2015) when global mean temperatures were as warm as they are today (i.e., Shackleton et al., 2003; Turney et al., 2020). Ice-flow modeling studies show that the Hercules Dome region remained glaciated during the last interglacial period (Pollard and DeConto, 2009), and climate model results show that significant lowering of the adjacent WAIS surface would cause atmospheric circulation changes that may be reflected in the isotopic composi-

tion of precipitation at Hercules Dome due to its proximity to the WAIS (Steig et al., 2015). Ice-penetrating radar data collected across a transect of Hercules Dome during the US portion of the International Trans-Antarctic Scientific Expedition (ITASE) traverses revealed continuous layers to depths just hundreds of meters above the bed (Welch and Jacobel, 2005; Jacobel et al., 2005). This supported conjectures that flow through parts of the dome has been stable throughout much of the last glacial period (Jacobel et al., 2005). Satellite observations of the dome's complex multi-axis structure (Howat et al., 2019) support this possibility and suggest that the position of the dome is anchored by local subglacial topography (Fig. 4.1b, 4.2a).

To better characterize the subglacial landscape, we deployed multi-element swath radar (Paden et al., 2010; Jezek et al., 2011; Holschuh et al., 2020) and conventional high-frequency impulse ice-penetrating radar (Welch and Jacobel, 2003; Christianson et al., 2016b) at Hercules Dome. Both radar systems were used to map englacial layering and along-track subglacial topography at ∼5 m posting; where available, swath radar mapped cross-track topography at ∼25 m posting in swaths ∼2 km wide (see Fig. 4.1 for an overview of the impulse radar profiles and swath-mapped topography). These data cover previously unmeasured regions of the ice-sheet interior, and can be connected to existing ice-penetrating radar data (Welch and Jacobel, 2005; Jacobel et al., 2005; Winter et al., 2018) to extend our knowledge of the ice sheet stratigraphy into the bottleneck between East and West Antarctica. We use polar stereographic (EPSG:3031) referenced directions (i.e. grid east, grid west) to describe relative positioning within the survey. First, we characterize the large-scale features in the radar data before discussing smaller-scale landforms and evidence of subglacial water mapped in radar swaths. We then contextualize these new observations with existing aerogravity data collected by the PolarGAP survey (Jordan et al., 2018; Winter et al., 2018; Paxman et al., 2019), past studies of the regional tectonic history, and theoretical models of ice-sheet response time.

4.2.1 Subglacial valleys and bedforms

Both radars imaged deep U-shaped valleys at Hercules Dome, similar to those typically found in glaciated alpine environments (Fig. 4.2–4.4). The deepest and most pronounced valleys appear to be part of one contiguous feature stretching from the grid southwest region of the survey to the grid east. The dramatic relief (1000–1500 m over a few kilometers) continues to affect modern ice flow, promoting deflection greater than five degrees in the englacial layer slopes in profiles crossing the valley (Fig. 4.4). Grid north of this feature, we image additional kilometer-scale features consistent with alpine glaciation, including hanging valleys and arêtes (Fig. 4.2–4.4).

Within the large U-shaped valley system, Fourier analysis of swath radar topographies revealed younger sub-kilometer scale landforms that appear to be associated with streaming flow and two candidate subglacial lakes that suggest the bed in the valleys is thawed (Fig. 4.3–4.4). The landforms include strongly tapered, elongated crags and tails, and weakly tapered longitudinally symmetric bedforms consistent with drumlins, glacial lineations, and glacial sills (Fig. 4.2–4.3, 4.7–4.9). Many of these features are thought to align with the flow direction during formation and can therefore be used to understand past ice-flow direction (Spagnolo et al., 2014). Across all radar swaths, windowed Fourier analysis of landform orientation suggests ice flowed rapidly along the subglacial valley axes (Fig. 4.3, 4.7–4.9).

4.2.2 Gravity field anomalies

The ice-flow direction imprinted in the swath-imaged valleys implies ice flow into larger basins that underlie the upper reaches of West Antarctic ice streams. Using radar and gravity data collected by the PolarGAP survey (Winter et al., 2018; Paxman et al., 2019), we evaluate the hypothesis that the basins host low-density sediment columns by calculating gravity anomalies associated with density contrasts consistent with the modern ice thickness, basin geometry, and geology using methods described by Plouff (1976) and Muto et al. (2013, 2016). Local geology is unknown in the region of Hercules Dome, and thus substrate density and basement depth were treated as free parameters informed by outcrop observations from the Ellsworth and Thiel Mountains (Flowerdew et al., 2007) and density data available for

other Antarctic sediment basins (Trey et al., 1999; Karner et al., 2005). Free-surface gravity anomalies range between -90 and 90 mGal with well-defined lows coincident with topographic troughs imaged with high-frequency impulse radar (Fig. 4.1b, 4.4, 4.10). Forward gravity calculations indicate that these topographic basins are likely underlain by thick (1000-2000 m) low-density (2400 kg/m3) sediment columns (Fig. 4.5, 4.11).

The pattern of satellite and aerogravity data suggests that Hercules Dome is associated with a positive gravity anomaly, with ice likely anchored by remnants of an igneous province or potentially old cratonic bedrock (Fig. 4.5). The upstream extensions of Mercer, Whillans, Support Force, and Foundation ice streams continue into basins (topographic troughs and negative gravity anomalies) that isolate Hercules Dome from East and West Antarctica (Fig. 4.1,4.5, 4.10–4.11). The valleys imaged with swath radar appear to connect with these larger basins, and, together with the density contrasts and the morphologic context of the Neoproterozoic rifted margin, suggest that alpine glaciers fed into paleo ice streams that flowed from the East Antarctic margin to the Ross and Filchner-Ronne seas.

4.3 Discussion

4.3.1 New Constraints on the Geologic Evolution of Antarctica

Our new swath radar observations reveal an alpine subglacial landscape at the interior origins of Whillans, Mercer, Foundation, and Support Force ice streams in the central TransAntarctic Mountains in unprecedented detail. Most of the subglacial features we image are inconsistent with the current slow outflow from Hercules Dome and resemble deglaciated alpine landscapes, such as the Yosemite Valley and marine-proximal glaciated valleys found in the Antarctic Peninsula, Alaska, and Norway (Fig. 4.4). Ice-core evidence (Korotkikh et al., 2011; Steig et al., 2015; Turney et al., 2020), ocean sediment cores (Turney et al., 2020), and far-field sea-level data (Lisiecki and Raymo, 2005; Raymo and Mitrovica, 2012) support a smaller West Antarctic ice sheet during the last interglacial (130–115 kyr before present) and marine isotope stage 11 (420–360 kyr before present). Still, the durations of these interglacials were likely too short to promote the incision of >1 km deep valleys at Hercules Dome. This suggests that they were likely carved in the Pliocene or earlier when the ice

sheet was much thinner and when flow did not override locally high topography, driving localized erosion and valley formation (Harbor and Warburton, 1993).

Within these valleys, we identify bedforms associated with streaming flow that are thought to require faster basal sliding speeds for formation than the ice surface speeds we observe at Hercules Dome today (Spagnolo et al., 2014; Ely et al., 2016; Barchyn et al., 2016). Most of our observations of glacial bedforms come from deglaciated environments and include features formed or modified during glacier retreat. Features associated with deglaciation (i.e., kettles, kames, eskers, and moraines) represent the "death mask" of a retreating ice sheet and have been used to understand past changes in ice-sheet extent. Similarly, observed bed features consistent with fast flow in glaciated environments that are not currently flowing quickly allow us to identify past regions of fast flow and candidate nucleation centers that promoted past ice-sheet advance. The landforms and large-scale topography all indicate that ice flowed rapidly along the trough axis at Hercules Dome. This flow orientation is at times orthogonal to the current outflow from the local ice divide. The inferred past-flow direction suggests that ice from Hercules Dome fed into larger basins beneath paleo ice streams associated with negative gravity anomalies. Even today, interior ice flow is influenced by these basins as the surface is depressed and surface velocities increase in these regions (Fig. 4.10).

Evidence of past streaming flow in the interior of the continent and thick sediment deposits within the downstream basins are also consistent with the region's tectonic history (Salvini et al., 1997; Rossetti et al., 2006; Jordan et al., 2020a, 2022a). The host rock that anchors Hercules Dome and the nearby southern TransAntarctic Mountains is a Neoproterozoic-Cambrian metasedimentary basin (Storey et al., 1996; Paxman et al., 2019). The outcrop ages of the nearby Thiel Mountains (Pankhurst et al., 1988), sedimentological, structural and geochemical studies (Storey et al., 1996), and gravity and magnetic data (Paxman et al., 2019; Jordan et al., 2018) confirm that these rocks were deformed during the Cambro–Ordovician Ross Orogeny. The major basins are only imaged in cross-section by the PolarGAP aerogeophysical survey (Fig. 4.5; 4.10), but they resemble graben or wrench basins. The valleys at Hercules Dome feed into these basins, which geographically align with the West Antarctic ice streams (Bell et al., 1998). Ice flow is clearly topographically steered

along these basins as it flows from the East Antarctic continental margin to West Antarctica (Winter et al., 2018).

The potential fault-bounded nature of the basins is difficult to connect to a single extension event, and any fault can reactivate in response to regional tectonic activity. The most recent and extreme extension event occurred in the Late Cretaceous when the West Antarctic Rift System and the Marie Byrd Land block separated from the East Antarctic Ross Orogen as an active subducting margin and magmatic arc (Jordan et al., 2020a). Over a span of just 20 Myr, the movement of these blocks contributed to over 600 km of extension in the West Antarctic interior, triggering melt and emplacement of the upper crust that promoted thermal subsidence to form the West Antarctic ice sheet's quintessential over-deepened basin (Jordan et al., 2020a; Salvini et al., 1997, and references therein). The extension of the West Antarctic Rift System has previously been linked to rifting across the Siple Coast (Dalziel and Lawver, 2001) and has been identified as a controlling influence on the position of marginal ice streams further from the interior (Anandakrishnan et al., 1998; Bell et al., 1998). These larger tectonic basins appear to control the position of the upper extension of the Mercer and Whillans ice streams and the paleo-alpine glacier networks we image at Hercules Dome.

4.3.2 Implications of the Geology for Ice-Sheet Evolution

Marine outlet glaciers advance or retreat in response to flux imbalances between discharge across glacier grounding zones and the integrated accumulation upstream (Schoof, 2007; Joughin and Alley, 2011). Spreading ice shelves confined to fjords or pinning points can stabilize a growing ice sheet by buttressing grounded ice, which, in concert with sufficiently positive surface mass balance, can lead to additional ice flow from the glacier interior resulting in further glacier advance. The pace of this change depends on how quickly interior surface mass balance changes can be transported to the grounding zone. This "glaciological filter", associated with properties of conveying ice streams, plays a vital role in determining the pace of early ice-sheet advance.

Using observations of swath-mapped lineations and topographic ridges in currently fast-

flowing glaciated environments under Thwaites Glacier (Holschuh et al., 2020; Hoffman et al., 2022), we infer a contrast in basal resistance fields associated with lineated and highland features of the Hercules Dome topography. We then estimate basal resistance for these two substrate types and incorporate them into an idealized outlet-glacier model (Robel et al., 2018; Christian et al., 2020) to characterize how the fast-flowing valley glacier networks in our observations (Fig. 4.2, 4.4) would have affected the interior ice-sheet response to perturbations in surface mass balance forcing (see Section 4.5.4; Fig. 4.6).

Sampling a range of different sliding parameters and equilibrium estimates of interior surface mass balance that produce the same glacier length, we calculate characteristic ice thickness and glacier response time using the idealized model (see Section 4.5.4). We find that interior ice transport over a basal environment consistent with landforms we image at Hercules Dome reduces the equilibrium thickness and the characteristic timescale for glacier advance compared to the response time inferred for the modern configuration of the ice sheet (Fig. 4.6).

4.4 Conclusions

Our observations highlight the important and often underappreciated influence of West Antarctica's geologic history on the ice sheet's capacity to change volume. Radar-imaged valleys at Hercules Dome likely hosted paleo ice streams that conveyed ice to West Antarctica, potentially playing an important role in both seeding the early growth of the West Antarctic ice sheet and facilitating subsequent readvances. The positions of sedimentary basins, likely controlled by the tectonic history of the continent, appear to precondition the past flow patterns we see imprinted on the floors of glacially-incised valleys. Connections between past rifting and ice-stream flow have been observed near the present-day ice-sheet margins (Bell et al., 1998; Bingham et al., 2012) but had not been made in the interior, where streaming flow has implications for ice-sheet cycles. We conclude that past rifting that preceded or was activated during the extension event responsible for the over-deepened WAIS basin also facilitated early ice-sheet advance through interior basin-guided ice streams from mountain highlands adjacent to Hercules Dome.

4.5 Methods

4.5.1 Impulse Radar Topography

An impulse ice-penetrating radar system operating at a center frequency of 3 MHz was used to map bed topography and ice-sheet internal layering at nadir. See Christianson et al. (2016b) for comprehensive system details. This radar system is an evolutionary advance from earlier impulse radars (Welch and Jacobel, 2003; King et al., 2009) with increased bandwidth, faster digitization, higher sampling frequency, and increased dynamic range (Christianson et al., 2016b). Impulse radar data processing steps include bandpass filtering (8th-order Butterworth bandpass from 0.5 to 5 MHz), time correction for antenna separation, geolocation from dual-frequency GNSS data, interpolation to a precise trace spacing of 5 m, and along-track time-wavenumber migration (assumed radar wave speed in the ice of 169 m/μs). An adaptive horizontal filter that subtracts the average low-frequency component in a moving 100-trace boxcar window with a vertical exponential taper was also applied at shallow depths to improve imaging of shallow stratigraphy. The basal reflector was digitized using a semi-automated routine that identified the Ricker wavelet corresponding to the ice-bed interface (Gades et al., 2000; Christianson et al., 2016b; Lilien et al., 2020).

4.5.2 Swath Radar Topography

Conventional ice-penetrating radars have limited or no ability to localize energy in the cross-track direction, so cross-track resolution has historically been dictated by the choice of cross-track line spacing when designing surveys. Swath processing of a multi-element antenna array allows energy localization in the along- and across-track directions. In the along-track direction, phase differences from sequential acquisitions are used to position subsurface returns, which results in a conventional nadir-focused image. However, by combining target position from phase differences in sequential along-track acquisitions with phase differences between receiver elements in the cross-track antenna array, energy can be positioned in both directions simultaneously, allowing three-dimensional mapping of the subsurface (Paden et al., 2010; Holschuh et al., 2020). We applied the MUltiple SIgnal Classification (MUSIC) algorithm implemented in the Center for Remote Sensing of Ice Sheets toolbox (Paden et al.,

2010) to estimate the direction of arrival signals. Following Al-Ibadi et al. (2017), we digitized the reflector in the cross-track direction to geolocate off-nadir reflection information from multichannel frequency-modulated continuous wave radar data. This algorithm produced fine-resolution (∼25 m posting) bed topography maps over large swaths (∼2 km wide).

4.5.3 Sediment density and layer thickness gravity modeling

To identify spatial patterns in the aerogravity data (see Fig. 4.1b), the gravity disturbance line data (i.e., gravity anomaly using ellipsoid heights) distributed by the PolarGAP survey were gridded using a continuous curvature spline with a tension factor of 0.3 at a horizontal resolution of 1 km. After large-scale features of interest were identified, we conducted forward modeling to identify whether sediment was present beneath topographic basins. The forward modeling of the gravity anomalies for bathymetry and sediment-layer thickness and density is based on the gravity anomaly calculations of Plouff (1976). In this method, the domain of interest is discretized into rectangular prisms composed of ice, sediment, and crystalline bedrock. The prisms used in the discretization have fixed horizontal dimensions (5 km square), but their depth and density can vary according to the different sediment distribution hypotheses we test. We assume a sediment density consistent with seismic and borehole data (2400 kg/m^3) and vary the basement depth according to the position of the basins identified by Winter et al. (2018). The total gravity anomaly at a given point is computed as the sum of the contributions from all prisms. We account for regional gravity-anomaly fields by calculating the long-wavelength Bouguer gravity anomaly from satellite gravimetry and assume that this gravity anomaly is caused by variations in crustal thickness. We compare solutions for the gravity anomaly with observations and the null hypothesis that the basins contain no sediment. In all cases, we improve the fit to the gravity observations when we include sediment in the basins compared to the simulation where we assume there is no sediment.

4.5.4 The effect of fault-bounded ice streams on timescales of ice-sheet advance

We use a reduced marine outlet glacier model (Robel et al., 2018) to assess what past streaming flow near Hercules Dome implies for past regional ice dynamics. The model describes an idealized outlet glacier system with two dynamical stages. In the first stage, accumulation (S) falls in the interior catchment of length (L). This surface-mass-balance flux $L \cdot S$ is balanced by ice flow towards the outlet-glacier margins (Q). The interior flux, Q, has the general form

$$Q = \left(\frac{\rho_i g}{C}\right)^n \frac{H^\alpha}{L^\gamma}. \tag{4.1}$$

where ρ_i is ice density, g acceleration due to gravity, and C a friction coefficient assuming Weertman-type sliding. n is the flow-law exponent, H is the average interior ice thickness, and α and γ depend on the partitioning of stress accommodated by internal deformation and basal traction.

The interior reservoir of the outlet glacier drains according to this interior flux until it reaches a second conceptual reservoir near the grounding line. Here, stresses change as the glacier goes afloat, and the characteristic thickness (h_g) corresponds to the flotation thickness. The grounding zone flux (Q_g) is given by

$$Q_g = \Omega h_g^\beta, \tag{4.2}$$

where Ω and β depend on assumptions about glacier sliding and ice-shelf buttressing (e.g., Schoof, 2007; Haseloff and Sergienko, 2018). Two coupled equations describe the evolution of H and L as the glacier adjusts towards a balance of accumulation, ice flow, and discharge:

$$\frac{dH}{dt} = S - Q/L - H/(h_g \cdot L)(Q - Q_g) \tag{4.3}$$

$$\frac{dL}{dt} = \frac{1}{h_g}(Q - Q_g). \tag{4.4}$$

Descriptions of these kinematic fluxes ($L \cdot S$, Q, Q_g) with time series of forcing (e.g., perturbations in S or Q_g) form a closed system of ordinary differential equations that describe glacier response to climate forcing. These equations can be linearized about small

perturbations to equilibrium length and interior thickness to understand the dependence of the glaciological filtering properties of marine outlet glaciers (Robel et al., 2018). Solutions to this linear system of equations in the case of stable geometries reduce to the sum of two linearly-independent exponential functions with analytic expressions for eigenvalues that can be ordered to characterize the slow (τ_s) and fast (τ_f) response times of the conveying ice stream (Robel et al., 2018; Christian et al., 2020). We focus on interior perturbations in cumulative surface mass balance variability because the early advance of marine-terminating outlet glaciers must be driven by accumulation (Robel et al., 2018). The system of equations can be projected onto its eigenmodes and sorted according to the timescales of the glacier's length and thickness response, where m_s is the slower mode and m_f is the faster mode:

$$\frac{dm_s}{dt} = -1/\tau_s m_s + \sigma_s f(t) \tag{4.5}$$

$$\frac{dm_f}{dt} = -\frac{1}{\tau_f} m_f + \sigma_f f(t). \tag{4.6}$$

We focus on the slow mode, associated with the adjustment of interior ice, in our parametric evaluation of glacier advance sensitivity, which ultimately paces the full response of stable advance or retreat on millennial and longer timescales. The slow response time can be estimated (Robel et al., 2018) as

$$\tau_s = \frac{\bar{H}}{\bar{S} - s_T \alpha}(\alpha + 1/m + 1 - s_T) \tag{4.7}$$

Total flux in the model is dictated by assumed accumulation and catchment area; we can then solve Equation 4.1 for the implied thickness and use this thickness to calculate the slow response time. The equilibrium thicknesses and response times were calculated for combinations of sliding parameters and accumulation that resulted in the same equilibrium length using an implementation of the Adam gradient-descent inverse method. Refer to Table 4.1 for a comprehensive list of parameter descriptions and values.

With a model that appropriately complements the weak constraints on ice geometry at the time of glaciation and a metric for evaluating the "glaciological filter" associated with the early ice-sheet response, we can understand how the valley troughs and trough basins associated with fast outflow affect ice-sheet nucleation and regrowth. Full-Stokes

model simulations of Thwaites Glacier using high-resolution swath-mapped grids indicate that lineated features are typically associated with low basal drag environments compared to rough ridge-like features (Hoffman et al., 2022), such as the glacial highlands we image at Hercules Dome. Here, we evaluated the sensitivity of characteristic ice thickness and response time to different parameterizations of basal sliding and specifically assessed how the new features that we image at Hercules Dome, typically associated with rapid ice flow, may reflect conditions that promoted ice-sheet advance between collapse cycles.

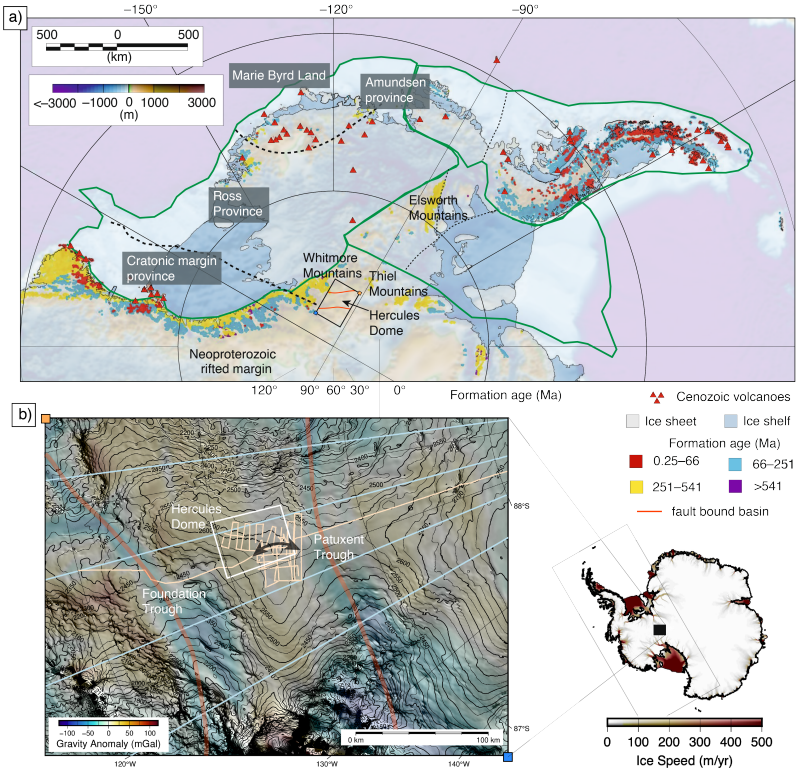

Figure 4.1: (a) Overview of the basins and provinces with formation ages of outcrops in West Antarctica overlaying the ice-sheet bed topography (figure modified from Jordan et al. (2020a)). (b) An overview map of Hercules Dome with interpolated aerogravity surface anomaly shown with composite MODIS imagery (Haran et al., 2018). Also plotted are the radar profiles (light orange) from this study and flight lines of aerogravity data (light blue) collected with airborne radar observations as part of the PolarGAP survey (Winter et al., 2018; Jordan et al., 2018). Inset shows locations of panels a and b in Antarctica. Black arrows denote flow-axis inferred from bedforms and the valley axis imaged in subglacial topography. Dark orange lines indicate the approximate position of the basin troughs likely associated with past tectonism.

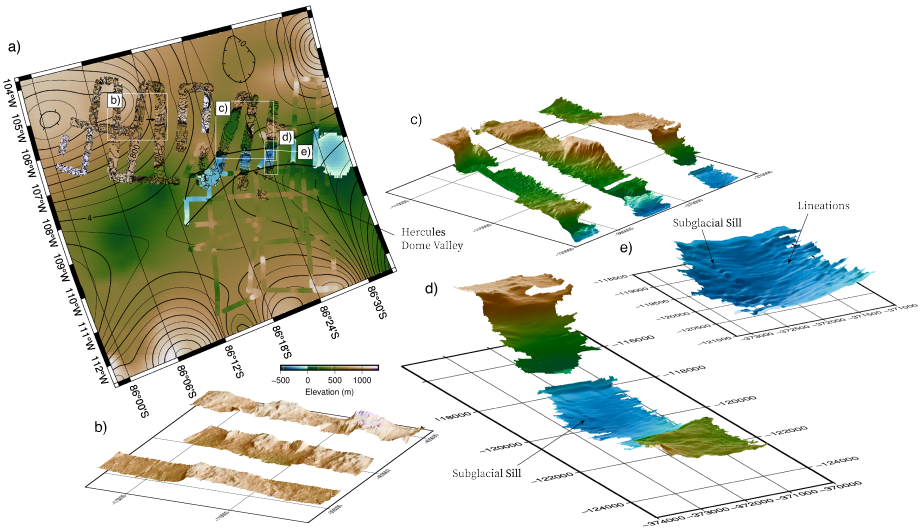

Figure 4.2: (a) Swath bed elevation overview created by geolocating off-nadir energy using the multi-element swath radar overlain over spline interpolated bed elevation (Morlighem et al., 2020) in the white region shown in Fig. 4.1b. Revealed in these radar swaths is evidence of (a) U-shaped valleys, host to subglacial water; (b, c) landscapes characteristic of glacier highlands; and (d, e) glacial lineations and sills within the Hercules Dome valley.

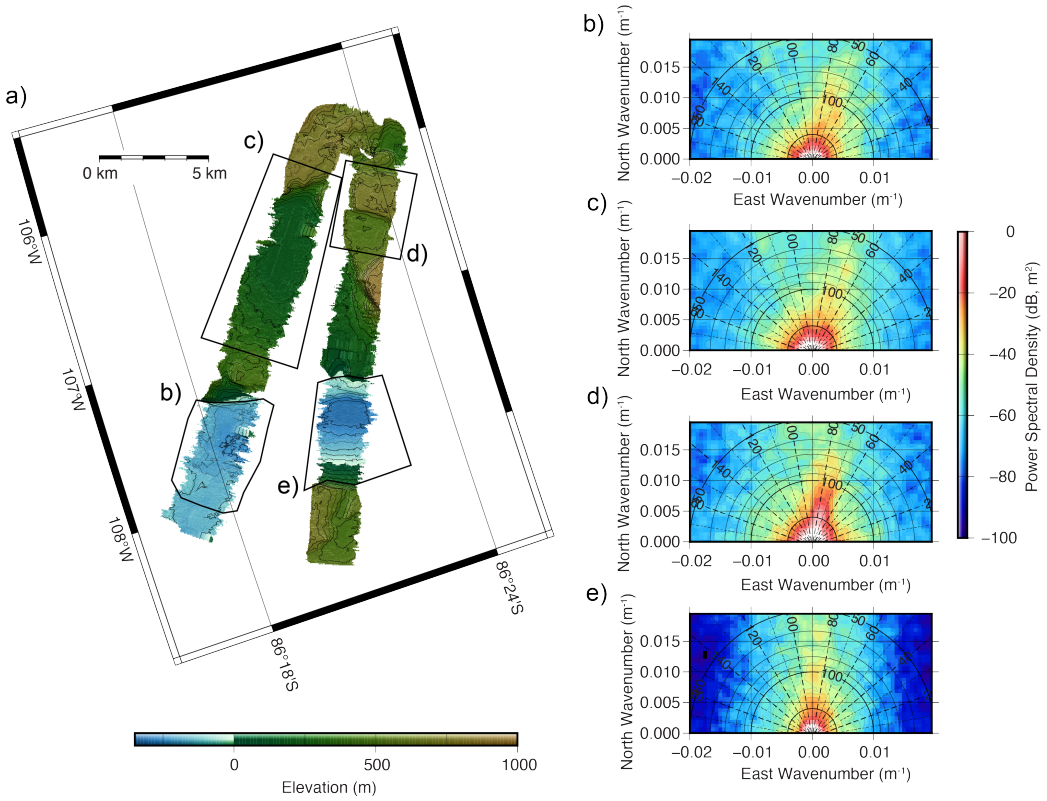

Figure 4.3: Spectral analysis of local subglacial topography in the glacier highlands (c,d), and valley floors (b, e). Black solid lines in Fourier analyzed panels of each outlined domain denote wavelength (in meters) and black dashed lines indicate orientation (azimuth with 45° marking NW-SE features and 135° marking NE-SW features). Colors capture the power (decibels) of spectral energy relative to the direction of the survey.

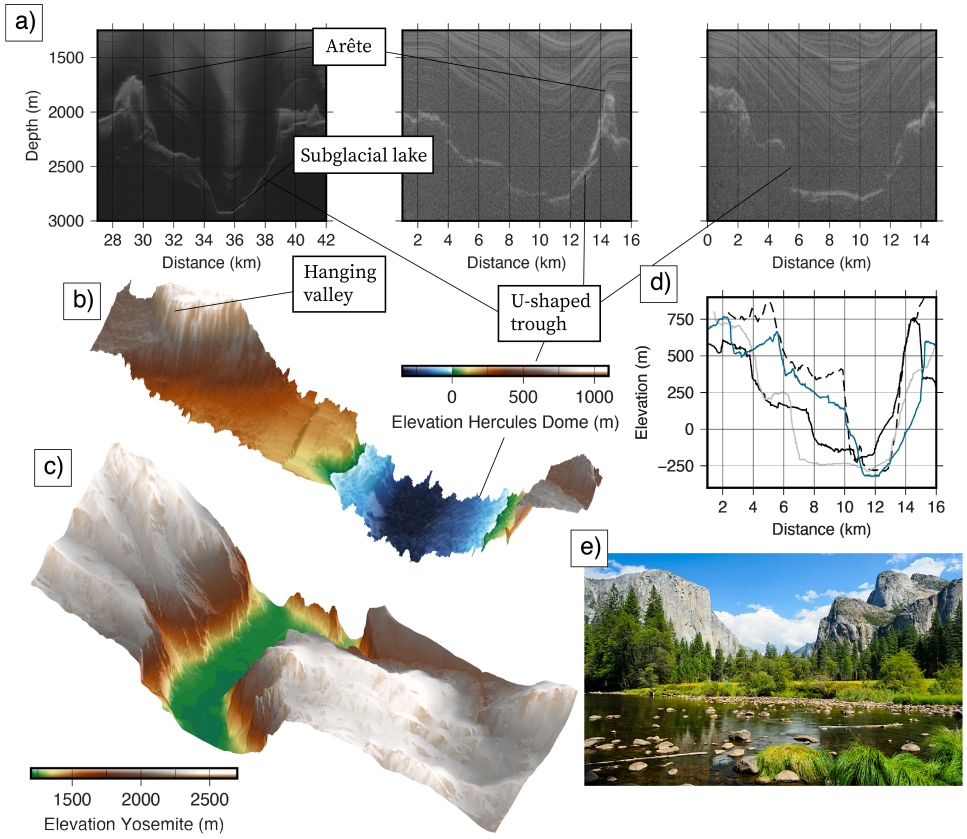

Figure 4.4: Profiles of (a) U-shaped valleys we image with nadir-focused multichannel radar and high-frequency impulse radar at Hercules Dome (note candidate subglacial lake water in trough bottom of the first radar profile), and (b) swath radar digital elevation model of the trough at Hercules Dome with (c) offset elevation model captured by lidar (USGS, 2021) of the Yosemite Valley (panels (b) and (c) have the same vertical scale). Profiles in panel (d) correspond to the bed elevation profiles from Hercules Dome radio echograms shown in panel (a; blue, black, and gray) with a profile of El Capitan (dashed black) in (c, e) the Yosemite Valley. Many large-scale ($>$ 1 km) landforms observed in these profiles are characteristic of deglaciated landscapes.

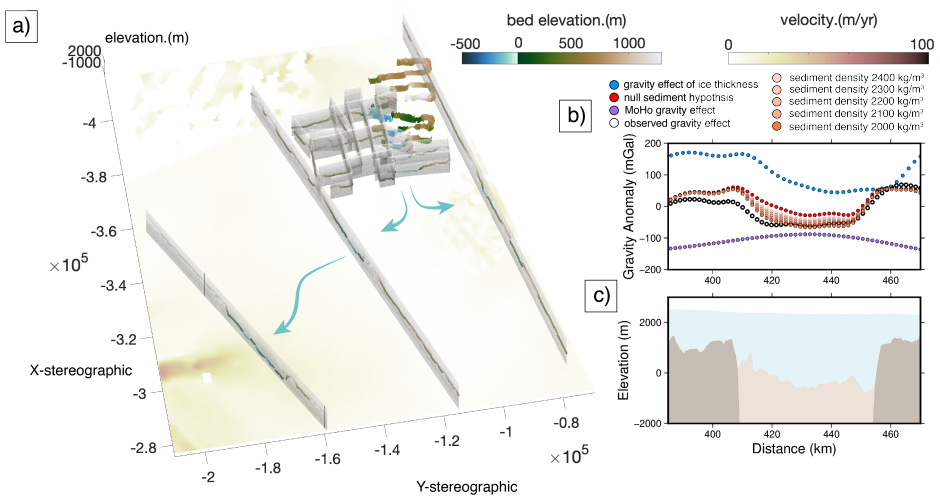

Figure 4.5: (a) High-frequency impulse and swath radar data with flow paths through the Hercules Dome valley into the Patuxent Trough. The regional surface velocities (Mouginot et al., 2019) are plotted in background. Also shown (b) are the gravity modeling results of the (c) PolarGAP transect across the Patuxent Trough. In the PolarGAP transect, blue curves show the gravity effect of ice thickness, purple curves indicate the sum of the Moho gravity effect, and orange curves represent the sum of these contributions with sediment density hypotheses that can be compared with observations (black). Because gravity solutions associated with substrate density and depth are non-unique, we held the sediment thickness constant and used different hypotheses for sediment density to evaluate the likely presence of a sedimentary basin hosted within the Patuxent Trough.

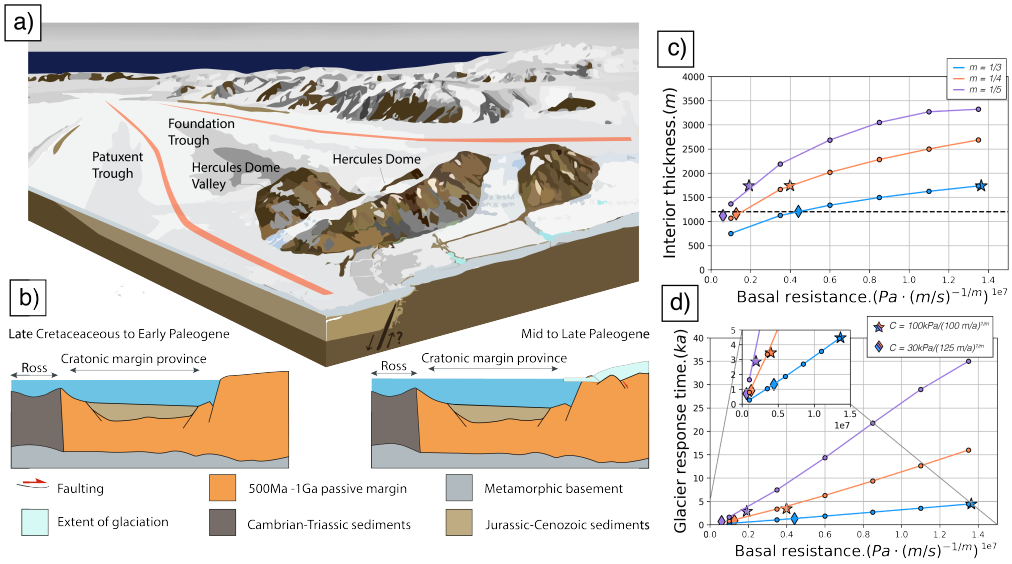

Figure 4.6: (a) Illustration of an early West Antarctic ice sheet with an open Ross Sea and alpine glaciers flowing from Hercules Dome into the neighboring rift system as viewed from the Filchner-Ronne sector looking towards the Ross sector. (b) Geologic cross-section of the evolution of the West Antarctic rift system and the West Antarctic ice sheet in the Late Cretaceous and the onset of glaciation (modified from Jordan et al., 2020a). (c) The equilibrium interior ice thickness estimated by an idealized model, associated with different parameterizations of glacier sliding. Stars indicate the resistances and associated thickness corresponding to rough highland-like features. Diamonds indicate the resistances and thickness inferred for lineated regions. The dotted black line indicates the approximate depth of the glacially incised trough, which provides a bound for the ice thickness when the trough was formed according to theory predicted by Harbor and Warburton (1993). (d) Interior transport timescale associated with different parameterizations of glacier sliding.

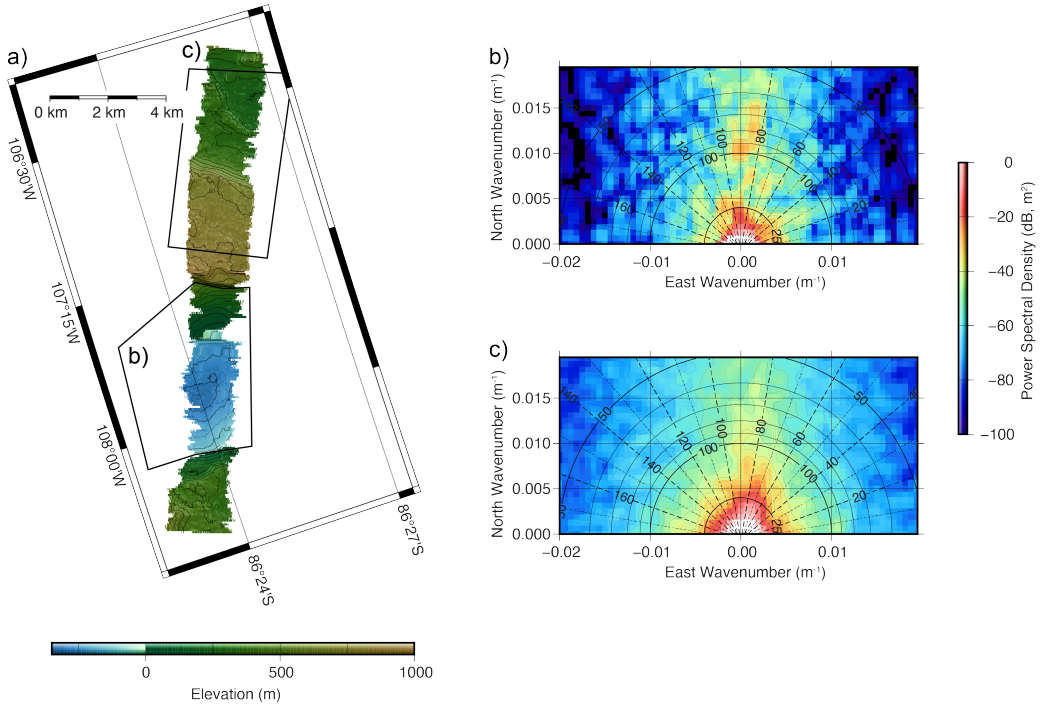

Figure 4.7: Spectral analysis of local subglacial topography in subglacial valley (b) and highland (c) environments along a continuous swath profile. Black solid lines denote wavelength (in meters) and black dashed lines indicate orientation (azimuth with 45° marking NW-SE features and 135° marking NE-SW features). Note that energy is particularly directed in the valley, with more energy along the valley axis.

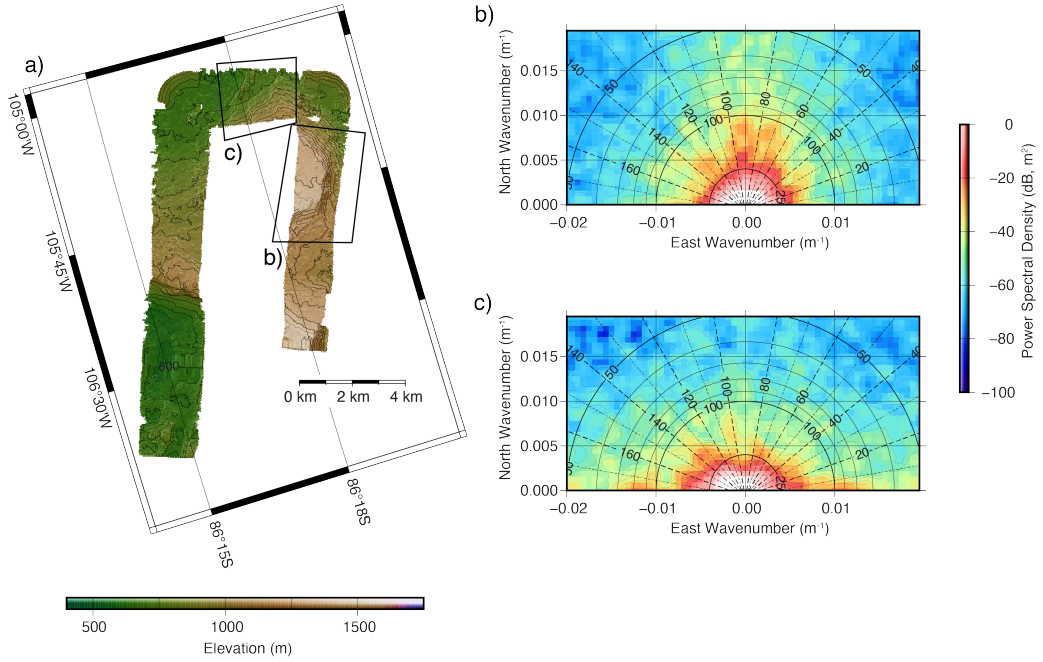

Figure 4.8: Spectral analysis of local subglacial topography in the subglacial highlands. Black solid lines denote wavelength (in meters) and black dashed lines indicate orientation (azimuth with 45° marking NW-SE features and 135° marking NE-SW features). Note that highland roughness has high power oriented in all directions compared to valley floors imaged elsewhere in swath topographies where energy is greater along the valley axis.

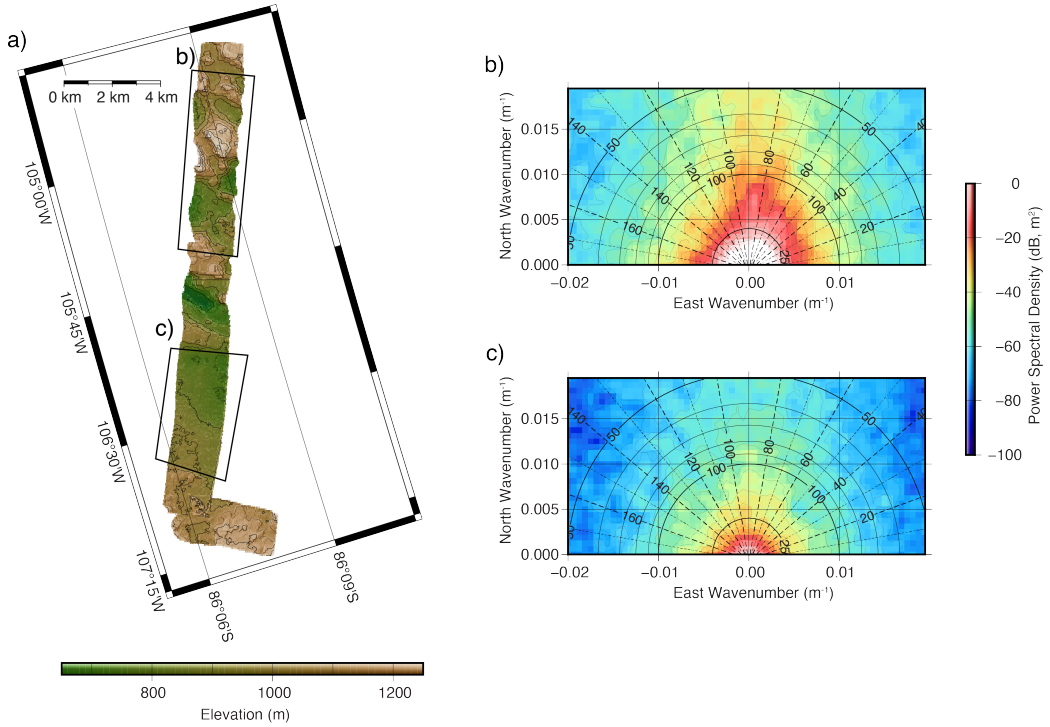

Figure 4.9: Spectral analysis of local subglacial topography in the subglacial highlands. Black solid lines denote wavelength (in meters) and black dashed lines indicate orientation (azimuth with 45° marking NW-SE features and 135° marking NE-SW features). Note that highland roughness has high power oriented in all directions compared to valley floors imaged elsewhere in swath topographies where energy is greater along the valley axis.

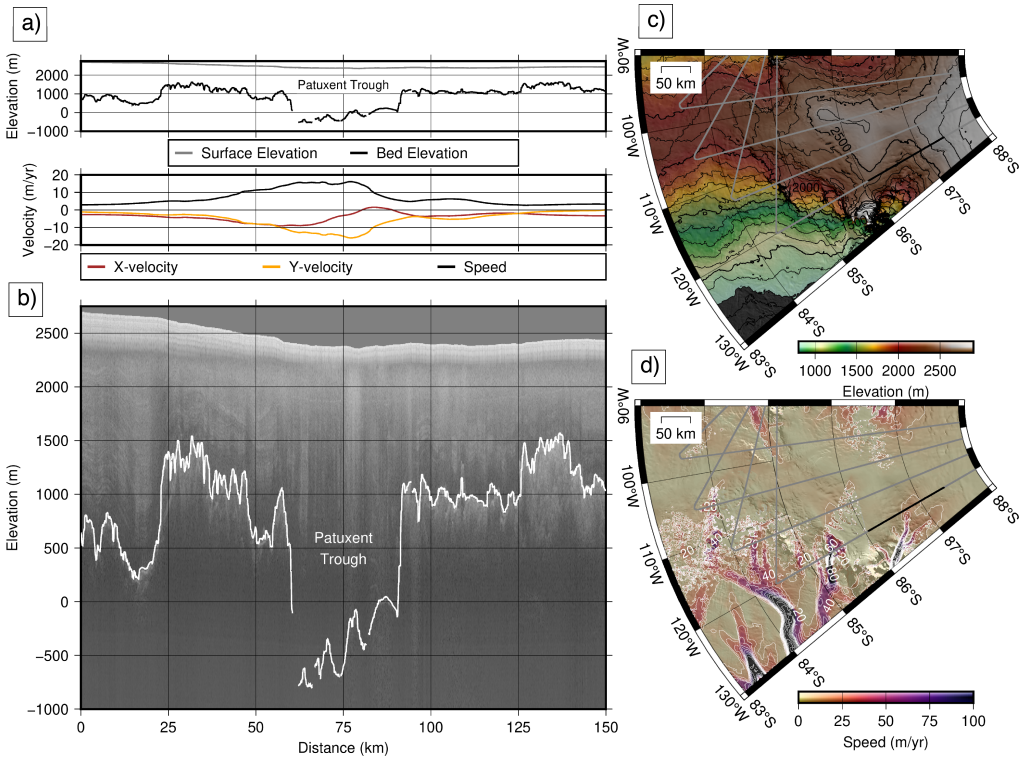

Figure 4.10: Influence of basin location on inland ice velocity (Mouginot et al., 2019) and surface elevation (Howat et al., 2019). (a) surface elevation and velocity along the PolarGAP profile (in thick black in panels b and d) and (b) radio echogram with bed pick (white) showing the Patuxent Trough identified by Winter et al. (2018) with (c) the distributed surface elevation and (d) surface velocity.

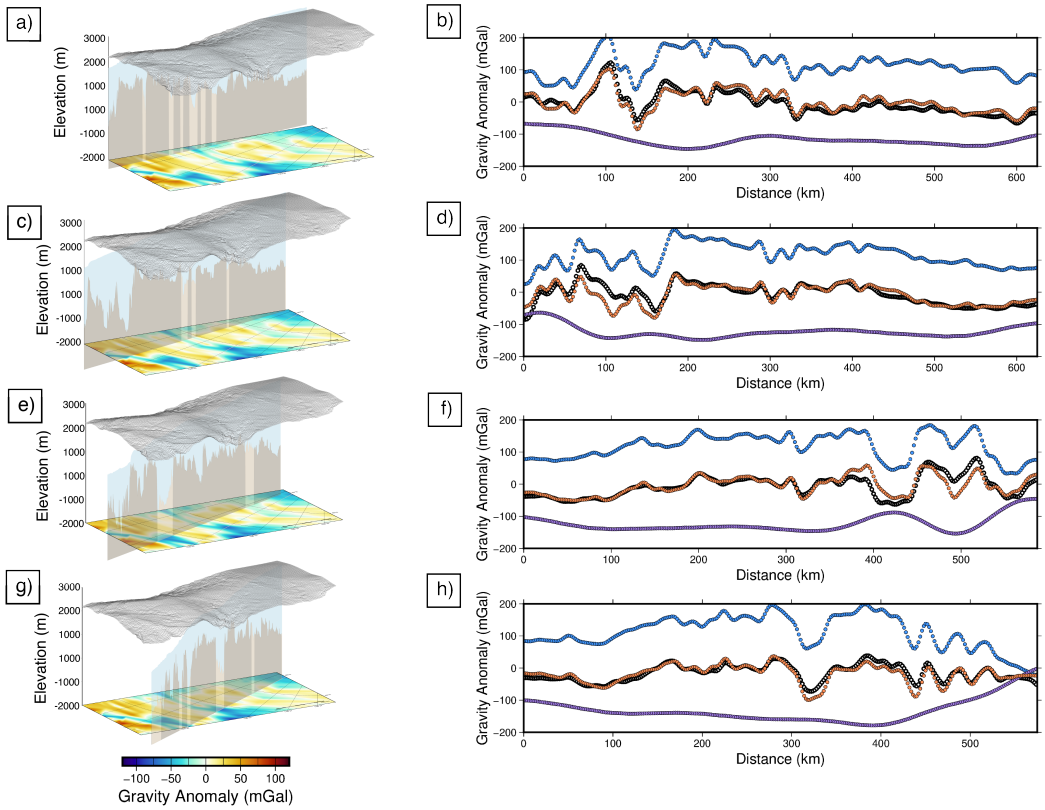

Figure 4.11: (a, c, e, g) Cross-sections of PolarGAP profiles of proposed sediment basin thickness (light brown) and host craton thickness (dark brown) beneath the ice (light blue) shown with a mesh of the Hercules Dome surface topography (Howat et al., 2019). Beneath each profile is the observed composite surface gravity anomaly determined from satellite and airborne data. Also shown (b, d, f, h) are the gravity modeling results of the PolarGAP transects and the gravity anomalies observed from airborne geophysics. Blue curves show the gravity effect of ice and sediment density and thickness, purple curves indicate the sum of the Moho gravity effect, and orange curves represent the sum of these contributions that can be compared with observations (black).

Table 4.1: Overview of the parameters used in the idealized model experiment. The bed-slope parameters and interior bed elevation were chosen based on observed average interior bed elevation and bed slopes of Siple Coast and TransAntarctic outlet glaciers. The choice of these parameters with assumptions for accumulation result in different equilibrium glacier lengths. The relationships we derive for interior thickness and response time hold across choices of glacier length.

Parameter	Description	Value
s_T	Stability parameter that isolates dependence of ice-sheet response on "static" features of conveying ice-stream.	$1 + \frac{\frac{\rho_w}{\rho_i}\left(\beta \bar{b_x} \bar{L}\right)}{h_g}$
α	Parameter that describes partition of stress accommodated by internal deformation and basal slip.	$2\left(\frac{1}{m}\right) + 1$
h_g	Grounding zone thickness.	$\frac{\rho_w}{\rho_i}(\bar{b_x} \bar{L} + b_0)$
β	Grounding zone outflow sensitivity to ice thickness derived from boundary-layer analysis of Schoof (2007)	$\frac{m+n+3}{m+1}$
m	Bed exponent in Weertman basal-sliding relation.	$\frac{1}{3}, \frac{1}{4}, \frac{1}{5}$
C	Friction coefficient	$1e^6, 2e^6, ...10e^6$
b_0	Interior bed elevation (m)	$400, 600, 800, 1000$
b_x	Bed slope	$-2e^{-3}, -3e^{-3}, -4e^{-3}, -5e^{-3}$
$\bar{L}$	Equilibrium glacier length (m)	$200e^3 - 400e^3$
n	Ice flow exponent	3
ρ_i	Density of ice (kg/m^3)	917
ρ_w	Density of water (kg/m^3)	1028

Chapter 5

LATE HOLOCENE STABILIZATION OF CONWAY ICE RIDGE

In this Chapter, we move thematically and geographically from the history of ice-sheet growth and the interior nucleation centers that feed West Antarctic ice streams to some of these ice streams that feed the Ross Ice Shelf. Specifically, we investigate signals associated with changes in the Mercer and van der Veen ice streams that flow around Conway Ice Ridge, formerly known as Ice Ridge A . Here we look in ice-penetrating radar data for signs of past fast flow (buried crevasses and layer deformation) associated with changes in ice-sheet behavior as the ice sheet transitioned out of its Last Glacial Maximum state. In agreement with some of the results we found in the interior of the continent that we connect to older deeper structure, our interpretation of radar data collected at Conway Ridge suggests that changes near the ice-sheet terminus (grounding zone) are transmitted fairly rapidly along ice streams to the interior with rapid changes in flow recorded in layer stratigraphy hundreds of kilometers away from the present and past glacier grounding zones.

Chapter 5, Sections 5.1–5.6 and Appendix C, is a maunscript in preparation for submission to *Journal of Glaciology*, authored by A. Hoffman, P. Summers, K. Christianson, J. Suckale, G. Catania, C. Raymond, and H. Conway. The dissertation author was the primary investigator and author of this paper.

5.1 Introduction

Processes controlling the configuration and resulting discharge of ice streams on centennial to millennial timescales are still poorly understood. Spatially distributed observations of surface elevation and velocity are beginning to capture subtle changes that are important for understanding and modeling the ice-stream response to climate variability (Joughin et al., 2002; Mouginot et al., 2017, 2019), but these data are limited to the period when we have reliable satellite observations. The ice-penetrating radar data archive can be used to

understand changes in flow encoded in the ice sheet's internal stratigraphy that occurred before the satellite era (Gades et al., 2000; Jacobel et al., 2000; Nereson and Raymond, 2001; Conway et al., 2002; Siegert et al., 2004b; Catania et al., 2005, 2006b, 2010; Holschuh et al., 2018; Hillebrand et al., 2021). Traced and dated layers and layer shapes are still somewhat difficult to unambiguously interpret, however, due to the non-unique effects of ice-flow history on layer geometry (Hindmarsh et al., 2006; Steen-Larsen et al., 2010; Vieli et al., 2007; Bons et al., 2016; Vieli et al., 2018; Gerber et al., 2021). Very few unambiguous tracers of ice-stream flow reorganization exist in the modern radar stratigraphic archive (Conway et al., 2002; Siegert et al., 2004b), and interpretations of stratigraphy often relies on corroboration of results with other contemporaneous data (e.g., cosmogenic nuclides, geopmorphological interpretation, etc.). Emerging techniques that isolate spatial patterns in ice-crystal fabric orientation using polarimetric radar may offer new insights into past flow structure (Jordan et al., 2020b, 2022b; Ershadi et al., 2022; Rathmann et al., 2022; Young et al., 2021a,b), but these data have not yet been collected distributively (Young et al., 2021b; Jordan et al., 2022b). Due to these observational challenges, thermomechanical models have been the primary tools used to understand the mechanics of ice-streams (Raymond, 1996; Jacobsen and Raymond, 1998; Raymond, 2000; Suckale et al., 2014; Perol and Rice, 2015; Elsworth and Suckale, 2016; Meyer and Minchew, 2018; Hunter et al., 2021) and ice-stream behavior on multidecadal and centennial timescales (Gandy et al., 2019). These models have notably focused on the steady-state configuration of ice streams and do not typically treat shear-margin location as a free boundary (Jacobsen and Raymond, 1998; Suckale et al., 2014). Additional constraints on past ice-stream behavior would provide guidance for model development and targeted simulations that could lead to more realistic simulations of ice-stream and shear-margin behavior on short (decadal to centennial) timescales.

Numerous ice ridges are found along West Antarctica's Siple and Gould Coasts, lying between dynamic ice stream systems that drain the West Antarctic Ice Sheet and trans-Antarctic outlet glaciers into the Ross Ice Shelf (Shabtaie et al., 1987; Matsuoka et al., 2015). In the central and eastern Ross Embayment, extensive ice-penetrating radar surveys have revealed shifts in shear-margin positions and ice-stream stagnation and reactivation cycles along the margins of Engelhardt Ice Ridge (Ridge BC) (Clarke et al., 2000; Nereson

and Raymond, 2001; Conway et al., 2002; Catania et al., 2003, 2005; Raymond et al., 2006; Matsuoka et al., 2009a), Siple Dome (Ridge CD) (Gades et al., 2000; Jacobel et al., 2000; Catania et al., 2003, 2005, 2006b, 2010), and Shabtaie Ice Ridge (Ridge DE) (Shabtaie et al., 1987; Nereson and Raymond, 2001), but bed-conformal stratigraphy throughout the whole ice column and the presence of Raymond stacks suggest that the low-deviatoric stresses over these ridges (divide flow) has not changed over the last several millennia (Nereson and Raymond, 2001; Gades et al., 2000; Jacobel et al., 2000; Kingslake et al., 2014). In the western Ross Embayment, Conway Ice Ridge (Ridge AB) and Crary Ice Rise (Bindschadler et al., 1990; Bindschadler, 1993; Hillebrand et al., 2021) do not show similar signs of stability. Crary Ice Rise grounded during roughly the last millennium (Bindschadler et al., 1990), and thus stability is not expected to be observed in internal layers. The history of Conway Ice Ridge is less well-known. Here we present detailed radar surveys collected on Conway Ice Ridge that may elucidate past ice-flow dynamics on the ridge and the adjacent van der Veen (Ice Stream B1) and Mercer Ice Streams (Ice Stream A).

Several lines of evidence suggest that Conway Ice Ridge is less stable then the other inter-stream ridges on the Siple and Gould Coasts. First, satellite imagery and elevation data do not indicate a central well-defined divide like those seen on other ridges (Fahnestock et al., 2000; Nereson and Raymond, 2001). Second, radar surveys (presented in this paper) show no indication of a Raymond stack in the internal layers, which would indicate ice-divide stability on millennial timescales (Raymond, 1983; Vaughan et al., 1999; Conway et al., 1999; Nereson and Raymond, 2001; Kingslake et al., 2014). Radar-detected internal layers across the ridge are disturbed. We also continue to observe synchronous modern change in elevation and velocity above the noise floor of the satellite altimeter and satellite velocity products, whereas the other ridges have more stable ice-flow characteristics in the observational record.

This paper has two primary goals. First, we seek to determine whether changes in the positions of the shear margins of Mercer Ice Stream and the neighboring Whillans and van der Veen Ice Streams are preserved in radar stratigraphy, and whether past shifts in shear-margin positions are consistent with the changes in the surface mass balance and grounding-zone flux that drove large-scale retreat in the Ross Sector of West Antarctica during the exit from the glacial period. Second, we aim to determine whether the modern

ice dynamics are a continuation of similar past changes or represent a new steady state. If the large-scale retreat since the Last Glacial Maximum has ended, more recent changes in ice-stream behavior may be due to primarily internal mass balance instabilities between neighboring ice streams.

We first review the modern observational data available in the vicinity of Conway Ice Ridge, including satellite altimetry, satellite velocity, and GNSS data that reveal modern ice dynamics as well as ice-penetrating radar data that may provide insight into the ice-flow history. We then place our local observations in context with regional changes in the Ross Sector during the Holocene. Finally, we present our conclusions regarding shifts in ice-flow behavior on Conway Ridge as a target for thermomechanical models of shear-margin dynamics.

5.2 Data and Methods

5.2.1 Field Site and Survey Characteristics

Conway Ice Ridge is the westernmost inter-ice-stream ridge in the Ross Sector of West Antarctica (Matsuoka et al., 2015). It is of particular interest because it restricts ice flow from East Antarctica into the Ross Ice Shelf through Mercer Ice Stream. Thus, understanding ice dynamics here offers the possibility of linking geologic history of ice thickness change in the TransAntarctic outlet glaciers with West Antarctic ice dynamics. The ridge was visited in the 2001–2002 and 2003–2004 austral summers. The fieldwork focused on the lower part of the ridge where there are two indistinct ice divides visible in satellite imagery (Fig. 5.1, 5.2a-b). The upper part of the ridge has less structure, and thus interpretations of radar stratigraphy there are likely to be more challenging. During the 2001–2002 field seasons, 47 mass-balance and ice-velocity stakes were installed (Fig. 5.3a). The positions and accumulation at these stakes were measured again in 2003–2004, with two years separation time chosen to allow robust measurements of changes in this relatively slow and dry region. Approximately 300 line-kilometers of high-frequency impulse ice-penetrating radar data were collected each field season (Fig. 5.2a).

5.2.2 Satellite Imagery

MODIS and RADARSAT-1 satellite imagery were used to examine surface morphology and slope. We use the MODIS high-pass band 1 surface morphology mosaic acquired over the 2013–2014 austral summer at 125 m resolution (Haran et al., 2018) to examine features that are associated with surface slope changes, e.g., flow stripes and shear margins (Fig. 5.1). Because many images are combined to make a mosaic with many processing steps (i.e., geolocation, destriping, cloud masking, high-pass filtering, and weighting for image stacking), the mosaic product does not retain a quantifiable relation to reflectance (Haran et al., 2018); thus, our uses are purely qualitative. The RADARSAT-1 Antarctic Mapping Project (RAMP) acquired a complete synthetic aperture radar (SAR) map of Antarctica at 25 m resolution during the RAMP Antarctic Mapping Mission (AMM-1) in September–October 1997 (Jezek, 1999). Although other SAR scenes have been opportunistically collected in this region, the RAMP AMM-1 provides the only comprehensive SAR imagery for Conway Ice Ridge and its surroundings, because this region is too far south for standard data collection using SAR instruments. A regional calibrated SAR backscatter mosaic was created following the workflow of Jezek et al. (2013). This imagery was used to locate surface and shallow subsurface crevasses (Marsh et al., 2021), which may mark indicate past shear-margin positions or incipient shear margins (Retzlaff and Bentley, 1993; Clarke et al., 2000; Smith et al., 2002; Catania et al., 2006b). Subsurface crevasses are challenging to identify in other satellite imagery because it does not penetrate into the subsurface (Jezek, 1999; Marsh et al., 2021).

5.2.3 Velocity Data

We used velocity data from two sources: in-situ GNSS data and satellite synthetic aperture radar (SAR) imagery. Repeat GNSS measurements were made at 47 stake locations (Fig. 5.3a), which were used to determine velocity vectors representative of the ice-flow field between November 2001 and November 2003. Stake locations were measured during both field seasons using GNSS differential carrier phase positioning in a local (east,north,up) coordinate system relative to the base station (King, 2004). Velocity vectors were calculated

by transforming local coordinates to geodetic coordinates and then calculating component position differences between acquisitions and dividing by the time elapsed between measurements. We compare these observed velocities to analytic predictions of deformation velocity at each stake location to determine the likelihood of basal sliding (see Appendix C.3). Final results are plotted in Figure 5.3a as component velocity vectors in a polar stereographic projection (EPSG:3031). We use three SAR velocity mosaics to examine regional ice-velocity changes (Joughin et al., 2002; Scheuchl et al., 2012; Mouginot et al., 2019). Differences of the three SAR mosaics provide spatially-distributed velocity fields to facilitate our discussion of observed recent changes in flow over the last 25 years (Fig. 5.3b).

5.2.4 Elevation Data

The Ice, Cloud and land Elevation Satellite-2 (ICESat-2) has now acquired over three years of surface height data at unprecedented spatial resolution and accuracy (Smith et al., 2020). We use the recently released ATL14 and ATL15 land-ice products to contextualize the changes we observe in surface velocity with changes in elevation observed across Conway Ridge and neighboring Van der Veen and Mercer Ice Streams. We interpolate the reference digital elevation model provided in ATL14 onto the coarser grid for the ATL15 height change time series to produce a time series of elevation change relative to the ATL14 reference digital elevation model. Our analysis of relative height change during the ICESat-2 mission uses only ATL15, but the referenced elevation time series we create allows comparison to elevation measurements obtained using other techniques from other time periods. Elevation change derived from ICESat-2 repeat elevation profiles is shown in Figure 5.3c.

5.2.5 Ice-Penetrating Radar Data

Variations in ice thickness and internal stratigraphy were measured using a custom impulse ice-penetrating radar system operating primarily at a center frequency of 2 MHz, which corresponds to a wavelength of ∼80 m in ice. A few radar lines were also collected with 7-MHz antennas, corresponding to a wavelength of ∼20 m. Radar lines (Figure 5.1a) were chosen to sample both the along- and across-flow topography as well as features of interest

identified in satellite imagery of surface morphology and velocity. Radar data were acquired at a constant distance interval of ∼15 m using an odometer wheel. Horizontal distances between radar traces vary slightly due traversing over variable wavelength sastrugi. Radar waveforms were stacked 300-500 times per trace, with number of stacks determined by driving speeds (time taken to traverse 15 m). Where available, dual-frequency GNSS data are used to determine positions of radar traces. If dual-frequency GNSS data were not collected contemporaneously with the radar data, horizontal radar trace positions were interpolated linearly between end points of the profiles, which have positions determined from dual-frequency GNSS data. Profiles of surface elevations were determined from dual-frequency GNSS data if these data were collected. If GNSS data are not available, surface elevations along radar profiles were interpolated from the Reference Elevation Model of Antarctica (Howat et al., 2019). We confine our surface elevation interpretations from radar data to individual profiles to account for the multi-year temporal offset between the time of collection of GNSS data and optical stereo-imagery used to construct REMA.

Radar data were processed following the workflow of Christianson et al. (2016b) with some modifications. First, a time correction for antennas spacing was applied to account for transmitter-receiver separation. A bandpass filter between 1–5 MHz or 4–9 MHz was applied to the 2 MHz and 7 MHz data, respectively. Geolocation was performed following the procedure detailed in the preceding paragraph. Following geolocation, shorter, spatially-adjacent, or overlapping profile segments were concatenated to facilitate migration and radar interpretation. Along-track time-wavenumber migration was applied to more accurately image subsurface positions and slopes. Migration and conversion of travel time to depth assumed an average radar wave speed in ice of 168 m/μs.

We calculated the corrected bed-returned power and depth-averaged and depth-variable englacial attenuation rates for individual traces using multiple englacial reflectors in each trace (see Appendix C.1 for additional information). These methods depend on several assumptions, most notably lack of spatial variability in reflection coefficient from an internal layer, constant reflectivity between layers, and consistency in source and near-surface characteristics (amplitude radiation pattern, transmitted power, and refractive focusing). Our power correction methods do not depend on assumptions regarding internal-layer or bed-

depth variability or bed reflection power. We use Fourier spectral analysis (Taylor et al., 2004; Bingham and Siegert, 2007) to analyze along-track bed topographic roughness (see Appendix C.2).

5.3 Results

5.3.1 Surface Morphology, Velocity, and Elevation

The surface morphology of Conway Ridge is also distinct from other inter-stream ridges in the Ross Embayment (Fig. 5.1). Unlike Engelhardt Ridge, or Siple Dome, Conway Ridge does not have a single divide (Matsuoka et al., 2015). In addition, the topography slopes relatively steeply toward the grounding line driving flow down the ridge rather than orthogonal to the ridge axis (Joughin et al., 2002; Mouginot et al., 2019). Observations of horizontal surface velocities from GNSS data of stake positions averaged over the two-year period between observations show a complex pattern of velocity (Fig. 5.3a). Unlike the other ridges (Nereson and Raymond, 2001; Matsuoka et al., 2015), there is no clear indication of divide flow. Comparisons of the observed velocities with calculations of the component expected from deformation (based on measurements of ice thickness and slope angle and an estimate of temperature) suggest that in some areas ice is sliding over the subglacial topography of Conway ridge.

The most prominent features of these data that we use to divide the ridge into four regions of interest are:

- Two subtle ice streams flow through the interior of the ridge, one on the south side of Conway Ridge and another on the northwestern side of the ridge, appear to drain much of the ice from the interior of the ridge to Mercer and van der Veen Ice Streams, respectively.

- Near the confluence of Mercer and Whillans Ice Streams, an area of enhanced ice flow from Mercer transports ice across the ridge into Whillans Ice Stream.

These features separate the ridge into four distinct slow-flowing areas that are also consistent with changes in the surface elevation of the ridge (Fig. 5.3c) and surface roughness

revealed in SAR backscatter and passive microwave imagery (Jezek, 1999; Hulbe and Fahnestock, 2004): the northern ridge, the southwestern ridge, the southeastern ridge, and the promontory near the confluence of Whillans and Mercer Ice Streams (Fig. 5.1a). On the northern half of the ridge immediately adjacent to van der Veen Ice Stream, the surface is smooth in both SAR and MODIS imagery and qualitatively looks similar to the currently inactive Siple Ice Stream (Jacobel et al., 2000; Catania et al., 2005), which lies between Siple Dome and Bindschadler Ice Stream. The southern half of the ridge towards Mercer Ice Stream has a rougher surface morphology and can be subdivided into two ridges (the southeast and southwest ridges) separated by an area of faster flow. On the western side of the southwestern ridge, near the confluence of Mercer and Whillans Ice Stream, the surface morphology is generally smooth, but is interrupted by several depressions that run orthogonal to the surface gradient. These cross-cutting features conform to depressions in the bed topography and also mark the current boundaries between stagnant ice flow and a region of faster flow ($\sim$10 m/yr) that transports ice from Mercer Ice Stream into Whillans Ice Stream. We do not observe radar backscatter from high-amplitude linear or arcuate features consistent with surface crevassing (Marsh et al., 2021). This suggests that buried crevasses, if present, are deeper than can be detected by C-band SAR, which can penetrate depths of $\sim$10 m in cold polar firn (Rignot et al., 2001; Marsh et al., 2021). Finally, we distinguish the promontory of this area, where ice is moving slowly relative to the ice stream and inland internal margin surrounding it.

Using the twenty years of satellite observations of surface velocity and elevation in this area, we can also begin to understand ongoing changes in the spatially distributed flow patterns and thickness of the ridge. Ice thickness changes calculated from differences in vertical velocity of the surface (calculated from repeat GPS measurements) and accumulation over the two-year period indicate that the average rate of thickening for the ridge is +1 cm/yr. This result is consistent with a calculation of the flux divergence (using measurements of ice thickness and the horizontal surface velocity field) that suggest the ridge centers are near balance. Two-year averages of gridded elevation change observations from ICESat-2 indicate similar rates of thickening (Fig 5.3c) and spatially mirror changes in surface velocity (Fig 5.3c). Where laser altimetry reveals ongoing thickening, the ice sheet has also slowed down

and where the ice thickness is unchanged, the speed of the ridge is also unchanged over the last twenty years (Fig. 5.3).

5.3.2 Bed Topography

Ice thickness varies from approximately 800 to 1200 m on Conway Ice Ridge (Fig. 5.8; Fretwell et al., 2013; Morlighem et al., 2020). The thickest ice is on the north side of the ridge, towards the currently active shear margin of van der Veen Ice Stream, where there is a well-defined trough that is ∼300 m deeper than the surrounding topography (km 60 to km 70 in Figure 5.6). The current shear-margin position is not obviously connected to this deep trough, indicating that ice flow is not solely steered by bed topography in this location. The interior edge of this trough is ∼10 km outside the current shear margin towards the ridge center. The current tributary of fast flow that cuts through the central ridge axis is also underlain by a wide (∼ 20 km) trough that is ∼ 300 m deeper than the surrounding topography (km 30 to km 50 in Figure 5.5) in its upstream portions. Although this trough becomes shallower as the ice flows downstream into van der Veen Ice Stream (Fig. 5.6), topographic steering likely enhances ice flow for this central tributary. The small tributary that feeds into Mercer Ice Stream is also steered by a bed trough (Fig. 5.8b). Finally, as noted previously, several surface depressions at the ice-stream confluence at the tip of the ridge are underlain by shallow bed depressions (Fig. 5.2). This suggests that broad-scale ($>$ 1 km wavelength) bed topography plays a prominent role in steering ice flow across the ridge.

5.3.3 Bed Roughness

In addition to the large scale variations in topography induced by the prominent troughs, there are also changes in short-wavelength roughness (20 m to 1 km wavelength) across the ridge. This contrasts with nearby inter-stream ridges adjacent to Kamb and Whillans Ice Streams, where beds are smooth outside of streaming flow (Siegert et al., 2004a). Short wavelength roughness ($<$ 1 km wavelength) is not uniformly anti-correlated with ice flow speed at this location, as is generally expected. For example, fast flow in the upper tributary draining

into Mercer Ice Stream occurs over rough short-wavelength topography (first 10 kilometers in Figure 5.6). However, shear margins active today and potential past shear margins are frequently correlated with high-amplitude, short-wavelength (<1 km) bed roughness. Here we discuss three specific examples of changes in basal roughness along profiles that cross areas of the ridge where the modern flow field changes. Then, we discuss bed roughness more broadly over the entire radar survey.

Along the profile near the confluence of Mercer and van der Veen Ice Streams (Fig. 5.4), the current area of fast flow is not confined to an obvious topographic trough. The fastest flow is instead oblique to an area of higher topography. The margins of the current faster flow and stratigraphic features associated with past fast flow (see below), are co-located with short segments of rough bed topography (Fig. 5.4a–c) that are also associated with visible depressions in SAR and MODIS imagery. Buried crevasses terminate in this same area of slightly elevated roughness (near km 8 in Fig. 5.4) and layers become smooth and the velocity slows where the basal roughness dramatically increases near km 20 in Figure 5.4. This inland increase in bed roughness is confined within a larger bed trough.

Further upstream on the ridge, the same general patterns are noted for profiles that cross the entire ridge (Fig. 5.5–5.6). In all areas of currently high ice speed, bed roughness is relatively low, but at transitions in flow speeds in the interior ice streams of the ridge (i.e., internal shear margins within Conway Ridge), the bed roughness increases. On the northern half of radar profile in Figure 5.5, the bed is quite smooth between km 50 and 60, with a small peak in roughness at km 60 and again at the end of the profile. The bed roughness on the profile in Figure 5.6 is slightly elevated in the area of possible past fast flow, but is still lower than at current or suspected past shear margins. In general, peaks in roughness are correlated with stratigraphic features that may indicate past shear-margin locations, as discussed in the following section.

5.3.4 Internal Stratigraphy

The internal stratigraphy of Conway Ridge is more complex than the stratigraphy observed on other inter-stream ridges, where internal layers are smooth and generally bed conformal

or exhibit prominent signs of long-term flow stability, i.e., a Raymond stack (Nereson and Raymond, 2001; Matsuoka et al., 2015). In some of the slow-flowing areas of Conway Ice Ridge, layers can be detected through the entire ice column and are bed conformal, similar to other ice-stream ridges. However, broad areas of complex folding that are not conformal to the bed topography suggest inheritance of flow features that were formed upstream or disruptions due to the migration of shear margins, where complex folds created by strain in the ice are common. We focus on three observations that are geographically linked to connected changes in ice flow on Conway Ridge.

First, throughout the survey where there is modern faster flow, layers are not solely bed or surface conformal and exhibit complex shapes. In these areas, it is also often difficult to detect internal layers in the lower third of the ice column. In areas far from modern shear margins where the flow is slow, we see bed conformal internal layers throughout the ice column (km 0–35 of the profile in Figure 5.5 and km 0–30 of Figure 5.6). Second, on the south side of the southwestern and southeastern ridges and the northeast side of the north ridge, smooth surface conformal stratigraphy is present in the top portion of the ice column but layers are deformed in the lower portion of the column (e.g., km 50 to end of the profile in Figure 5.5). This suggests non-steady ice flow, specifically past fast-flowing ice that has recently slowed. The timing of the slowdown can be determined by tracking the deepest undisturbed layer above the disrupted stratigraphy (Conway et al., 2002). Third, near the promontory, hyperbolic reflectors at depth indicate buried crevasses (Fig. 5.4c–e; Clarke et al., 2000; Conway et al., 2002; Catania et al., 2006b). At the northwestern tip of the promontory, stratigraphy is disturbed below 100 m depth and smooth and surface conformal above 100 m depth on the seaward 20 km of the profile (Figure 5.4). Stratigraphy is smooth and bed conformal throughout the full ice column 20 km inland from the modern confluence tip. The strong direct radar wave arrival prevents further interpretation of stratigraphy in the upper 100 m of the ice column for all data in this survey, so our ability to comment on changes in the recent past (∼1000 years) is limited.

5.4 Discussion

We combine the new stratigraphic observations with interpretations of the regional subglacial landscape and the influence of topography and rheology on surface elevation and velocity to construct a hypothesis for flow changes near Conway Ridge. We contextualize these new geophysical and stratigraphic interpretations with existing regional cosmogenic, geological, glaciological, and ice-core histories of grounding-line position and elevation change along the Siple Coast and TransAntarctic Mountains. We begin by discussing the present ice-flow dynamics. We then discuss past changes suggested by interpretations of internal stratigraphy imaged in the radar data. We then place these local stratigraphic features within the broader history of ice flow in the Ross Sector of West Antarctica during the Holocene. Finally, we discuss whether the modern flow and changes expressed in the 20-year archive of satellite elevation and velocity observations are consistent with past regional changes and mechanisms that have been proposed to explain the modern flow and flow history of the Siple Coast ice streams (Conway et al., 1999; Hulbe and Fahnestock, 2007; Spector et al., 2017; Kingslake et al., 2018).

5.4.1 Bed Topography, Ice Rheology, and Bed Conditions and their Influence on Streaming Ice Flow

Although our radar survey is not dense enough to build a comprehensive gridded bed product, it does reveal features that can be interpreted together with surface velocities and radar-derived bed roughness to understand the three-dimensional structure and flow of Conway Ice Ridge. We first explore the relationship between ice flow and topographic features of varying wavelengths before turning to attenuation and discussing the impact of internal layer geometry on inferred attenuation rates and interpretations of bed reflectivity.

Across Conway Ice Ridge, broad (kilometer) scale topography appears to control ice flow. Current active ice-flow tributaries that transport ice through the ridge are generally steered by upstream troughs (Fig. 5.6), though the expression of the troughs weakens downstream (Fig. 5.5). Where the northern part of the ridge meets the van der Veen Ice Stream, we image half of a modest (∼300 m) trough that extends to the modern shear margin (Fig. 5.6

(60-70km), 5.5 (50-65 km)). The modern shear margin position is not directly pinned by this feature, but the feature does appear to be glacially incised indicating that the van der Veen Ice Stream may have been wider at some point in the past. The inland extent of fast flow along the northwest promontory of the ridge at the confluence of Mercer and van der Veen Ice Streams may also have been limited by a bed trough that is roughly co-located with the onset of bed-conformal stratigraphy. In contrast to the strong controls long-wavelength features place on flow over the ridge, short-wavelength ($20 - 100$ m) features do not appear to be strongly related to ice-flow speed. Some of the fastest ice velocities observed with GNSS are on the interior ice streams on the ridge which flow over rough topography, while at the ridge centers, ice appears nearly stagnant over smooth topography. This may be a result of the survey design as we primarily survey roughness that is transverse to the ice-flow direction, which does not affect basal resistance as much as roughness oriented along flow (Hoffman et al., 2022). Short wavelength bed roughness does, however, appear to be connected with the location of modern shear margins interior to the ridge. Current shear margins of the ice streams that bisect the ridge are located near locally rough beds across the survey. Frequently, localized bed roughness is associated with a large bed trough that geometrically steers flow or persists downstream of large bed troughs that become more muted downstream. Our data do not permit a causal relationship between localized rough beds and shear-margin locations. We simply note that there is an association between shear-margin positions and rough beds when shear-margin location is not clearly correlated with other features in the radar data.

Bed temperature and properties of the substrate in contact with the ice can dramatically change the mechanics governing traction and resistance to flow at the ice-bed interface. Deformable till has been recovered from all of the ice streams where the bed has been accessed and is potentially observerable in the reflectivity of the basal interfaces. After correcting for englacial attenuation, higher amplitude bed returns would be associated with saturated till and generally faster ice flow. Our results for attenuation and geometric spreading corrected power show no strong spatial changes (see Appendix C.1 for details). This could be due to either truly uniform bed reflectivity or data limitations, but we cannot say whether bed conditions (frozen/thwawed or wet/dry) currently exert a strong control on ice flow on

Conway Ridge.

Coupled changes in the surface velocity and ice thickness across the Siple Coast ice streams, particularly Whillans and Kamb Ice Streams, have been connected to changes in the mechanical coupling at the ice-sheet bed, potentially linked water piracy (Anandakrishnan and Alley, 1997; Carter et al., 2007) and basal freezing that accompanies thinning associated with a reduction in ice flux (Joughin et al., 2005). The slowing of Whillans Ice Stream, in particular, is caused by a decrease in the frequency of tidally-induced stick-slip events (Joughin et al., 2005; Winberry et al., 2009) to one event per day instead of two. These ongoing changes are driving Whillans, van der Veen and Mercer Ice Streams to slow, and similar processes have been hypothesized to be responsible for the shutdown of Kamb Ice Stream that occurred ∼130 years before present (Anandakrishnan and Alley, 1997). At Conway Ridge, we observe slowing and thickening of ice-stream tributaries consistent with the interior response to the same downstream slowing mechanism. As the Mercer and van der Veen Ice Streams have thickened and slowed, the backstress these ice streams provide the interior ice streams that flow from Conway Ridge has increased, driving a decrease in horizontal velocity observed at the surface and whole column changes in extensional strain that produce the thickening signals measured with laser altimetry (Winberry et al., 2014; Smith et al., 2020). Changes in shear-margin positions have not been associated with gradual deceleration of the Whillans Ice Stream system, but this could be due to the short satellite observational times series.

5.4.2 Flow Changes Recorded in Internal Stratigraphy

Folds in internal layers fundamentally represent gradients in the history of vertical strain experienced by englacial layers, which are assumed to be isochrones. Although fold geometry depends on the ice-flow history, internal layer folds are difficult to unambiguously connect to ice-flow and bed features for several reasons. In areas where there are large spatial and temporal gradients in strain, ice is often moving quickly, exposing features to additional strain that can further distort the folds. Detailed knowledge of the upstream bed topography and bed conditions is often crucial in order to interpret fold mechanisms that can become

convolved with the history of strain induced by topography and changes in traction at the ice-bed interface (Vieli et al., 2007, 2018). The flux conditions at the boundaries of the ice sheet, including surface mass balance, basal melt, accretion, and grounding-zone flux, can also affect the ice-flow history of folds and other englacial tracers of flow (Ng and Conway, 2004; Catania et al., 2005; Holschuh et al., 2018, 2019; Vieli et al., 2007, 2018). Steady-state assumptions for the basal boundary conditions that describe slip across the Siple Coast are unlikely to be valid (Clarke et al., 2000; Joughin et al., 2005; Hulbe and Fahnestock, 2007; Catania et al., 2012; Beem et al., 2014; Winberry et al., 2014), further complicating interpretations of folds and identification of the origins of these features in this region.

Even if the origins of features cannot be identified, changes in internal stratigraphy can still unambiguously indicate a change in ice-flow conditions. Here our interpretation of stratigraphy as a change in past flow state of the ice depends on three assumptions:

- Reservoirs of slow-flowing ice in the regions of the north and southwestern ridges, where we see undisturbed bed-conformal layering at all depths, are persistent during the time period recorded in the stratigraphy.

- Any deviations from the bed-conformal stratrigraphy that we observe at depth near the shear margins of Mercer and van der Veen Ice Streams are associated with a change in the strain history.

- Deviations in the layer structure and features that we image at depth can be dated using simple one-dimensional models of vertical flow associated with regional accumulation histories derived from the dated stratigraphy of the Siple Dome and Roosevelt Island ice cores.

We interpret features in our radar data from west to east, beginning with the Conway Ridge/Mercer Ice Stream shear margin, progressing to the confluence of Mercer and van der Veen Ice Streams at the promontory of Conway Ridge, then the interior ice stream that terminates into the van der Veen Ice Stream, and concluding with discussions of the northern Conway Ridge/van der Veen Ice Stream shear margin.

We observe complex folds in areas near currently fast-flowing regions of Conway Ridge. Further from these areas, in the interior of the north ridge and southeast ridges the layering is undisturbed. Although data crossing the adjacent Mercer shear margin are limited to a single radar profile, we do not observe buried crevasses or changes in layer geometry that indicate shear-margin migration on this line or on interior lines adjacent to this margin (note bed-conformal layering on km 0–35 of Figure 5.5 and km 0–20 of Figure 5.6).

On the western promontory of the ridge near the current confluence of van der Veen and Mercer Ice Streams (Fig. 5.4), we observe two distinct stratigraphic features that suggest shifts in ice dynamics. Between depths of ∼200 and ∼250 m depth, we observe prominent hyperbolic reflectors from 2.5–4.5 km and 7–9 km on the radar profile in Figure 5.4. Following our assumptions for the regional accumulation rate, these crevasses would have been open at the ice-sheet surface ∼3000 years ago. Stratigraphy is smooth and bed conformal through the ice column farther than 20 km inland from the modern confluence tip, suggesting that rapid flow did not progress inland of this location. Above the crevasses, the deepest prominent continuous layer rests at approximately ∼100 m depth, corresponding to an age of 850–1000 years ago. Stratigraphy above this prominent layer is smooth and surface conformal. Below the hyperbolic diffractors at ∼250 m depth, there are prominent layer folds that are not surface or bed conformal, suggesting they experienced a different strain history. Between these two features, layers are somewhat surface conformal, but are discontinuous. The presence of crevasses suggests that the surface stresses were sufficiently high to fracture the ice ∼3000 years ago, likely indicating close proximity to a shear margin flow and/or flotation (Vaughan, 1993; Colgan et al., 2016; Huth et al., 2021). We interpret the surface conformal, yet still discontinuous layers above the crevasses as evidence of a transition in the strain history of ice in this location. The continuous reflector at ∼100 m depth (850 years before present) may represent the end of the slowing trend at the tip of the promontory when the ice became stagnant (speeds under 5 m/yr), somewhat like it is today. We note that GNSS and satellite data (Fig. 5.2b 5.3) indicate modestly elevated flow (up to 10 m/yr) towards van der Veen Ice Stream inland of the relict crevassing today. This may be the remaining remnant of a past broader region of fast flow from Mercer into van der Veen Ice Stream. The stagnant ice at the ridge tip between this modestly elevated flow though

ridge and the confluence of Mercer and van der Veen Ice Streams is relatively thin compared to ice elsewhere on Conway Ridge (680 m thickness and surface elevation 153 above mean sea level); it is only 60 m thicker than flotation. We suggest that this stagnant portion may be a stranded vestige of past faster, potentially floating ice that thickened enough to ground and then has continued to slowly thicken since the ice was stranded. Thickening rates of < 3 cm/yr between 3000 and 850 years ago would be sufficient to ground the ice at the ridge promontory and obtain the current elevation profile.

Along the southern margin of the interior ice stream that terminates into van der Veen Ice Stream (Fig. 5.7), we also image several prominent hyperbolic reflectors. Again, following our assumptions for the regional accumulation rate, the presence of crevasses (in this case, at depths ∼250 m depth below the surface) in this interior location suggest that the flow through this interior ice stream was faster ∼3000 years ago. In an an immediate downstream orthogonal profile that crosses the interior ice stream closer to where the ice flows in to the van der Veen Ice Stream, layers within the trough that confines the flow of the modern ice stream dip steeply below a depth of 500 m at a much faster rate than the comparatively flat reflectors above (km 35–40 of Fig. 5.6c,d). Profiles that are transverse to the ice flow direction are always more difficult to interpret because the layers do not share the same strain history, but the dramatic increase in the gradient of the dipping layers with depth is consistent with the hypothesis that the draw down through this ice stream was greater in the past than it is today.

Along the northern half of the ridge (up to 40 km from the current shear margin), we also observe stratigraphic features consistent with a change in the strain history of ice adjacent to the modern margin of van der Veen Ice Stream. Here the smoother stratigraphy in the upper ∼300 m is consistent with modern observations of slow flow (km 50-66 of Fig. 5.5 & km 50-85 of Fig. 5.6). The lower three quarters of the ice column contain disrupted, complex layering that suggests ice below this depth experienced a different strain history, changing approximately 3,000 years ago. These disturbed layers associated with prolonged exposure to high strain are unlikely to have formed by acceleration of ice away from the ridge center, as unlike the interior ice stream we image between the northern and southeastern ridge, we do not image topography that could promote flow convergence. We propose instead that

the change in strain history is readily explained by the migration of the southern van der Veen Ice Stream from a more interior location to its current margin position. The location of the layer disturbances supports this hypothesis as the change in stratigraphy occurs immediately adjacent to the van der Veen Ice Stream shear margin, and in conjunction with other observations of slow down from the interior ice stream and the promontory, suggests that van der Veen Ice Stream began to narrow about 3,000 years ago. The last 7.5 km immediate adjacent to the current shear margin are disrupted to more shallow depths (km 65–75 of Fig. 5.6). Here, the deepest continuous layer is only ∼100 m below the surface, indicating that past streaming flow may have persisted until ∼1,000 years ago. The margin appears to have narrowed in two phases: (1) ∼30 km narrowing that began about 3,000 years ago, before a (2) a second phase of approximately ∼7.5 km of migration that ended approximately 1,000 years ago. Unlike the observations over the promontory near the ice stream's confluence, the abrupt stratigraphic transitions suggest that these migratory events happened more quickly, perhaps within a time span approaching the range resolution of the radar data, which equivalent to roughly 250 years of ice accumulation.

Taken together, these observations suggest that ice flow in the vicinity of Conway Ridge began to slow approximately 3,000 years ago and that flow may have stabilized to something similar to its current configuration by about 1,000 years ago, and that this change may have occurred in two steps along van der Veen shear margin. We note that the high-frequency (2 and 7 Mhz) radar data is saturated by the direct wave arrival at depths shallower than ∼100 m. Due to this saturation and the lack of shallower, higher-frequency radar data, we cannot evaluate changes in flow and near surface processes that may have occurred in roughly the last 1,000 years. We also note that although we cannot directly connect the relict crevassing with stratigraphy across the northern half to the ridge, the contemporaneous dating of these events suggests that they may be related. The same shallow continuous layer is observed in both locations. This indicates that the changes we observe on Conway Ice Ridge occur across the ridge and may be connected to broader changes that were contemporaneous across the entire ridge. We next discuss the local shifts in ice dynamics suggested by englacial stratigraphy in context with broader ice-flow changes in the Ross Embayment that occurred as the ice sheet retreated to its present configuration during the Holocene.

5.4.3 Ross Sector Ice Dynamics History

Extensive work over the last several decades has produced a rich record of the ice-flow history in the Ross Sector of West Antarctica since the Last Glacial Maximum. Recent work has resulted in dramatic revisions to the "swinging-gate" paradigm of grounding-line retreat that has persisted for decades (Conway et al., 1999) and suggests that regional ice dynamics may result in relatively short-lived ($< 1,000$ year) grounding-line retreat episodes followed by re-advances after the grounding line stabilized near its current position in the western Ross Embayment roughly 8,000 years ago (Spector et al., 2017; Kingslake et al., 2018). These more ephemeral retreat episodes result from an interplay of ice and solid-Earth dynamics, where grounding-line retreat may be arrested by glacial isotatic adjustment to reduced ice loading, which can lead to re-advance (Kingslake et al., 2018). We next outline the regional history of ice-sheet retreat that may make the Whillans/van der Veen Ice Stream system especially prone to shifts in ice dynamics. Then, we connect our stratigraphic changes to these shifts in ice dynamics recorded in other data.

The swinging-gate hypothesis suggested that grounding-line retreat proceeded steadily inland along the TransAntarctic Mountains while remaining pinned north of Roosevelt Island until about 3,000 years ago when broad inland retreat occurred as the grounding line receded around Roosevelt Island until it stabilized near its current location (Conway et al., 1999). Recent work using cosmogenic nuclide samples collected along the major TransAntarctic outlet glaciers (Beardmore, Shackleton, and Scott Glaciers) (Ackert et al., 2007; Todd et al., 2010; Ackert et al., 2011; Spector et al., 2017) and marine sediment samples collected under the Ross Embayment ice streams (Kingslake et al., 2018; Venturelli et al., 2020) requires fundamental revisions to this hypothesis. These new data suggest that the West Antarctic Ice Sheet was only a few hundred meters thicker at last glacial maximum than it is today and that retreat in the western sector of the Ross Embayment may have started only ∼10,000 years before present rather than earlier (Ackert et al., 2007; Todd et al., 2010; Ackert et al., 2011). Rather than a gradual retreat on the western side of the embayment, the majority of the retreat along the TransAntarctic Mountains occurred by 8,000 years ago (Spector et al., 2017). Fluctuations in grounding-line position since that time have been local and close

(within ∼100 km) to the modern grounding-line position (Kingslake et al., 2018; Venturelli et al., 2020). At least one large-scale (> 100 km) early Holocene fluctuation in grounding-line position has also been documented by carbon dating marine sediments under several ice streams (Kingslake et al., 2018). The only other notable embayment-scale events in the last several thousand years are the retreat of the grounding zone around Roosevelt Island to near its modern position in the eastern Ross Embayment about 3,000 years ago (Conway et al., 1999) and the grounding of Crary Ice Rise that occurred in two phases between 1,100 and 550 years ago (Bindschadler, 1993). The retreat of the grounding line around Roosevelt Island is thought to be associated with broad inland thinning and accelerations of MacAyeal, Bindschadler, and Kamb Ice Streams, which may have resulted in confinement and narrowing of Whillans and Mercer Ice Streams. As the grounding line retreated, glacial isostatic adjustment may have resulted in thickening and readvance. The impact of the grounding of Crary Ice Rise is unclear, but grounding downstream of the Whillans Ice Stream system would be consistent with thickening and slowing of its tributaries (Hulbe and Fahnestock, 2007; Catania et al., 2012). Beyond these embayment-scale events, smaller fluctuations in grounding-line position are likely, but may not be well documented in geological data if they have not triggered changes in ice thickness of TransAntarctic outlet glaciers. These smaller changes in grounding-line position are still a primary control on ice discharge on decadal to centennial timescales, and are important to understanding ice-sheet contribution to sea level on these shorter timescales. We next discuss possible connections between events we infer from radar stratigraphy and both embayment-scale and local shifts in ice dynamics recorded in other data.

5.4.4 Local Changes in Recent Ice Dynamics Associated with Stratigraphic Features

Whillans and Kamb Ice Streams are unusually prone to large fluctuations in velocity and grounding-line positions due to shallow bed slopes and weak basal traction that permit changes in basal or shear-margin dynamics in response to glaciological conditions (changes in ice thickness and basal thermal conditions, Joughin et al., 2004; Hulbe and Fahnestock, 2007; Bougamont et al., 2015), external forcings (such as a sea-level, surface mass balance

and ocean melt, Lowry et al., 2019), or glacial isostatic adjustment (Kingslake et al., 2018; Venturelli et al., 2020). Retreat of the grounding line to near its modern position along Kamb, Whillans, and Mercer Ice Streams suggests that ice-stream stagnation cycles due to dynamic mass imbalances between Whillans and Kamb ice stream may result in local grounding-line oscillations larger than those seen in the observational record (Horgan et al., 2017). Counterintuitively, a slowdown of one ice stream can promote grounding-line retreat and acceleration of the adjacent ice stream due to enhanced lateral spreading from the reduction in ice flux of the neighboring ice stream (Hulbe and Fahnestock, 2007). Observations of changes in thickness near the grounding zones of these glaciers and further inland reveal the complexity of the ice stream's mechanics in response to changes in coupling of the ice-bed interface. As downstream Whillans Ice Stream has slowed, its upstream tributaries (Alley and van der Veen Ice Streams) have thickened (Joughin et al., 2002; Joughin and Tulaczyk, 2002; Joughin et al., 2005; Smith et al., 2005; Beem et al., 2014; Winberry et al., 2014). Meanwhile, upstream tributaries of Kamb Ice Stream have thickened as its downstream trunk has thinned (Smith et al., 2005; Moholdt et al., 2014). Some of these processes have been linked to the eventual recommencement of streaming flow and have been used with reduced models to suggest that ice-stream dynamics can naturally produce oscillatory behavior when forced with stochastic accumulation and temperature variability (Mantelli et al., 2016). Numerous observational and modeling studies indicate that Whillans and Kamb Ice Streams have frequently switched on and off on decadal to centennial timescales due to dynamic mass imbalance between these two ice streams (Clarke et al., 2000; Fahnestock et al., 2000; Bougamont et al., 2003; Hulbe and Fahnestock, 2007; Catania et al., 2012; Bougamont et al., 2015). This evidence suggests that changes in flow near ice ridges along the Siple Coast are not uncommon, and that flow adjacent to Conway Ice Ridge has likely experienced change driven by regional flow reorganization across the Ross Sector and more local changes due to the proximity of van der Veen Ice Stream to Whillans Ice Streams and ice-stream stagnation and reactivation cycles between Whillans and Kamb Ice Streams.

Reconstructions of ice-stream behavior in this region between ∼3,500 years ago and the start of the modern observational era are difficult due to a lack of reliable methods and observational data to unambiguously reconstruct past ice flow. This is due to a variety

of factors including lack of outcrops for sampling and difficulties imaging and interpreting terminal landforms under extant ice streams. Cosmogenic nuclides offer the clearest evidence of past ice thickness, but are limited here in this specific time frame by sampling and proximity. Although outcrops have been sampled along the flanks of several TransAntarctic outlet glaciers (Reedy, Scott, and Beardmore Glaciers), these data are too temporally sparse to provide a record of ice thickness variability over the last 3,000 years (Todd et al., 2010; Spector et al., 2017). The dates of the radar features we document here at ∼3,000 and ∼1,000 years are, however, contemporaneous with two local changes in ice dynamics recorded in other observational data: (1) thinning of Reedy Glacier that occurred about 3,000 years ago documented by changes in the elevation of terminal ponds and moraines (Hall et al., 2016), and (2) a slowdown of Whillans Ice Stream that occurred approximately 850 years ago as recorded by changes in flowstripes visible in satellite imagery (Hulbe and Fahnestock, 2007; Catania et al., 2012).

The first event (∼3,000 years ago) is associated with a change in elevation of terminal ponds along the nearby Reedy Glacier (Hall et al., 2016). Due to a lack of other water sources, most standing water bodies in the southern TransAntarctic Mountains are small, shallow ponds located immediately adjacent to the ice margin. Thus, the past locations of these terminal ponds can be used to reconstruct past glacier terminus positions. Past locations of terminal ponds can be identified as in situ lacustrine cyanobacterial mats in stratified sand, and these cyanobacterial mats can be used to construct a radiocarbon chronology of glacier terminus position. In the case of Reedy Glacier, this radiocarbon chronology combined with the existing earlier cosmogenic nuclide record suggest retreat and thinning started 9,500–8,500 yrs before present (Hall et al., 2016). This early retreat was followed by a period of stability in the middle Holocene, an inference supported by discontinuous terminal moraines in adjacent valleys (Hall et al., 2016). Renewed thinning occurred from 3,700 to 2,400 years before present with little change indicated by the radiocarbon chronology from Reedy Glacier between 2,400 years ago and today (Hall et al., 2016).

This retreat episode is well documented with other dynamic changes associated with enhanced thinning across the Siple Coast and interior of West Antarctica, including migration of flow divides on the other inter-stream ridges (Nereson and Raymond, 2001), changes

in the thinning behavior of western Marie Byrd Land (Stone et al., 2003), and southward migration of an erosional surface caused by a surface slope change recorded as a change in slope of an angular unconformity near Mt. Resnik in the upper reaches of the Kamb Ice Stream (Holschuh et al., 2018). The ultimate cause of all these changes is suspected to be the retreat of the grounding line around Roosevelt Island about 3,000 years ago Conway et al. (1999), but the spatial pattern of grounding-line retreat and thinning has remained unconstrained by available geological evidence. Greater divide migration on Engelhard Ice Ridge in the Holocene compared to the other inter-stream suggests enhanced thinning occurred on Whillans Ice Stream (Nereson and Raymond, 2001). This suggests that grounding-line retreat may have initiated here earlier than 3,000 years ago and that a tongue of marine waters existed in the vicinity of Whillans Ice Stream inland of the current grounding line preceding the retreat past Roosevelt Island. This would be consistent with numerous other studies suggesting early-to-mid Holocene grounding-line retreat along the TransAntarctic Mountains on the western side of the Ross Embayment (Spector et al., 2017; Kingslake et al., 2018; Venturelli et al., 2020). Although we cannot determine the exact chronology of events, initial thinning at Reedy Glacier followed by little change in elevation (Hall et al., 2016) could also be consistent with enhanced flow from grounding-line retreat around Roosevelt Island followed by grounding-line stabilization.

The second change (∼850-1,000 years ago) is associated with both a stagnation of flow at Whillans Ice Stream that is recorded in surface flowstripes and local thickening (Hulbe and Fahnestock, 2007; Catania et al., 2012). This period of ice-stream stagnation is supported by numerical modeling of flowstripe shapes in satellite imagery, with a particular focus on flowstripe deflection around Crary Ice Rise (Hulbe and Fahnestock, 2007). It is unknown whether this shutdown is associated with thickening of Whillans Ice Stream, associated with the two phase grounding of Crary Ice Rise due to glacial isostatic adjustment that occurred at 1,100 and 580 years before present (Bindschadler et al., 1990; Bindschadler, 1993), or was similar to more recent internal dynamic oscillations of fast flow between Whillans and Kamb Ice Streams (Conway et al., 2002; Catania et al., 2006b,a, 2010, 2012). Regardless of the cause of the slowing, thickening of the ice also resulted in regrounding at the tip of Conway Ice Rise at the confluence of Mercer and van der Veen Ice Streams, which likely then resulted

in slowdown and outward migration of the van der Veen Ice Stream shear margin.

5.5 Synthesis

Both of our radar observations of changes in the strain history of ice near shear margins occur contemporaneously with local and embayment-scale changes in ice flow. The slowing and narrowing of the ice stream ∼3,000 years ago may be associated with the last major grounding-line retreat (around Roosevelt Island) that occurred in the Ross Embayment (Conway et al., 1999). Locally, this retreat and eventual grounding-line stabilization may have resulted in thinning at Reedy Glacier followed by little change to the present (Hall et al., 2016). Our radar data indicate that van der Veen Ice Stream narrowed around the time when existing evidence would suggest the grounding line stabilized and that ice at the tip of the ridge may have slowed or regrounded. The second event we note that occurred 1,000 years ago is associated with further narrowing of van der Veen Ice Stream and complete grounding and slowing of ice near the current confluence of Mercer, van der Veen, and Whillans Ice Streams at the tip of Conway Ridge. These events are roughly contemporaneous with the beginning of the stagnation cycle of Whillans Ice Stream that has been noted in surface flowstripes, which may be connected to the grounding of Crary Ice Rise (Hulbe and Fahnestock, 2007; Catania et al., 2012; Bindschadler et al., 1990; Bindschadler, 1993). Despite challenges in determining causal connections, growing evidence supported by our new observations of Conway Ridge stratigraphy suggest that flow slowed and the van der Veen Ice Stream narrowed approximately 3,000 years ago. This slowing is consistent with modern observations of surface elevation and velocity change that suggest that ridge interior ice streams are continuing to negatively accelerate and thicken in concert with the larger Mercer, Whillans and van der Veen Ice Streams.

Our data establish spatial and temporal constraints on changes in the magnitude and position of ice streams that can serve as targets to test ice-flow models that resolve ice-stream margin migration. Here, we outline two types of changes in shear-margin dynamics that occur on different timescales. The first is the slowdown, and likely grounding, of the ice at the tip of the ridge. Our data indicate that this process was gradual and occurred over approximately two millennia. Although the relatively thin ice and stagnant tip suggest

grounding may have occurred, we cannot verify this. If grounding did occur, it would be consistent with thickening of roughly 3 cm/yr over two millennia. Buried crevasses indicate stresses high enough for fast ice flow associated with fracture. The transition from crevassing to disrupted to smooth stratigraphy suggests a gradual transition from fast flow to today's essentially stagnant ice over 2,000 years. This location may have served as both a shear margin and grounding line, presenting a complicated target for model simulations of shear margins, but the thickening rate suggested may be representative of thickening over much of the ridge, and thus useful information for constructing a flux boundary condition consistent with this thickening. The second shear margin shift occurred on the northern half of the ridge towards van der Veen Ice Stream. Although the timing and duration of the margin migration are difficult to determine precisely, the abrupt transitions in stratigraphy suggest they happened over less than 250 years and covered spatial distances of up to 40 km, which present viable limits for models of shear-margin migration.

5.6 Conclusions

Conway Ice Ridge has been considered the least stable of the Ross inter-ice-stream ridges due to its disturbed englacial stratigraphy, lack of a Raymond arch, active ice-stream tributaries that flow through the ridge, and complex surface morphology and topography (Matsuoka et al., 2015). Our ice-penetrating radar, velocity, and elevation data provide new insights into past changes in flow through this ridge. Despite the lack of a Raymond arch and obvious flow divide in imagery, the southwestern portion of the ridge (towards Mercer Ice Stream) is characterized by smooth, surface and bed conformal stratigraphy and shows no signs of disturbances indicative of changes in strain history or shear-margin migration. This southern portion of the ridge has and will likely continue to form a bottleneck to flow from East Antarctica to West Antarctica through Mercer Ice Stream. On the northern side of the ridge, smooth surface conformal stratigraphy overlying disrupted stratigraphy indicate a narrowing of van der Veen Ice Stream and slowing of the northern half of the ridge between 3,000 and 1,000 years before present. Our data also suggest that the ridge expanded seaward, with gradual slowing potentially associated with grounding at the northwestern tip of the ridge during the same time period that the ridge expanded to the north (towards van der

Veen). We are unable to precisely constrain the timescale for shear-margin migration on the northern side of the ridge, but changes in margin position appear to have occurred faster than the vertical resolution of the radar, which suggests a relatively rapid reorganization in less than 250 years.

The events we deduce from englacial stratigraphy are documented in other data. The slowdown we observed beginning 3,000 years ago is likely due to grounding-line stabilization following the retreat of the grounding line around Roosevelt Island (Conway et al., 1999). This event is also noted in nearby changes in ice thickness at Reedy Glacier in the TransAntarctic Mountains (Hall et al., 2016). The stabilization of the ridge we observe 1,000 years before present may be associated with the slowing of Whillans Ice Stream (Hulbe and Fahnestock, 2007; Catania et al., 2012), which may be related to the grounding of Crary Ice Rise (Bindschadler et al., 1990; Bindschadler, 1993) or dynamic mass imbalance between Whillans and Kamnb Ice Streams (Hulbe and Fahnestock, 2007). The contemporaneous timing of the slowdowns we observe in radar stratigraphy with other shifts in ice dynamics suggests our interpretations are robust.

Our detailed radar surveys reveal that ice-stream flow, both past and present, is strongly influenced by bed topography and roughness. Broad-scale bed troughs ($>$ 1 km wavelength) coincide with the locations of the currently active tributaries in the interior ice ridge and inferred past expansions of van der Veen Ice Stream. Active and relict shear margins are co-located with areas of elevated roughness ($<$ 1 km wavelength topography). Despite these bed controls, the ice flow is not solely steered by the bed at any given time. The boundaries of van der Veen Ice Stream today, for example, do not coincide with a prominent bed trough (Fig. 5.6) that is under portions of the ice stream despite no obvious reason they should not. This suggests that other factors, such as drainage imbalances or strain history of the ice, which may affect ice viscosity through temperature and fabric development, may influence shear-margin location, in addition to the bed's prominent role.

Along with guidance on the past history of the Ross Sector ice dynamics, our data and interpretations provide a target for thermomechanical models of ice flow that simulate shear-margin dynamics. Our data specifically provide guidance on two scenarios: (1) lateral shifts in the location of the van der Veen shear margin of $\sim$30 and $\sim$7.5 km that likely occur

on decadal timescales, and (2) a thickening (of ∼60 m) and potential grounding of the ice stream that occurs on centennial timescales. Our radar attenuation analysis is consistent with other work that indicates that ice streams may funnel cold ice from higher elevations, but shear margins may be warmer (though we cannot identify the degree of warming). We hope that these changes in shear-margin position and ice thickness can aid in providing more accurate simulations of shear-margin migration in response to change in discharge flux, which may also provide guidance on other processes at play in shear-margin migration that can now be simulated in state-of-the-art ice-flow models, including shear heating and ice fabric development. Accurate inclusion of these process should allow better simulation of shear-margin dynamics, which are important in determining ice-sheet mass balance on decadal to centennial timescales.

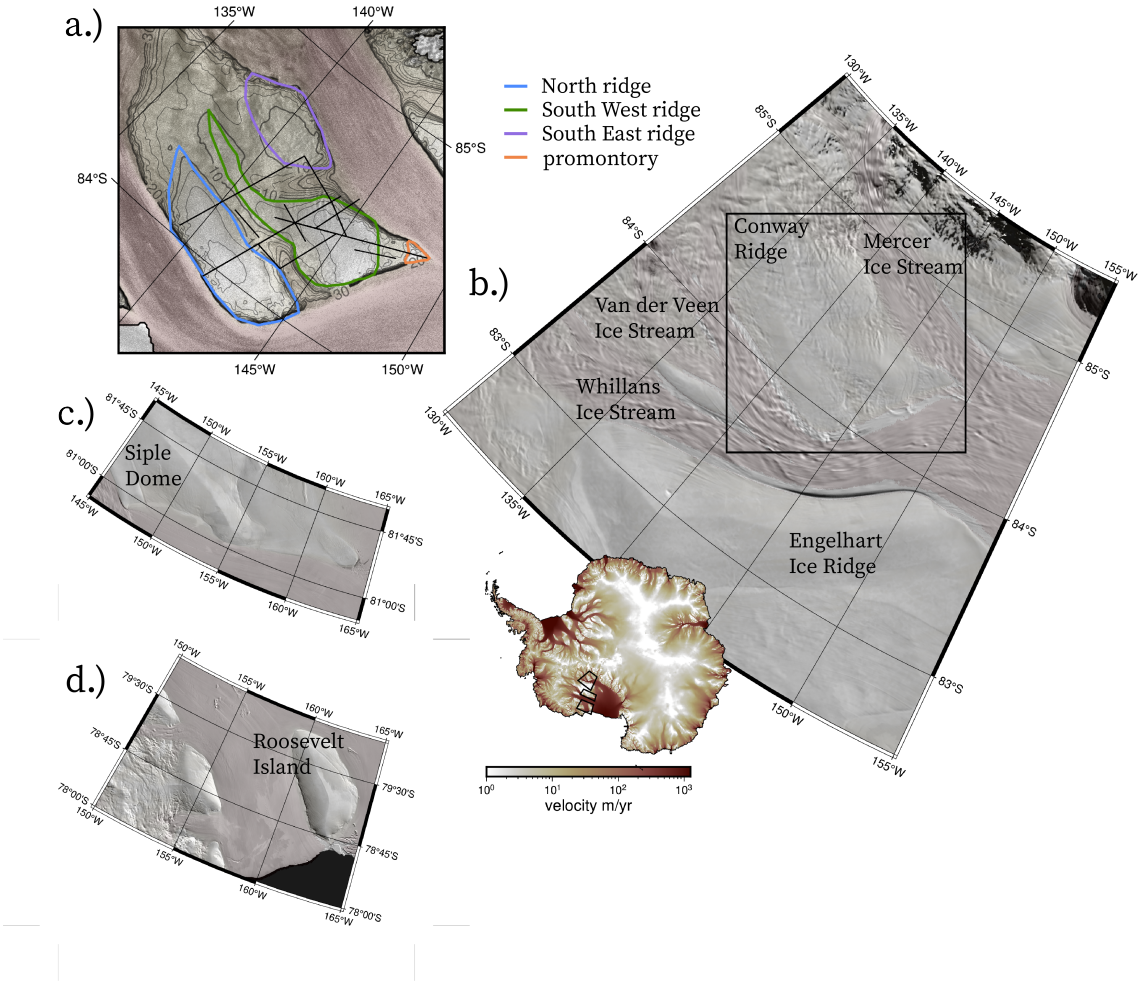

Figure 5.1: Survey overview overlaying MODIS mosaic (Haran et al., 2018) of Mercer Ice Stream, Conway Ridge, and the van der Veen Ice Stream. Red lines indicate radar data and box indicates model domain used to understand margin migration with velocities used to constrain initial inferences of basal strength.

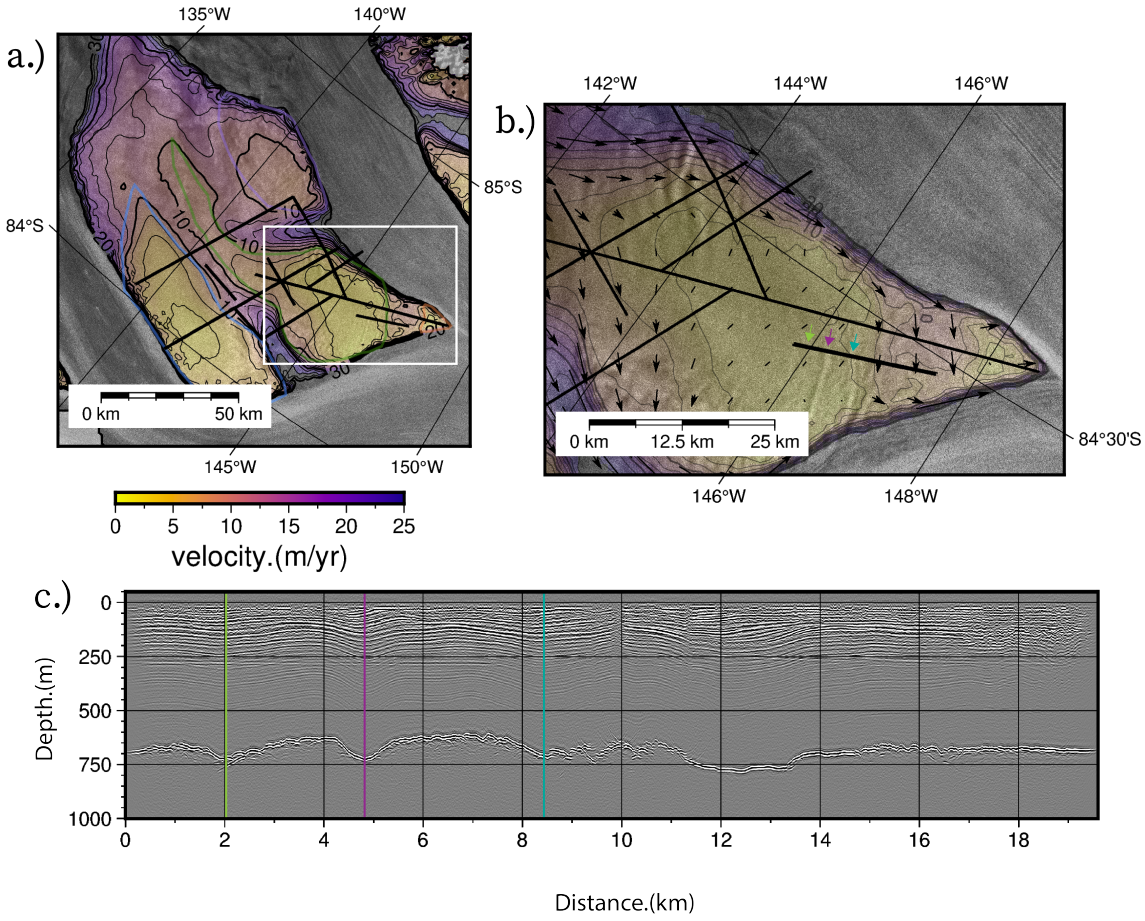

Figure 5.2: (A) Velocity map of Conway Ice Ridge showing radar profiles (black lines). (B) Promontory of Conway Ridge (white box in (a)) showing radar lines and ice-velocity vectors. Colored arrows indicate features labeled in (c). (C) Along-flow radar profile on Conway Ridge. Features marked colored lines correspond to surface features marked by colored arrows in (b).

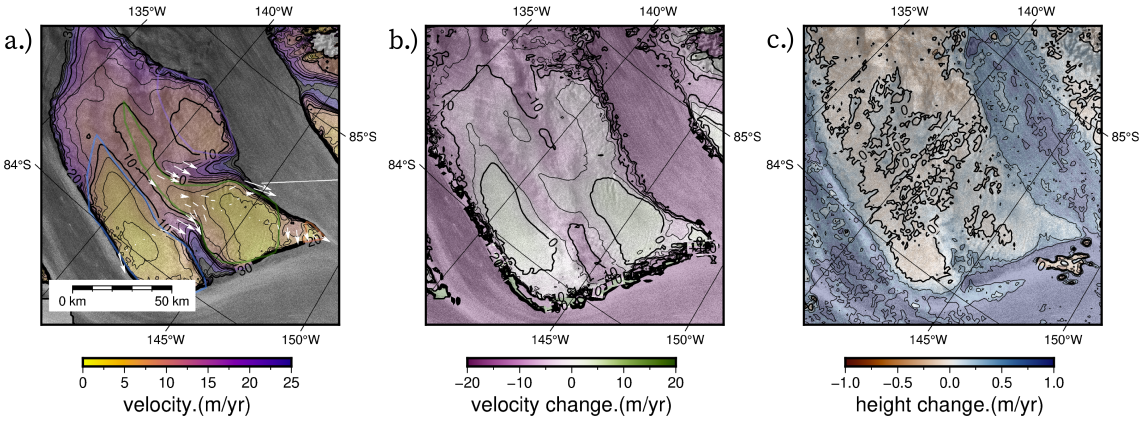

Figure 5.3: (A) Surface velocity with velocity vectors calculated from GNSS data (white arrows), (b) mean velocity change over the last two decades, and (c) elevation change data derived from the average of all 3-month repeats collected as part of the ICESat-2 mission.

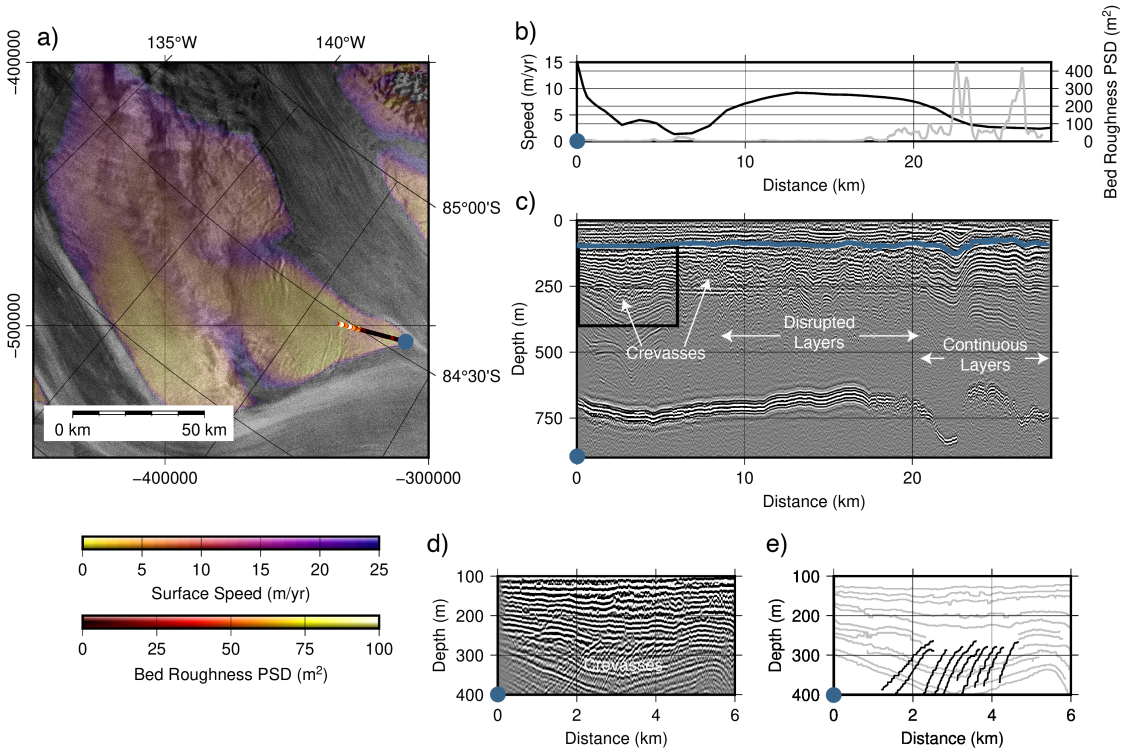

Figure 5.4: Radar profile at the confluence of van der Veen and Mercer Ice Streams on the western promontory of Conway Ridge. A) radar profile location, bed roughness, and speed map plotted on synthetic aperture radar imagery. B) ice speed and bed roughness along the profile as a function of distance. C) Radargram with location of buried crevasses and deepest continuous layer (traced in blue) along the profile with age 850 years before present. Areas of crevassing, disrupted layers, and continuous layers are labeled. Black box shows limits of radargram portion in panel (d). D) Close-up radargram showing buried crevasses (black box in panel (c). E) Interpretation of radargram shown in panel (d). Internal layers and hyperbolic reflectors indicative of buried crevasses are plotted in gray and black, respectively.

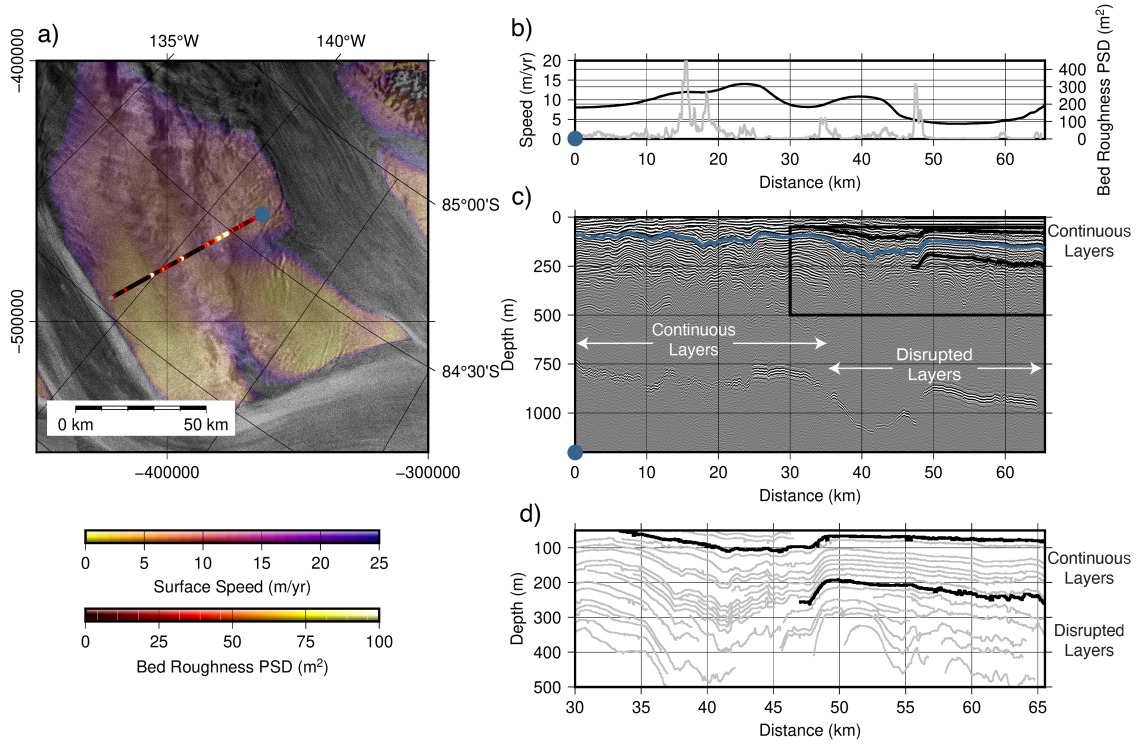

Figure 5.5: Sorthern radar profile across Conway Ridge from Mercer to van der Veen Ice Stream (south to north). A) radar profile location, bed roughness, and speed map plotted on synthetic aperture radar imagery. B) ice speed and bed roughness along the profile as a function of distance. C) Radargram with location of deepest continuous layer (∼850 years before present, and shallowest and deepest continuous layers marking time period of recent slow flow on this former tributary of van der Veen Ice Stream. Areas of continuous and disrupted layers are labeled along the profile. Black box shows limits of radargram portion in panel (d). E) Interpretation of portion of radargram shown in black box in panel (c). From km 50 to the end of the profile, continuous layers between ∼3,000 and ∼1,000 years age (marked in solid black) are above deeper disrupted layers consistent with faster ice flow.

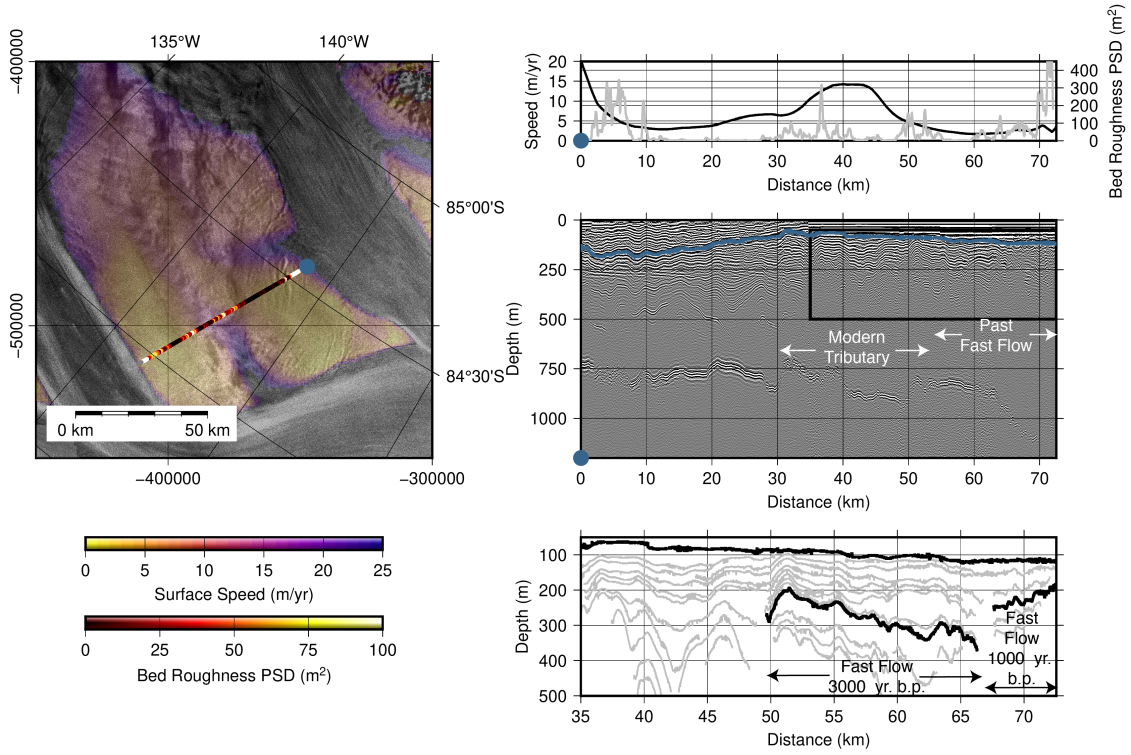

Figure 5.6: Northern radar profile across Conway Ridge from Mercer to van der Veen Ice Stream (south to north). A) radar profile location, bed roughness, and speed map plotted on synthetic aperture radar imagery. B) ice speed and bed roughness along the profile as a function of distance. C) Radargram with location of deepest continuous layer (∼850 years before present. Areas of of modern fast flow and suspected fast flow are labeled along the profile. Black box shows limits of radargram portion in panel (d). E) Interpretation of portion of radargram shown in black box in panel (c). From km 50 to km 65, thick black layers indicate probable slowing between ∼3,000 and ∼1,000 years before present. From km 66 to the end of the profile, fast flow ended more recently, perhaps ∼1,000 years ago.

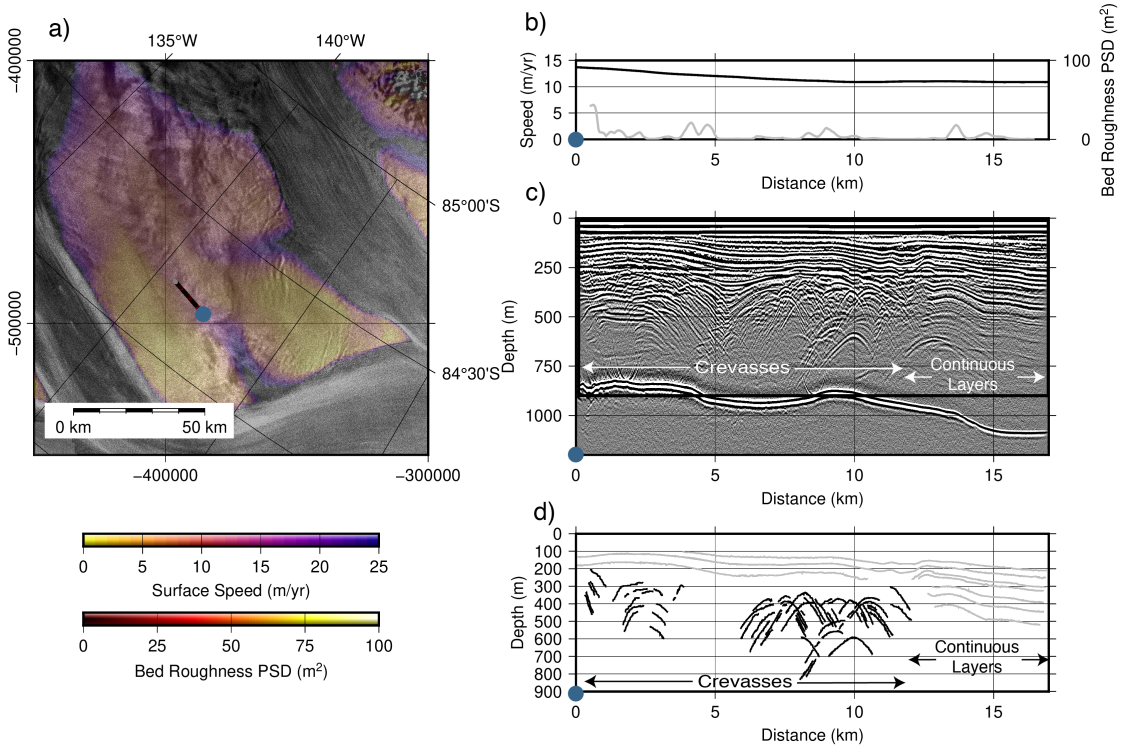

Figure 5.7: Along-flow radar profile in the central tributary of Conway Ridge. A) radar profile location, bed roughness, and speed map plotted on synthetic aperture radar imagery. B) ice speed and bed roughness along the profile as a function of distance. C) Radargram with continuous layers and crevasses labeled. Black box shows limits of radargram portion in panel (d). D) Interpretation of radargram shown in panel (c). Crevasses are consistent with past faster flow in the first two-thirds (downflow) section of the profile.

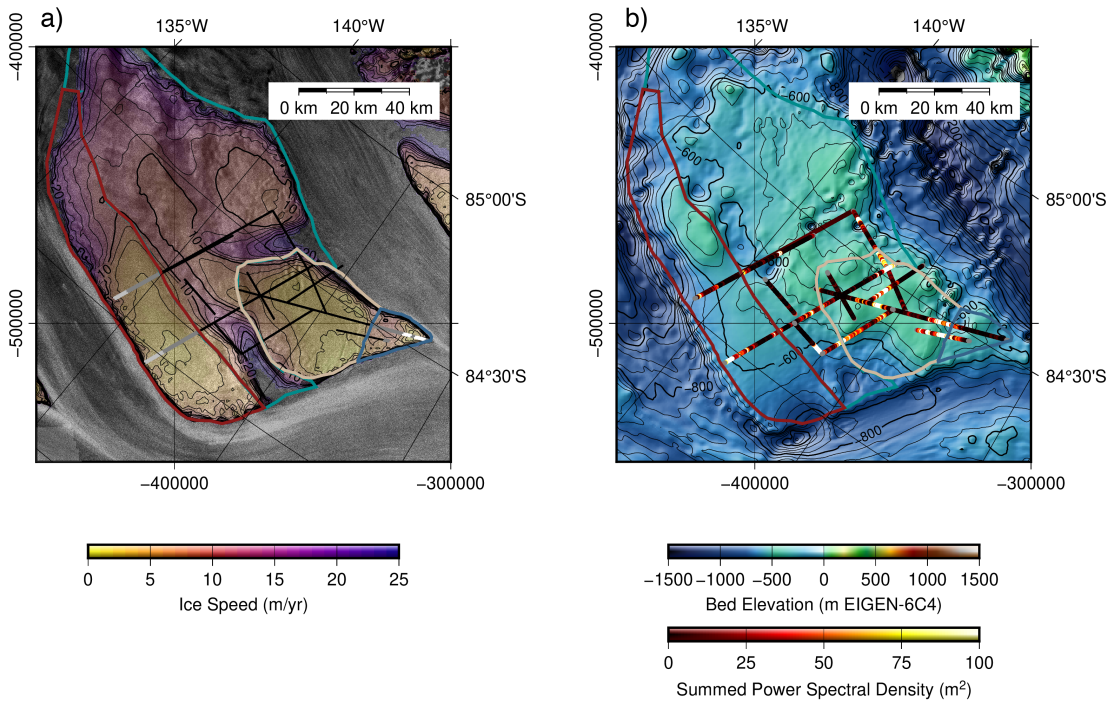

Figure 5.8: Radar survey interpretation plotted on a) ice speed (Joughin et al., 2002) and b) bed elevation Morlighem et al. (2020). In (a), radar profiles are plotted in black. Dark and light gray denotes radar stratigraphic evidence of streaming fast ice flow 3,000 and 1,000 years ago, respectively. White portions of profiles denote locations of buried crevasses. Contours (2 m/yr interval) indicate ice speed. In (b), roughness is plotted along bed profiles. Contours (50 m interval) indicate bed elevation above sea level (relative to EIGEN-64C geoid). In both panels, red polygon denotes formerly active expanded tributary of van der Veen Ice Stream, blue polygon indicates area of fast flow at or near flotation, tan polygon indicates central ridge, and cyan polygon indicates currently active drainages and upper ridge.

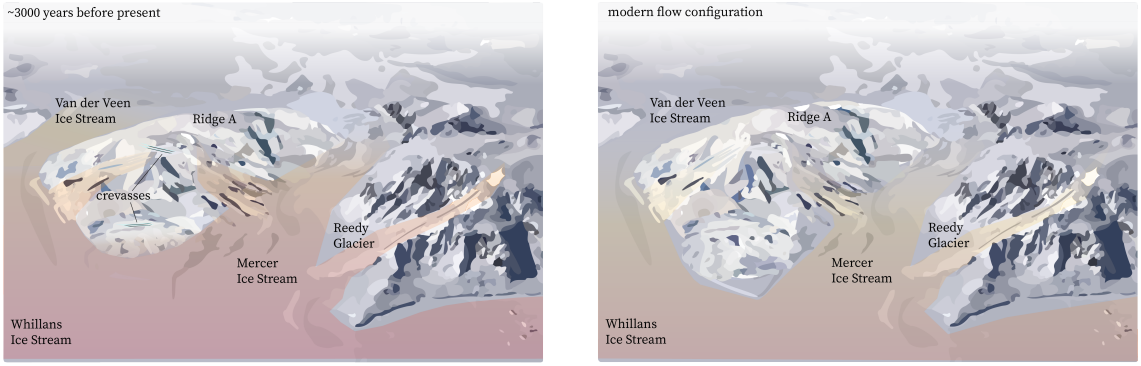

Figure 5.9: Schematic of the changes inferred from radar over the 3,000 years preceding modern observations.

Chapter 6

INLAND MIGRATION OF PINE ISLAND AND THWAITES GLACIER SURFACE CREVASSES IN THE AMUNDSEN SEA EMBAYMENT

In the previous study of the history of ice flow near Conway Ridge, some of the most compelling evidence that revealed how flow near Conway Ridge has changed came from features we interpret as buried crevasses in ice-penetrating radar data. The mechanics of surface fracture in snow, firn, and ice is still an active area of research. One of the still unresolved questions in glaciology is the discrepancy between observational methods that use visible crevasses and fractures in surface imagery that calculate tensile strength using ice-sheet surface strain rates and empirical lab experiments that derive tensile strength from load experiments. Observations suggest that tensile strength of ice is roughly an order of magnitude lower than inidicated by measurements made in laboratories. This discrepancy presents a challenge for models that seek to describe the mechanics of fracture in ice, snow, and firn from first principles.

In this final Chapter, we return to Thwaites Glacier where the material failure of ice has been connected to high mass loss scenarios (DeConto and Pollard, 2016). We use deep learning methods applied to satellite synthetic aperture radar (SAR) imagery to map crevasses in the Amundsen Sea Embayment in time and space. We then use these maps to understand the failure envelopes of the firn and use ice-penetrating radar data to understand the depth and buried nature of these features. We conclude by presenting a model for the fracture toughness of ice that we use to investigate the features we detect in SAR imagery.

Chapter 6, Sections 6.1–6.5 and Appendix D, is a manuscript in preparation for submission to *The Cryosphere*, authored by A. Hoffman, K. Christianson, C.-Y. Lai, I. Joughin, E. Case, J. Kingslake and the GHOST science tream. The dissertation author was the primary investigator and author of this paper.

6.1 Introduction

Crevasses, common to almost all glaciers, are the result of macroscopic material failure due to the progressive accumulation of microcracks and inclusions in glacier ice (Schulson et al., 1989; Vaughan, 1993; Veen, 1999; Colgan et al., 2016). These cracks and inclusions affect glacier mechanics by promoting iceberg calving (Berg and Bassis, 2022), changing the bulk density of glaciers (Meier et al., 1994), and efficiently routing surface meltwater to glacier beds (Zwally et al., 2002; Benn et al., 2009; Colgan et al., 2011). Crevassing also has implications for understanding the bulk physical properties of ice that affect ice flow. For example, the very presence of crevassing, combined with theoretical frameworks for ice fracture and its propagation, can be used to estimate the material strength of firn and ice and its spatiotemporal variability, an important parameter in prognostic ice-flow models. Crevasses also pose a serious risk to personnel conducting scienctific and logistical traverse activities that depend on stable surfaces for safe glacier travel. In this study, we present a six-year time series of inland crevasses in the Amundsen Sea Embayment, West Antarctica, the embayment with the greatest potential to influence global sea-level rise in the coming centuries (Scambos et al., 2017) and where the fracture mechanics of grounded ice have been hypothesized to contribute to rapid glacier retreat in the future (DeConto and Pollard, 2016).

Pine Island, Thwaites, and neighboring Haynes, Pope, and Kohler Glaciers in the Amundsen Sea Embayment (ASE) are losing mass at a greater rate than any other glaciated region in Antarctica (Shepherd et al., 2019; Rignot et al., 2019). Over the last three decades, satellite and ocean observations have indicated that this accelerated mass loss is due to melt from the infiltration of warm modified Circumpolar Deep Water (mCDW) to the ice-shelf base and grounding zone (Jacobs et al., 1996; Jenkins et al., 2010, 2018). Thinning, acceleration, inland glacier retreat, and the inland migration and expansion of crevasses has accompanied the high basal melt. The failure limits of crevassed ice exposed to surface meltwater has been suggested to be important for the acceleration and break-up of Thwaites and Pine Island Glaciers (DeConto and Pollard, 2016; Lhermitte et al., 2020). The rate of retreat for rapid collapse scenarios depends on tensile failure limits of grounded ice (Crawford et al., 2021);

however, observed changes in the crevassing and fracture properties of grounded regions of Pine Island and Thwaites Glaciers have yet to be established or linked to material properties that are used in ice-flow models.

To map crevasse locations from 2016-2022 and determine rates of crevasse area change, we extend deep-learning neural network frameworks (i.e., Ronneberger et al., 2015; Akeret et al., 2017; Lai et al., 2020) to satellite synthetic aperture radar (SAR) imagery collected by the Sentinel 1 constellation from 2016–2022. We use this time series of crevasse locations to test a common phenomenological relationship between surface stress and crevasse nucleation in glaciology: that the presence of crevasses is controlled by a surface stress criterion and the tensile strength of ice (Nye, 1959; Vaughan, 1993, and citations therein). We also present this time series as a test case for fracture and continuum mechanical models that include treatments of the damage history, damage anisotropy, and non-local contributions to damage accumulation (e.g., Huth et al., 2021; Benn et al., 2022). Our results suggest that the tensile strength of the ice-sheet surface is substantially lower than that suggested by laboratory experiments using non-porous ice. Because ice-penetrating radar imagery suggests the crevasses we image are features that occur predominantly in the firn, we suggest that consideration of firn, rather than ice, physical properties is necessary to properly include surface fracture observations in glacier flow models. We use these observations to explore the theoretical development of a geometric fracture mechanical model for polar firn using the crevasse time series and satellite SAR measurements of ice velocity.

In this paper, we first describe the methodology we use to filter and preprocess SAR imagery and the neural network algorithm used to classify and segment crevasses in this imagery. We assess the validity of the algorithm by comparing our results to other methods that can detect crevasses, namely optical and ice-penetrating radar imagery. We then discuss the results of the algorithm's application to the SAR imagery time series, including a summary of the correlation between crevasse expansion and ice velocity for each glacier and the relationship between crevassing and surface stress. Finally, we evaluate failure criteria based on a critical tensile strength of ice and firn and suggest that geometric models of firn properties are a useful avenue for properly relating observed tensile strengths to the physical properties of the fracturing media.

6.2 Data and Methods: From satellite SAR images to maps of crevasse area change

Crevasses at or near the surface of the ice sheet can be difficult to detect in visual imagery due to snow bridges. Surface crevasses covered by snow bridges can, however, be mapped remotely using active microwave synthetic aperture radar (Marsh et al., 2021). Compared to visual imagery, radar imagery is advantageous because it provides continuous observations through clouds, can image features during the polar night, and can penetrate through shallow snow (> 10 m for C-band SAR in polar firn; Rignot et al., 2001). In this study, we use synthetic aperture radar data collected as part of the Sentinel 1A and 1B missions managed by the European Space Agency. The methods described could also be extended to map crevasses using past and future SAR imagery datasets, such as the RADARSAT-1 Antarctic Mapping Project mosaic of Antarctica collected in September and October 1997 (Jezek et al., 2013), TerraSAR data (Marsh et al., 2021), and the future NISAR mission (NISAR, 2018). We first describe the preprocessing steps used to build imagery datasets for neural network training and classification. We then describe the architecture of the neural network, the methods used to recombine classified imagery, and the metrics used to evaluate the methodology.

6.2.1 Sentinel SAR imagery Processing and Analysis

Imagery Selection and Processing

Since 2014, Sentinel SAR 1A and 1B Level-1 Ground Range Detected interferometric wide swath high-resolution amplitude images (∼5 m x 20 m native resolution, HH polarization) were selected geographically using the Alaska Satellite Facility vertex search tool (ASF DAAC, 2022). Images were selected geographically to capture areas that contained the approximate inland crevasse extent in 2014 and 2022. Although we did process imagery for the whole Sentinel archive, our time series analysis focuses on 2016 to 2022 due to changes in scene geometry during the satellite commissioning stage and a melt event in 2015 that substantially affects radiometric backscatter. Here for geometric consistency, we use solely Sentinel 1A frames (see Figure 6.1). Sentinel SAR data are available with a repeat time

of 12 days; shifts in scene geometry can, however, result in less frequent acquisitions for an individual frame. Images with HH polarization were selected because they appear to have the advantage of higher backscatter amplitude than VV polarization, which reduces the effect of random noise (Marsh et al., 2021). Images in both ascending and descending orbits were used to assess possible differences in detectability based on satellite image look angle and crevasse orientation.

Prior to training and classification, all images were converted to radiometrically calibrated backscatter coefficient in unsigned integer 8-bit integer data format. Image processing was conducted using the European Space Agency (ESA) Sentinel Application Platform (SNAP) Toolbox (SNAP, 2022). First, orbit state vectors in the gridded product metadata were updated using precise orbit files supplied by the ESA Global Navigation Satellite System Hub. Several radiometric processing steps were applied including removal of antenna thermal noise, border noise removal which masks null pixels introduced in the creation of the ground range detected products, speckle filtering, and radiometric calibration to backscatter coefficient using Look Up Tables that apply a range-dependent gain including an absolute calibration constant. We applied an ellipsoid correction geolocation-grid operator to convert each image to an orthorectified polar stereographic projection (EPSG:3031) using Sentinel ground-control tie points. Orthorectified images were then resampled to 25 m resolution using a nearest-neighbor interpolation to preserve sharp features. Following radiometric calibration and orthorectification, backscatter coefficients (0 to 1) were converted to unsigned 8-bit integers (0 to 255) and exported as GeoTIFF files.

Neural Network architecture

These preprocessed Sentinel images were then used to train a U-net image segmentation algorithm (Ronneberger et al., 2015; Akeret et al., 2017; Lai et al., 2020). The U-net architecture extends the conventional Convolutional Neural Network (CNN) framework by adding expansive operations (up-sampling layers) to the contracting operations (down-pooling layers) to identify and localize features in an image. The downsampling path followed by the upsampling path resembles a U-shape and gives the network its name.

Network Training

Training data consists of pairs of images and binary classifications for crevassed and crevasse-free regions. Training data were generated using image masking software available at Earth-Masker on Github. The masks were generated by first using a threshold to define an initial binary classification based on the backscatter reflection coefficient – brighter reflections are often associated with crevasses. This binary classification was then refined by manually digitizing crevasses that manifest as arcuate features in these images and deselecting false-positive features. The image training dataset includes images from Thwaites, Pine Island, and Dotson and Crosson and samples the entire time series to capture seasonal and interannual changes in the surface reflectivity potentially induced by melting, snow metamorphism, and changes in the microwave sensor. The training dataset was augmented by rotating each image and ground truth mask to produce over one thousand training images.

Network Application

We train the network using these refined binary classification images of crevasses. We implement the U-net segmentation algorithm using the python package Tensorflow (Abadi et al., 2015) with training data from Thwaites, Pine Island, Haynes, Pope, and Kohler Glaciers. The size of raw Sentinel 1A images ($\sim$ 17000 $\times$ 25000 pixels; $>$ 500 MB) is too great to segment at the native image resolution. We, therefore, divide each image into 500 $\times$ 500 pixel patches and run the U-net algorithm on each patch individually using a sliding window with an offset equal to the output layer image (460 pixels in both dimensions). We tested a variety of optimizers and found the Adams optimizer maximized the area under the receiver operating curve that we used as the evaluation metric for model selection. The output of the U-net model is a 460 $\times$ 460 pixel image of the likelihood (ranging from 0 to 1) that a pixel contains part of a fracture. We then used the F_1 score to choose a threshold for binary classification (model prediction probability greater than 0.8 maximized the F_1 score).

We apply the trained network on more than three hundred Sentinel SAR 1A images from five separate scenes (Fig. 6.1a) that were selected for their comprehensive spatial and temporal coverage of lower Thwaites Glacier, Pine Island Glacier, and Haynes, Smith, Pope,

and Kohler Glaciers that feed the Dotson and Crosson Ice Shelves. Each scene is divided into 500×500 pixel patches using the same division scheme implemented for the training data. These images were then combined by merging the images, using the maximum value of the pixels within the shared windows. Because translational equivariance is not preserved in CNNs, clipping schemes are necessary to accurately stitch patches of the segmented image back together. We evaluate a variety of padding schemes and find that padding each segmented layer by 20 pixels reduces the error most in the final image relative to hand-drawn masks.

Validating the network and image filtering

The network was applied to the complete time series and used to calculate the area of crevassed ice using a 3-month rolling median filter with a threshold of 10 km^2 (Fig. 6.3b). We also use high-resolution optical imagery, WorldView with ∼0.5 m image resolution, and ultra-high-frequency ice-penetrating radar, which captures crevasses below the penetration depth of Sentinel imagery, to validate the extent and shape of these features.

6.2.2 Method evaluation with Optical and Ice-Penetrating Radar Imagery

The crevasses we identify in SAR backscatter images are fundamentally near-surface features. They reflect the fracture properties of snow and firn, which may or may not be connected to crevasses and voids that extend deeper into the ice column. To understand the dependencies of the segmentation algorithm on the satellite orbit geometry, we use both ascending and descending orbits from interior Thwaites and Pine Island Glaciers, and show that our approach of using both orbital geometries helps eliminate ambiguities in crevasse detection present with a single geometry. To better determine the connection of the features we image to the surface and subsurface geometry, we evaluate the algorithm and the methods used to identify crevasses with manual inspection of alternative higher-resolution optical images (Worldview), which depict the appearance of crevasses at the surface, and ice-penetrating radar data (Operation IceBridge and International Thwaites Glacier Collaboration aerogeophysical surveys, Fig. 6.6), which images crevasses in the subsurface.

Comparison of crevasse detections from the SAR data with high-resolution optical imagery and ice-penetrating radar data confirms that the detected features are always crevasses, but also that crevasses detected with SAR data are commonly buried with no surface expression.

Crevasse Orientation and Scene Geometry

In agreement with the findings of Marsh et al. (2021), the character and expression of the crevasses we image change in Sentinel imagery as a function of satellite look angle, the slope of the surface, and crevasse orientation (Fig. 6.5). In descending scenes over Thwaites and Pine Island Glaciers, the left column in Figure 6.5, crevasses that fracture along the true east-west axis appear as highly reflective scatterers; while in the ascending scenes, (the middle column of Figure 6.5), crevasses that are oriented in the grid east-west direction return the most energy. Our results indicate that SAR detection of crevasses is highly dependent on look angle. We recommend using all available scene geometries when conducting SAR analysis for scientific or logistical assessment.

Crevasse Appearance in Optical Imagery

SAR imagery presents a view of the surface and subsurface, and determining whether a crevasse detection is indicative of a surface or subsurface feature is difficult from SAR imagery alone. WorldView high-resolution optical imagery does not penetrate into the subsurface and thus presents an unambiguous image of the surface crevasse geometry. Near crevasse onsets, WorldView imagery often directly images clear crevasses or surface features indicative of crevassing (Fig. 6.6b), such as regular "swells" likely representing snow bridges, that are associated with crevasses that are also imaged SAR imagery and ice-penetrating radar data (see Section 6.2.2). In some areas downstream of crevasse onsets, there is extensive crevassing indicated in SAR imagery, but there is also no surface expression of the crevasses in the WorldView image (Fig. 6.6c). This suggests that these crevasses are subsurface features – crevasses that have been buried by accumulation following formation. Examination of spatially-coincident ice-penetrating radar profiles confirms that these are subsurface crevasses that have been buried (Fig. 6.6e, see Section 6.2.2). This indicates

that SAR images subsurface crevasses reliably, including occasional near surface crevasses ($<$ 10 m depth) that present hazard and are not imaged in high-resolution optical imagery, but does not comprehensively map the subsurface geometry, which is better imaged by ice-penetrating radar.

Crevasse Appearance in Ice-Penetrating Radar

The geometry of crevasses with depth can be interpreted most easily in ultra-high-frequency wideband ice-penetrating radar profiles. However, interpretations of crevasse morphology are still complicated by the dependence of the return on the orientation of the radar profile relative to the geometry of the crevasse and generally complex shape of the crevasse itself. For simplicity in this discussion, we assume that the radar profiles are oriented orthogonally to the crevasse (Fig. 6.6). The radar profiles we interpret in this study are interpreted following this geometric constraint. In this geometry, there are three primary components of the crevasse geometry that are recorded in the radar data: (1) reflections form the crevasse top and sidewalls, (2) diffraction from wave spreading and interference at the crevasse sidewalls, and (3) refraction of the radar wave into the crevasse void where no energy is reflected back to the receiver. These are manifested in a radargram as (1) a strong reflection that interrupts otherwise smooth snow/firn stratigraphy, (2) strong hyperbolic diffractors along the sidewalls, and (3) a vertical column (or wedge) with consistently low amplitude returns below the peak of diffraction hyperbola. Examples of radargrams that fit this characteristic description are shown and labeled in Figures 6.6.

Our radar data add context to the crevasses we identify in satellite SAR imagery in several ways. First, crevasses have a finite depth. Although there is a drop in reflected energy beneath crevasse voids, when layers are present, there are always continuous layers below the void. The diffraction hyperbola from sidewalls are also only present for a fixed depth range. This indicates that crevasses occupy a finite depth span (typically no greater than $\sim$ 50 m from top to bottom) on grounded ice. Second, with a few exceptions, crevasse tops occur in the near subsurface (depth of $<$ 150 m). Crevasses initially are imaged with voids that are at or very near the surface in areas of crevasse onsets. Subsequent burial is common and

crevasses downstream of onset zones may have characteristic hyperbola peaks well below the surface (to depths of > 100 m). We do not image crevasses deeper than ~ 200 m except when basal rifts on ice shelves are also present. Many of these deepest reflectors may be side-lobe reflections that do not represent true crevasse locations. Third, the geometry and material composition of the crevasses change between formation and subsequent burial. Crevasses that are newly formed are characterized mainly as a vertical column of low amplitude returns, indicating a purely vertical feature. As the crevasses widen in the SAR imagery, characteristic diffraction hyperbola develop, likely indicating prominent sidewalls that narrow with depth, i.e., formation of an inverted wedge geometry, which has been confirmed with direct exploration of crevasses. Fourth, areas with crevasses that overlap in patterns inconsistent with current crevasse formation due to the observed strain rates are often associated with crevasse families that are imaged at different depths in the ice-penetrating radar data (Fig. 6.6e), which likely indicates upstream formation and subsequent burial and closure during advection downflow. Finally, in some cases, crevasses that form at the surface are buried and subsequently form a layer consisting of overlapping hyperbolas characteristic of buried and closed crevasses. This observation is qualitatively similar to interpretations of hyperbolic diffractors as buried crevasses indicative of past shear margins in other areas of the ice sheets.

These observations of three-dimensional structure revealed in the SAR and ice-penetrating radar imagery have ramifications for the interpretation of ice tensile strength and the influence of crevassing on ice-sheet structure discussed later in Sections 6.3.2 and 6.4.1. However, the agreement of crevasses identified in SAR imagery with crevasses visible in other sources gives high confidence that crevasses are surface and near surface (< 200 m depth) features that are robustly identified by the neural network. We next evaluate changes in crevasse area recorded in the SAR imagery time series and their implications for understanding the material properties and fracture mechanics of firn/ice.

6.3 Results

6.3.1 Crevasse Expansion in the Amundsen Sea Embayment

Results from the algorithm applied to the SAR image timeseries are summarized in Figures 6.2 and 6.3. We identify three types of phenomenological changes in crevasse area and density that describe the increase in damaged surface area in the Amundsen Sea Embayment:

- Inland migration of crevassing associated with the initiation of crevasse nucleation zones in regions of previously uncrevassed areas of potentially damaged ice that is surrounded by previous crevasses.

- Large areas of rapid crevasse expansion (faster than the 12-day sampling rate of Sentinel scenes) in previously uncrevassed ice.

- Crevasse appearance where preexisting fractures have been advected from upstream. These changes in the density of damaged ice are discernible in the changes in the patterns of crevasse orientations.

The broad-scale crevassing patterns differ between the major glacier systems we examine in this study and are correlated with changes in effective stress expressed in the glacier surface velocities (Fig. 6.3). From 2017–2022, Pine Island Glacier sped up, accelerating by ∼500 m/yr near the grounding line over the course of five years. On Pine Island Glacier, there is a large increase in crevassed area in 2017 when the glacier also sped up in response to changes in the buttressing capacity of the ice shelf (Fig. 6.3b; Joughin et al., 2021). The crevassed area then increases more slowly and steadily from 2018 to 2020. This is followed by a second more rapid increase in crevassed area from 2020–2021, which is contemporaneous with a major calving event, similar to the 2017 increase in crevassing. Thwaites Glacier also accelerated, speeding up by 400 m/yr near the grounding zone between 2017–2022 (Benn et al., 2022). This speedup, which is contemporaneous with the increase in crevassing on Thwaites from 2020–2021, has been attributed to the development of full-depth fractures near a prominent pinning point on the Thwaites Eastern Ice Shelf (Benn et al., 2022). During this time period,

the crevassed area of Thwaites Glacier increased by 10% and expanded inland of the glacier grounding line while also increasing in crevassed area density in previously crevassed regions. The glaciers that feed Dotson and Crosson Ice Shelves do not systematically speed up during this time period and crevasse areas here are steady.

Our results indicate that crevasse area change in the Amundsen Sea are correlated with regional changes in glacier velocity, which are connected to the mechanics of glacier sliding (Hoffman et al., 2020, 2022). The relationship between basal shear stress and glacier sliding velocity (also termed the sliding law) mediates the transmission of stress inland as basal shear stress increases. Glaciers in the ASE accelerate to balance changes in driving stress associated with distributed steepening due to ocean melt or changes in the buttressing of ice shelves near the terminus. The heterogeneous pattern of thinning we observe across Thwaites reveals the complexity of this relationship (Supplement Video 1, Hoffman et al., 2020)) and agrees with patterns we see in crevassing, which are concentrated on the stoss side of local elevation highs associated with large scale subglacial topography and basal resistance (Fig. 6.1) (Hoffman et al., 2022).

6.3.2 Evaluating fracture instability hypotheses with modern observations

By combining the crevasse time series with an ice-velocity timeseries from the same period, developed from the same satellite constellation, we can directly examine the relationship between crevasse formation and expansion and ice velocity. First, we briefly review a common relationship between crevasse formation and ice surface stress which can be determined from ice-velocity observations. We then use our observations to estimate the tensile strength of snow and firn.

Fracture nucleation and growth have been a major topic of research in glaciology for more than sixty years (Nye, 1959; Vaughan, 1993; Veen, 1999). Early analytic expressions remain in common use today and are frequently applied in both scientific and logistic analyses. These formulations often assume that crevasse formation relies on the surface stress exceeding a threshold, most often the tensile strength of ice. The most common of these formulations is the von Mises (octahedral) failure criterion. This criterion assumes that the material can

support an octahedral shear stress that is less than the tensile strength of ice (σ_t) and can be formulated as (Vaughan, 1993):

$$\sigma_e < \sigma_t \tag{6.1}$$

$$\sigma_e^2 = \sigma_{1surf}^2 + \sigma_{2surf}^2 - \sigma_{1surf}\sigma_{2surf} \tag{6.2}$$

where σ_e can be interpreted as the effective stress and σ_{1surf} and σ_{2surf} are the principal surface stresses parallel to the ice surface. Because the top boundary of an ice sheet or glacier is a free surface, normal stress and traction are zero at this boundary, and thus one of the three principal stresses must be normal to the surface and have a magnitude equal to zero (Vaughan, 1993; Veen, 1999). The other two principal stresses are parallel to the surface. Next, we combine our new crevasse location time series with satellite SAR observations of ice velocity from the same satellites (Sentinel 1A and 1B) to compare with the von Mises failure criterion.

Following previous work (Nye, 1959; Bindschadler et al., 1996; Veen, 1999; Alley et al., 2018), we first calculate the principal surface stresses from the ice-velocity time series (see Appendix D.2). We then extract the surface stresses at crevasse locations identified by the CNN quarterly between 2015 and 2022. This results in surface stress maps with an ovaloid failure surface, as expected for the von Mises failure criterion (Fig. 6.3a). Comparison of surface stress values between crevassed and uncrevassed ice suggests that the tensile strength of the near surface can be bounded (Fig. 6.4). For Thwaites Glacier (other glaciers in the ASE have similar results), this approach creates a failure envelope consistent with a tensile strength between 75 and 210 kPa. These estimates of the tensile strength of the ice sheet agree with limits cited elsewhere in the remote sensing literature, but disagree with failure limits determined from laboratory measurements conducted on pure ice.

6.4 Discussion

One of the major unresolved questions related to the constraints on the fracture properties of glacier ice is the apparent disagreement between fracture properties of ice derived from

laboratory experiments and estimates from in situ and remote sensing observations. Critical yield strength and fracture toughness, a measure of how existing fractures may propagate, often disagree between remote sensing and experimentally derived estimates, sometimes by orders of magnitude. For example, the tensile strength of ice measured in laboratory experiments conducted by McClung and Schaerer (2006) range from 0.7 to 3.1 MPa while the tensile strength inferred from satellite-derived surface strain rates has been observed to vary from 0.1 to 1 MPa (Vaughan, 1993; Scott et al., 2010; Ultee and Bassis, 2016). The values we observe (75 to 210 kPa) are in line with ranges derived from surface crevasse features imaged elsewhere in Antarctica and suggest that the crevasses and associated yield strengths determined from satellite observations of surface strain may reflect near-surface fracture in firn where the fracture toughness is reduced by firn porosity (Smith et al., 1990; Fischer et al., 1995; Rist et al., 1999, 2002).

Models that describe the effects of porosity on fracture toughness were first developed for metals, ceramics, polymer foams, and sponges (Ashby and Medalist, 1983; Maiti et al., 1984; Gibson and Ashby, 1999), and, though the fracture toughness of fresh water has been known to decrease with increasing porosity (Rist et al., 1999, 2002), this relationship remains disconnected from the physical theory of fracture propagation. Physical models that unify the behavior and observations of near-surface fracture with fracture propagation deeper in the ice column are important to represent the effects of damage on the viscosity of the ice sheet.

6.4.1 A simple geometric model for the fracture properties of firn

Our approach follows from Jelitto and Schneider (2018) and uses geometric arguments based on a simple conceptual model for firn pore space to derive a relationship between the fracture toughness of densifying snow from the fracture toughness of ice (K_{IC}) and the firn porosity (P). We introduce this model using the concept of toughness (G_C) and Young's modulus, E_C. The toughness of a material describes the crack extension force or the strain energy release rate with respect to the crack length. The Young's modulus describes the linear elastic deformation of the material under applied stress. These material parameters can be

converted to the normalized toughness (G_C^*/G_C) and normalized Young's modulus (E_c^*/E_c) by taking the ratio of the substantial crack surface to the total crack surface. Together, G_C^*/G_C and E_C^*/E_C can be used to calculate the normalized fracture toughness (K_{IC}^*/K_{IC}). Fracture toughness and the strain energy release rate define the state of a loaded crack system; they do not constitute a criterion for crack propagation. Instead, fracture toughness can be viewed as a measure of how close to unstable propagation a stressed crack is (i.e., when the stress intensity factor reaches a critical level for the material ($K_I \geq K_{IC}$) or when the strain energy release rate reaches a critical rate $G \geq G_C$, the crack will propagate). Porosity affects the fracture toughness by increasing the total crack surface which includes pores and void spaces in the lattice, promoting failure propagation along the crack face that bisects the volume through the nearest and largest pores.

Using expressions for the normalized toughness and normalized Young's modulus we derive a firn-specific fracture model for fracture toughness and compare this model with models developed by Smith et al. (1990) and Rist et al. (1999, 2002). We assume a closed idealized lattice of firn with ligament thickness (t) and unit cell width (w, Fig. 6.7). Within this lattice, we define the relative fraction of pore connections (X) to capture the structural impact of unsintered grains and the microphysical imperfections of firn observed with scanning electron microscopy. The firn structural analog of a unit cell for this geometric model is shown in Figure 6.7 with the associated crack face. If X is 0, the lattice is perfectly intact and the porosity can be calculated as a function of the ratio d=t/w based on the geometry of the lattice as:

$$P = \frac{(w-t)^3}{w^3} = (1-d)^3 \tag{6.3}$$

As X approaches 1, then the lattice behaves as though it is completely porous. The effect of connections between pores on the toughness can be introduced by assuming that X, the fraction of connections between pores, is a function of porosity. That is, as the walls that enclose pore space within the firn become thicker (d approaches 1, P approaches 0), the number of connections between pores decreases and the fracture toughness increases. Following Jelitto and Schneider (2018), we assume that the disconnections can be related to

porosity by $(1-X)=(1-P)^n$, and the toughness can be formulated from the geometry of the crack face as

$$\frac{G_C^*}{G_C} = \frac{w^2-(w-t)^2}{w^2} X = \left(1-(1-d)^2\right)(1-P^n) \tag{6.4}$$

Solving the quadratic equation for the ratio of the ligament thickness and unit cell width as a function of porosity and substituting the result into the expression for G_C^*/G_C we find that $d = 1-P^{1/3}$. And thus

$$\frac{G_C^*}{G_C} = \left(1-P^{2/3}\right)(1-P)^n \tag{6.5}$$

The Young's modulus can be calculated by applying the rule of mixture for a parallel and serial arrangement (Jelitto and Schneider, 2018)

$$\frac{E^*}{E} = \left(\frac{1-d}{2d-d^2} + \frac{1}{2-d+(1-d)^2\, d^{-1/2}}\right)^{-1} (1-P)^n \tag{6.6}$$

where again,

$$d = 1-P^{1/3}. \tag{6.7}$$

From these expressions, the normalized fracture toughness takes the form

$$\frac{K_{IC}^*}{K_{IC}} = \sqrt{\frac{G_C^* E^*}{G_C E}} \tag{6.8}$$

$$\frac{K_{IC}^*}{K_{IC}} = \sqrt{1-P^{2/3}} \left(\frac{1-d}{2d-d^2} + \frac{1}{2-d+(1-d)^2\, d^{-1/2}}\right)^{-1} (1-P)^n \tag{6.9}$$

This can be rewritten as a function of porosity as:

$$\frac{K_{IC}^*}{K_{IC}} = \frac{\sqrt{1-P^{2/3}}\,(1-P)^n}{\frac{P^{2/3}-1-(1-P)^{1/3}P}{P^{2/3}-1}\left(1+\left(-1+\sqrt{1-P^{1/3}}\right)^{2/3}\right)} \tag{6.10}$$

Figure 6.8 shows a comparison of fracture toughnesses from Rist et al. (1999) and Fischer et al. (1995), adapted from Smith et al. (1990), and the geometric model reformulated from Jelitto and Schneider (2018) for the firn structure with pore space described above. These

data show encouraging agreement and suggest that the near-surface fractures we observe in the Amundsen Sea may reflect the fracture properties of snow and firn, not ice. More data particularly the firn microstructural scans and fracture toughness and tensile strength data should be collected for firn that has experienced a range of strain and densification histories.

6.4.2 Implications of inland migration of near surface fracture

Our observations of inland crevasse migration on Thwaites and Pine Island Glaciers are consistent with porosity-dependent fracture models that would predict near-surface fracture preceding deeper crevasse propagation. The apparent migration of these features inland is not a sign of instability, but rather a symptom of enhanced horizontal strain. Though the extent of these features is expanding inland, evidence of relict crevasses filling with snow suggests that at least some of the near-surface crevasses we image on Thwaites Glacier may also heal. Observations of crevasse filling and healing have implications for Thwaites Glacier response, as these processes likely impact the mechanics of potential disintegration via hydrofracture. The crevasse position time series also presents a target for models that seek to simulate the effects of fracture on grounded-ice mechanics and glacier discharge for a catchment where the material strength of grounded ice in relation to calving has been hypothesized to lead to catastrophic collapse.

6.5 Conclusions

These are the first observations of changes in the fracture behavior of grounded snow, firn, and ice on Thwaites Glacier and its neighbors in the Amundsen Sea Embayment. Our results indicate that changes in crevasse area are generally correlated with increases in surface stresses (Fig. 6.3b,c) and thinning. Although our observations are generally consistent with observations of ice yield strength (∼100–200 kPa) determined from remote sensing, these failure limits are smaller than the failure limits predicted by laboratory experiments conducted on solid ice. We have shown that these inconsistencies can be resolved by accounting for the effects of porosity on fracture intensity; however, more observations of fracture behavior in firn are needed to verify this hypothesis. The presented time series of crevasse evolution also presents a verifiable target for models that incorporate fracture or continuum damage

mechanics, non-local effects associated with damage accumulation, damage anisotropy, and experiments aiming to simulate potential future material failure of the marine outlet glaciers that drain the West Antarctic Ice Sheet. Ongoing collection of Sentinel SAR images can also be processed quickly enough so that live crevasse detection in areas where researchers are conducting fieldwork is possible and are available from the authors upon request.

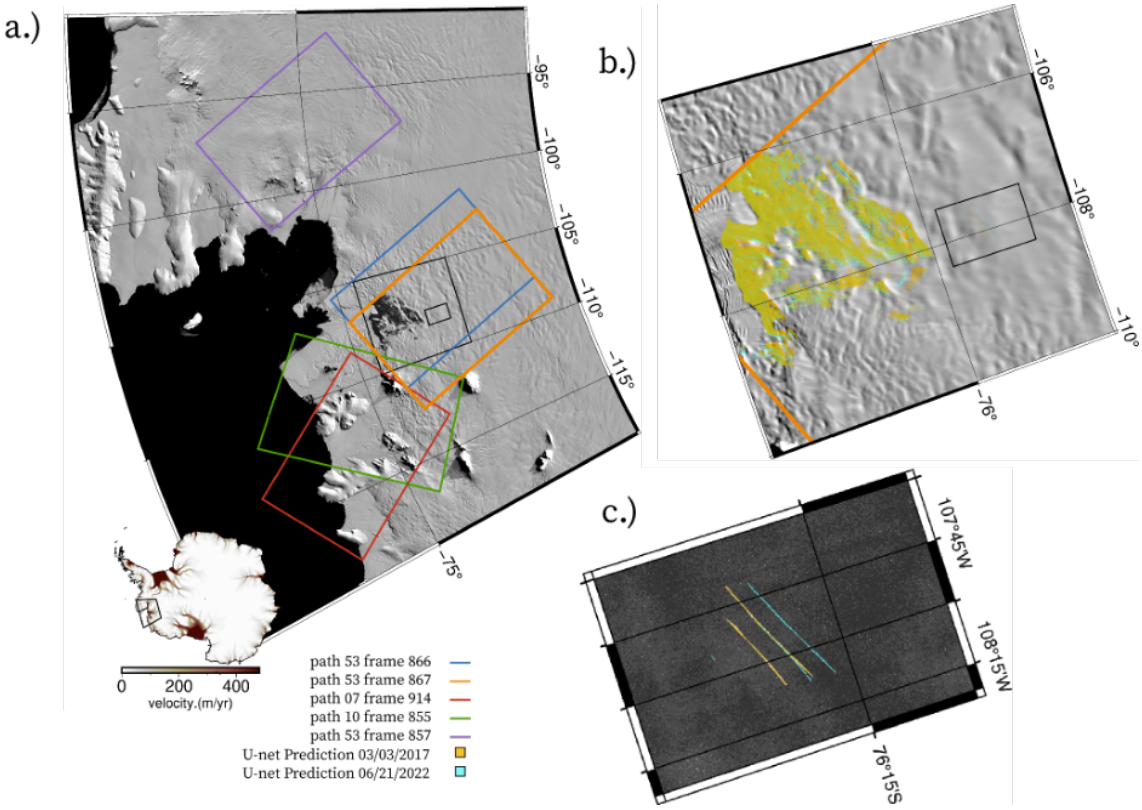

Figure 6.1: (a) Overview of Sentinel scenes of Amundsen Sea glaciers used to create inland crevasse area time series for the grounded regions of Pine Island (lavender), Thwaites (blue, orange), and glaciers feeding the Dotson and Crosson ice shelves (green and red). Black boxes mark areas of paneled images in (b) and (c). (b) An example of the map of crevasses predicted by the U-net from March of 2017 (cyan) and June 2022 (orange). Note that the density of crevasses appears to be concentrated on the stoss side of ridges that are captured in the background MODIS image (Haran et al., 2018). The U-net also skillfully detects (c) isolated crevasse features in low-strain environments

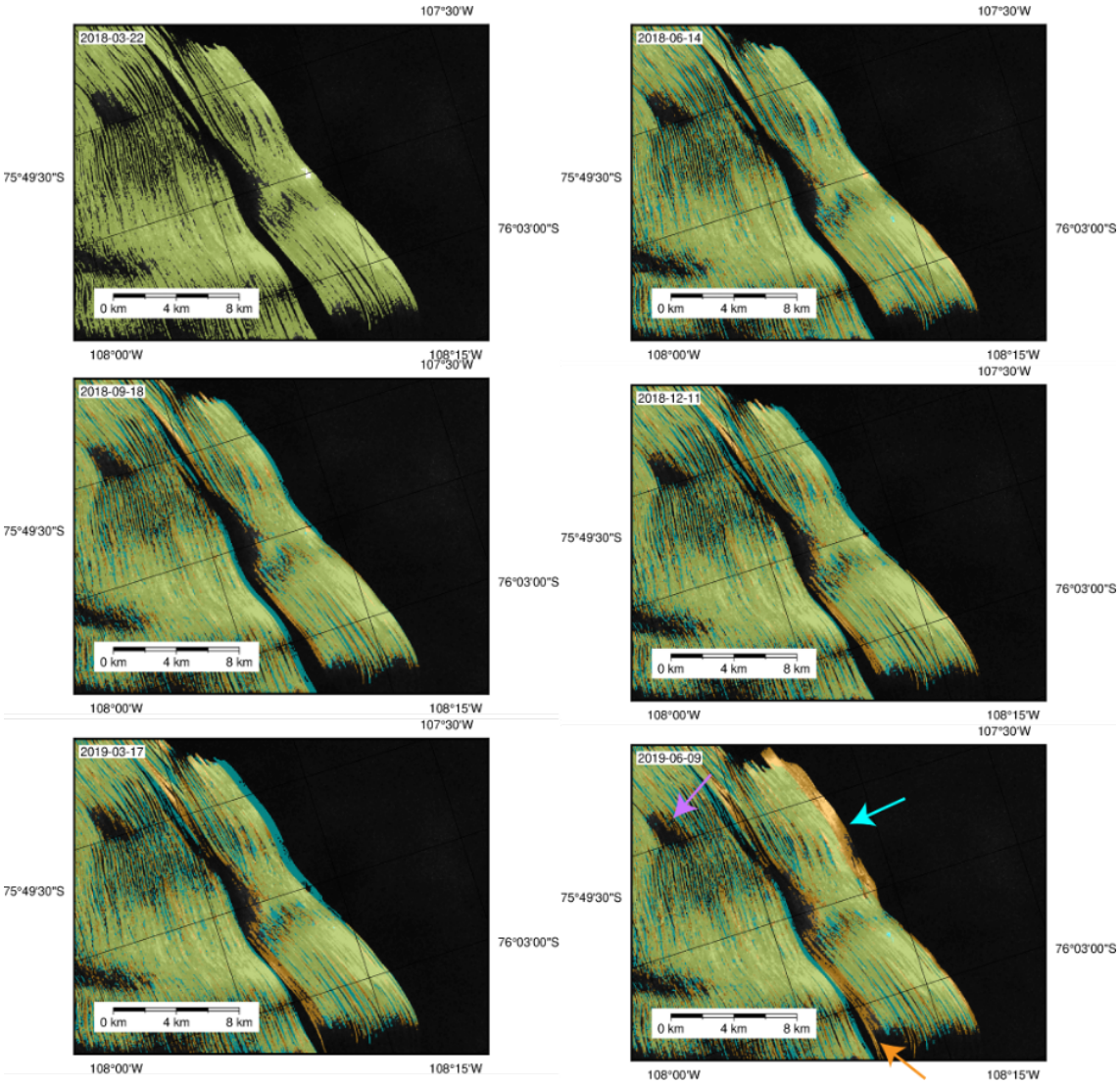

Figure 6.2: SAR time series of inland crevasse advection and nucleation between 2018-2019 in the upper reaches of the crevassed trunk of Thwaites Glacier. The U-net crevasse prediction of a scene shot in March 2018 (cyan) overlain with subsequent crevasse location prediction (orange). Arrows highlight different mechanisms of crevasse area change: orange, advection due to fill-in; blue, rapid expansion; and purple, crevassing in areas with preexisting fractures.

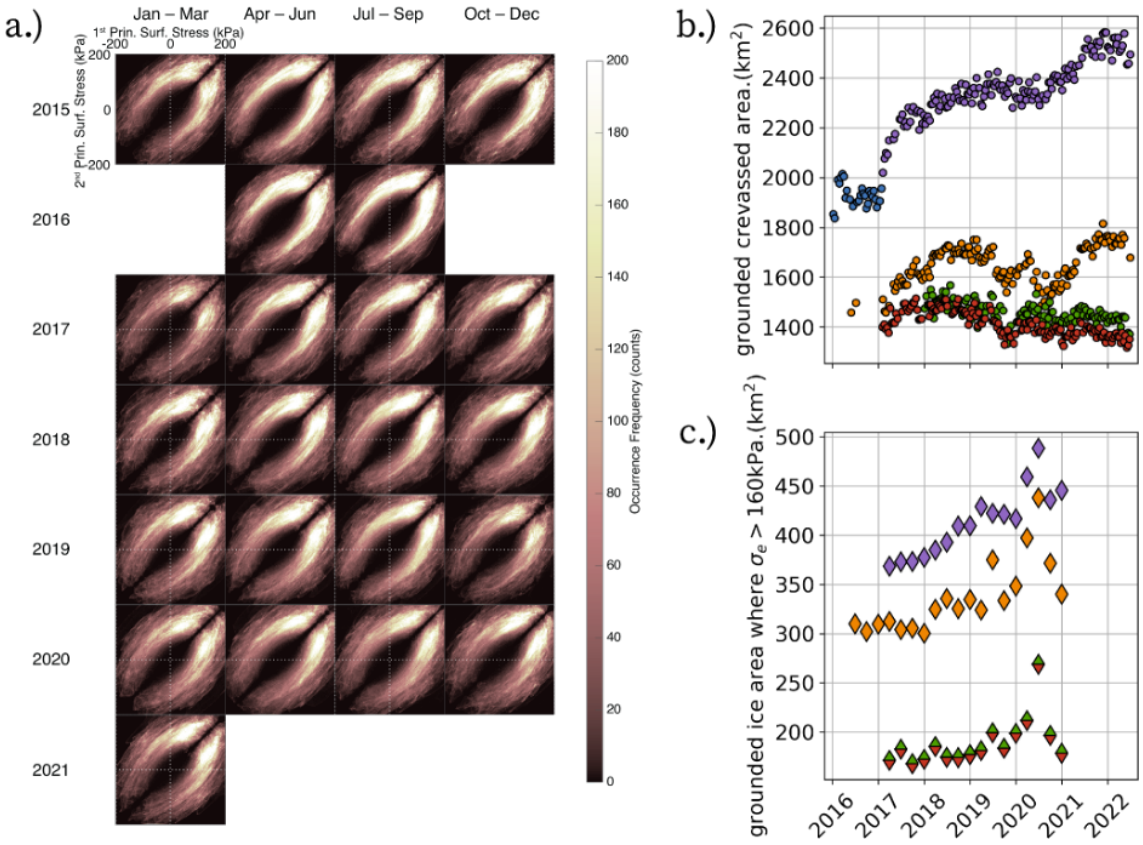

Figure 6.3: (a) Principal surface stress failure envelopes of Thwaites Glacier crevasse time series from 2015–2022, following Vaughan (1993). (b) Crevassed area for the grounded regions of Pine Island (lavender), Thwaites, (blue, orange), and the glaciers feeding Dotson and Crosson Ice Shelves (green and red), with (c) the area where the effective stress (calculated using the surface membrane stresses) exceeds 160kPa.

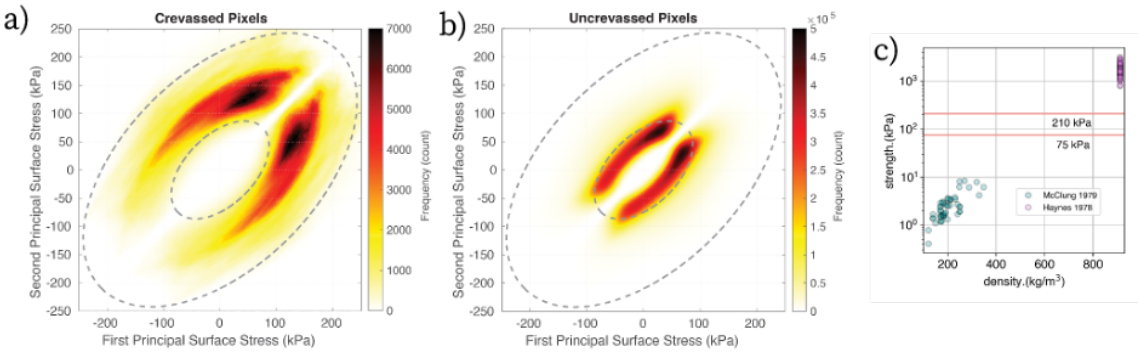

Figure 6.4: Principal surface stress failure envelopes observed on Thwaites Glacier are shown for (a) crevassed and (b) uncrevassed regions of the glacier identified with U-net. Also shown are the (C) experimental tensile strengths inferred from laboratory experiments conducted on snow and ice.

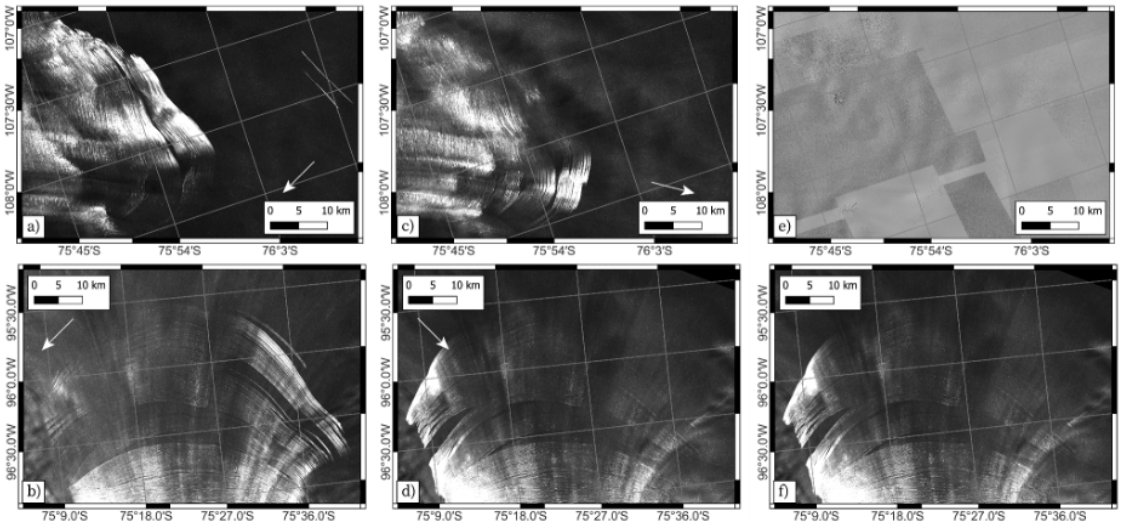

Figure 6.5: Crevasse appearance in ascending (a, b) and descending (c,d,f) orbits of Sentinel-1 satellite imagery for interior regions of Thwaites and Pine Island Glaciers. Arrows indicate satellite look direction. Also shown is a WorldView image (e) for the same coverage of Thwaites Glacier, revealing how many of the crevasses that are readily visible in Sentinel imagery are buried beneath snow bridges that obscure the features in panchromatic optical imagery.

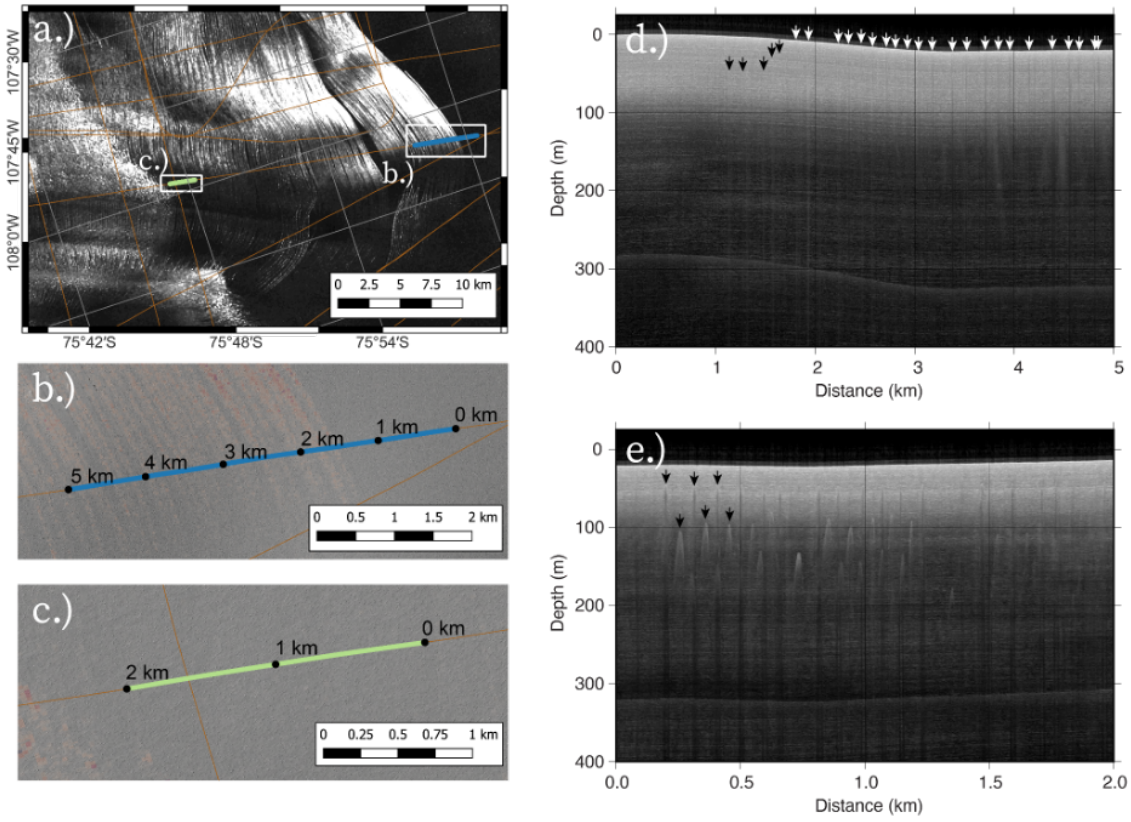

Figure 6.6: (a) SAR backscatter intensity image with flight lines of ice-penetrating radar that cross the (b) onset of surface crevassing in panchromatic optical imagery and (c) buried crevasses downstream in panchromatic optical imagery. (d, e) Layers in radar profiles observed beneath surface features imaged in SAR backscatter and high-resolution panchromatic optical imagery.

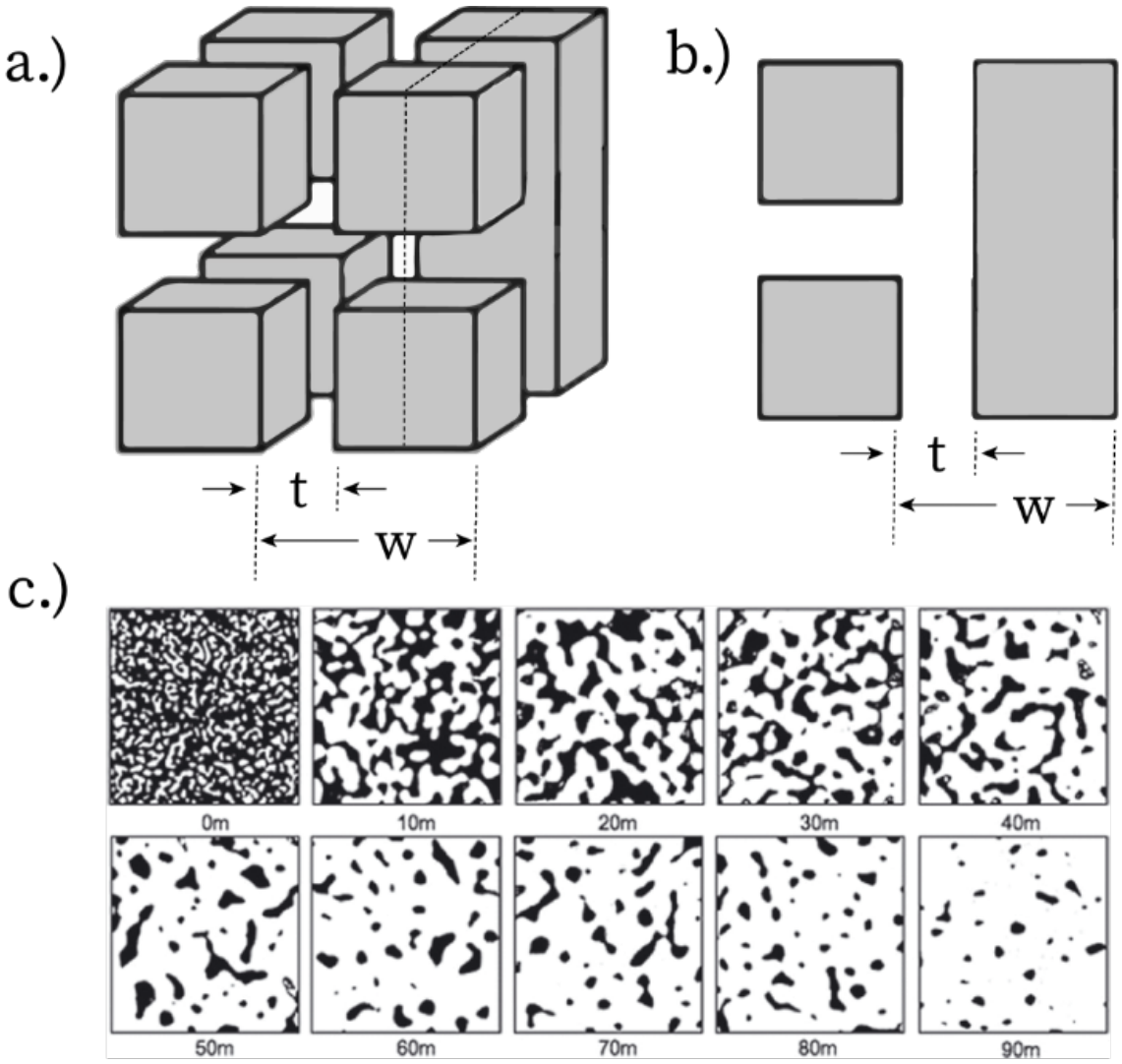

Figure 6.7: Conceptual geometric model for firn fracture with diagrams of (a) the unit cell, and the (b) crack face used to derive the relationship between fracture toughness and porosity. Also shown is (c) a micro CT scan of firn structure revealing the effect of compressed pore space within the firn. The scan was first presented by Lomonaco et al. (2011) using firn cores collected from Summit, Greenland.

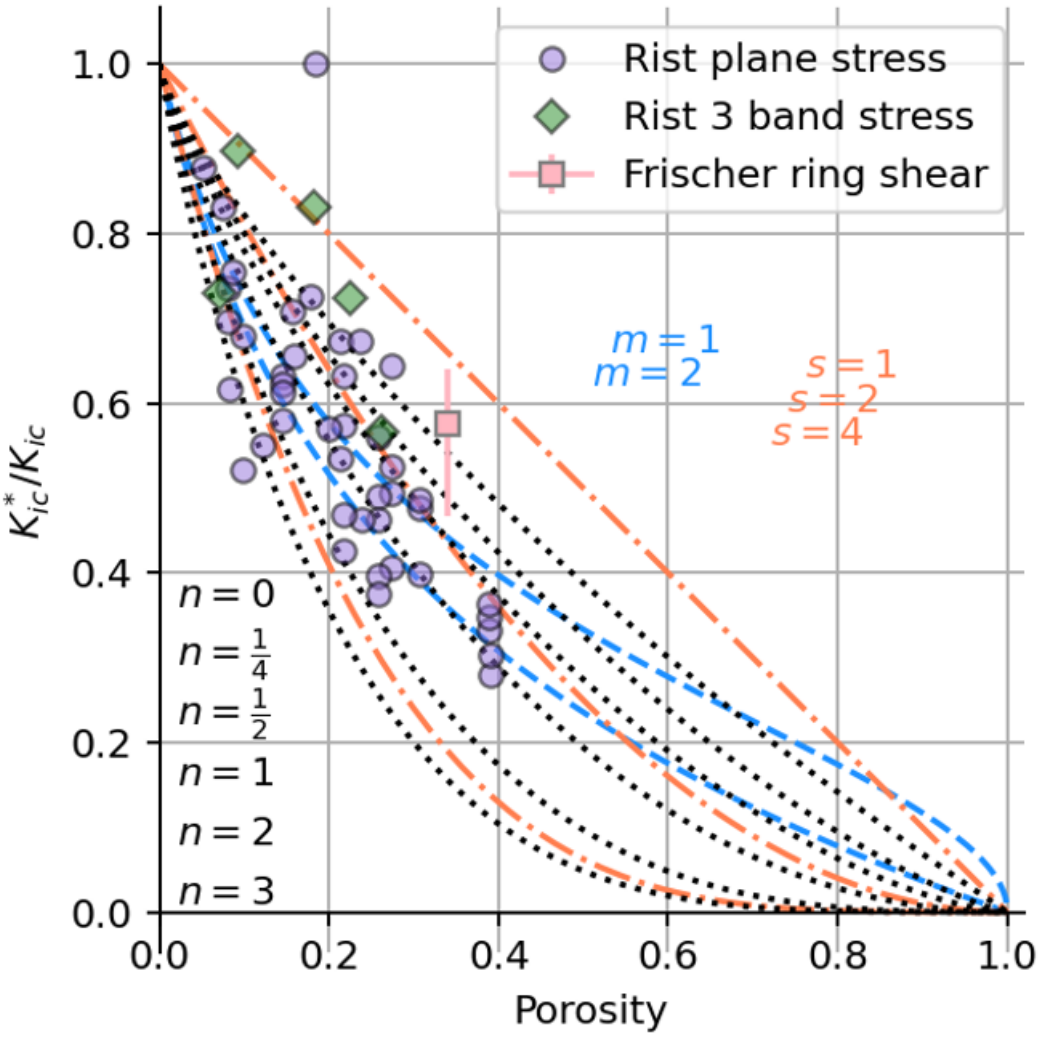

Figure 6.8: Fracture toughness vs. porosity for three different models (black, blue and orange), are presented with available data from the Filchner-Ronne Ice Shelf (Rist et al., 1999, 2002) and Summit Greenland (Fischer et al., 1995) normalized by the fracture toughness of ice.

Chapter 7

CONCLUSION

We have presented results across Antarctica that use novel datasets and models of varying complexity to understand the mechanics of subglacial lake activity, ice deformation, the history of flow in West Antarctica, and the mechanics of fracture that may impact the ice sheet's future. We have shown that newly discovered subglacial lakes on Thwaites Glacier have remained active over the last ten years and will likely continue to fill and drain as Thwaites accelerates and retreats into the overdeepened interior of the Amundsen Sea Embayment. These lakes currently do not play a significant role in changing the discharge of ice mass from the interior to the outlet glacier margin, and they appear to occupy areas of known low basal resistance. The mechanics of these active subglacial reservoirs of water afford an opportunity to understand the mechanics of grounding and ungrounding in an environment where, as yet, there are no known surface hazards. The possibility of using these environments as a proxy for the glacier grounding zone is an active research opportunity we are exploring as part of the International Thwaites Glacier Collaboration. This collaboration is also using multi-element radar arrays to swath map more of the basal topography on Thwaites Glacier and potentially image structure and detail that has changed since the 2010 survey presented in Chapter 3. These data will build on the work presented in this dissertation that has connected the roughness of the subglacial landscape to shear stress at the ice–bed interface and inform future work that aims to understand how subglacial landforms form.

In Chapter 4, we presented swath data sets from the interior of the continent at the prospective location of an ice core, Hercules Dome. Our data reveal large kilometer-scale features in the subglacial landscapes typical of a marine proximal alpine glaciated environment. Lineations within the glacial valleys we imaged in our survey suggest that ice at Hercules Dome has flowed much more rapidly than the ice presently does today. The in-

ference of more rapid flow sometime in the ice sheet's past carries implications for ice-sheet nucleation and the details of ice-sheet growth following deglaciation. These data also suggest that ice at Hercules Dome likely responds more readily to climate perturbations than observations of modern flow initialized with present surface velocities and surface elevation, with implications for the rates of drawdown and ice elevation signals preserved in a prospective ice core. These interior observations motivated work closer to the margin at Conway Ice Ridge (previously known as Ice Ridge A). This ridge sits between the Mercer and van der Veen Ice Streams and encodes information about the configuration and response of these ice streams to the climate transition out of the Last Glacial Maximum because of its comparatively slow response time relative to the neighboring ice streams. From the radar survey conducted at Conway Ridge presented in Chapter 5, we hypothesize that the ridge has slowed down in the last 3,000 years when buried crevasses that would have formed at the surface experienced sufficient strain to open. We are actively working with parametric models of ice-stream shear margins to understand the sensitivity of surface changes we observe at present (modern acceleration and thickening) and past changes suggested by layering and buried crevasses in ice-penetrating radar profiles to understand the mechanics of the Mercer and van der Veen Ice Streams following the Last Glacial Maximum.

We conclude by returning to the Amundsen Sea where surface crevasses visible in the backscatter of active satellite synthetic aperture radar imagery reveal changes in the area of damaged ice on Thwaites and Pine Island Glaciers. Using velocity time series available from the same time period (generated using the same imagery), we relate the change in fractured areas of lower Thwaites and Pine Island Glaciers to the tensile stress of the surface changing as these glaciers accelerate and retreat. As part of this work, we also adapt a geometric relation that describes the effects of firn porosity on fracture toughness. This new model bridges discrepant behavior between satellite observations of surface crevasse features and laboratory load tests conducted on pure ice, and suggests that surface crevasses reflect physical properties that vary dramatically with depth in the near-surface. Surface crevasse area change and the the time series of crevasse density change presented in Chapter 6 present the first verifiable target for models that seek to resolve the fracture of ice and the impact of fracture on grounded ice discharge and Thwaites Glacier stability.

The manuscript published as Chapter 2 would not have been possible without the support of Benjamin Smith, Ian Joughin, and Daniel Shapero, who contributed datasets and modeling expertise that helped contextualize the GNSS time series, created from stations deployed between 2007 and 2010 by Knut Christianson when he was a graduate student at the Pennsylvania State University. The ideas presented in Chapter 3 were drafted during the pandemic thanks to Elizabeth Case, Jonny Kingslake, Nicholas Holschuh, Knut Christianson and Robert Arthern. These ideas eventually led to a prolonged visit at the British Antarctic Survey hosted by Andy Smith, Alex Brisbourne, and Pierre Deutriux. The research environment at the British Antarctic Survey was incredibly inspiring and helped re-energize and focus much of the discussion that is presented in the final three chapters of the manuscript. Howard (Twit) Conway, the namesake of Conway Ridge, made this transition to and from the Cambridge more comfortable, and contributed incredible insight into the history of changes that have been detected or suggested in the Ross Sector that we present in Chapter 5. The work presented in Chapter 6 arose as part of field preparations for the 2022–2023 field season, wherein 19 people eventually made it to WAIS Divide and worked incredibly hard to make the most of a field season that was affected by the spread of COVID-19 across the Antarctic stations. The people involved in this work, and folks doing adjacent science in West Antarctica on Thwaites Glacier as part of the TIME, GHOST, and TARSAN teams, made the most of incredibly difficult circumstances that could have been filled with despair. I feel grateful to work with so many kind and generous people.

BIBLIOGRAPHY

Abadi, M., Agarwal, A., Barham, P., Brevdo, E., Chen, Z., Citro, C., Corrado, G. S., Davis, A., Dean, J., Devin, M., Ghemawat, S., Goodfellow, I., Harp, A., Irving, G., Isard, M., Jozefowicz, R., Jia, Y., Kaiser, L., Kudlur, M., Levenberg, N., Mané, D., Schuster, M., Monga, R., Moore, S., Murray, D., Olah, C., Shlens, J., Steiner, B., Sutskever, I., Talwar, K., Tucker, P., Vanhoucke, V., Vasudevan, V., Viégas, F., Vinyals, O., Warden, P., Wattenberg, M., Wicke, M., Yu, Y., and Zheng, X. (2015). TensorFlow: Large-scale machine learning on heterogeneous systems.

Ackert, R. P., Mukhopadhyay, S., Parizek, B. R., and Borns, H. W. (2007). Ice elevation near the West Antarctic Ice Sheet divide during the Last Glaciation. *Geophysical Research Letters*, 34:L21506.

Ackert, R. P., Mukhopadhyay, S., Pollard, D., DeConto, R. M., Putnam, A. E., and Borns, H. W. (2011). West Antarctic Ice Sheet elevations in the Ohio Range: Geologic constraints and ice sheet modeling prior to the last highstand. *Earth and Planetary Science Letters*, 307(1-2):83–93.

Akeret, J., Chang, C., Lucchi, A., and Refregier, A. (2017). Radio frequency interference mitigation using deep convolutional neural networks. *Astronomy and Computing*, 18:35–39.

Al-Ibadi, M., Sprick, J., Athinarapu, S., Stumpf, T., Paden, J., Leuschen, C., Rodríguez, F., Xu, M., Crandall, D., Fox, G., Burgess, D., Sharp, M., Copland, L., and Wychen, W. V. (2017). DEM Extraction of the Basal Topography of the Canadian Archipelago Ice Caps Via 2D Automated Layer-Tracker. *2017 IEEE International Geoscience and Remote Sensing Symposium (IGARSS)*, pages 965–968.

Alley, K. E., Scambos, T. A., Anderson, R. S., Rajaram, H., Pope, A., and Haran, T. M.

(2018). Continent-wide estimates of Antarctic strain rates from Landsat 8-derived velocity grids. *Journal of Glaciology*, 64(244):321–332.

Ambach, W. and Eisner, H. (1986). Proposal for a constitutive equation of temperate firn. *Cold Regions Science and Technology*, 13(1):1–9.

Ambach, W., Huber, J., Eisner, H., and Schneider, H. (1993). A constitutive equation for temperate firn derived from strain rates of two firn pits (Kesselwandferner, Oetztal Alps, 1967–1989). *Cold Regions Science and Technology*, 21(3):295–303.

Ambach, W., Huber, J., Eisner, H., and Schneider, H. (1995). Depth profiles of effective viscosities of temperate firn following from strain rate measurements at two firn pits (kesselwandferner, oetztal alps, 1967–1989). *Cold Regions Science and Technology*, 23(3):257–264.

Anandakrishnan, S. and Alley, R. B. (1997). Stagnation of Ice Stream C, West Antarctica by water piracy. *Geophysical Research Letters*, 24(3):265–268.

Anandakrishnan, S., Blankenship, D. D., Alley, R. B., and Stoffa, P. L. (1998). Influence of subglacial geology on the position of a West Antarctic ice stream from seismic observations. *Nature*, 394(6688):62–65.

Arthern, R. J. and Gudmundsson, G. H. (2010). Initialization of ice-sheet forecasts viewed as an inverse Robin problem. *Journal of Glaciology*, 56(197):527–533.

Arthern, R. J., Vaughan, D. G., Rankin, A. M., Mulvaney, R., and Thomas, E. R. (2010). In situ measurements of Antarctic snow compaction compared with predictions of models. *Journal of Geophysical Research: Earth Surface*, 115:F03011.

ASF DAAC (2014-2022). Alaska Satellilte Facility Distributed Active Archive Center, contains modified Copernicus Sentinel data 2014–2022.

Ashby, M. F. and Medalist, R. M. (1983). The mechanical properties of cellular solids. *Metallurgical Transactions A*, 14:1755–1769.

Barchyn, T. E., Dowling, T. P. F., Stokes, C. R., and Hugenholtz, C. H. (2016). Subglacial bed form morphology controlled by ice speed and sediment thickness. *Geophysical Research Letters*, 43(14):7572–7580.

Beem, L. H., Tulaczyk, S. M., King, M. A., Bougamont, M., Fricker, H. A., and Christoffersen, P. (2014). Variable deceleration of Whillans Ice Stream, West Antarctica. *Journal of Geophysical Research: Earth Surface*, 119(2):212–224.

Bell, R. E., Blankenship, D. D., Finn, C. A., Morse, D. L., Scambos, T. A., Brozena, J. M., and Hodge, S. M. (1998). Influence of subglacial geology on the onset of a West Antarctic ice stream from aerogeophysical observations. *Nature*, 394(6688):58–62.

Benn, D., Gulley, J., Luckman, A., Adamek, A., and Glowacki, P. S. (2009). Englacial drainage systems formed by hydrologically driven crevasse propagation. *Journal of Glaciology*, 55(191):513–523.

Benn, D. I., Luckman, A., Åström, J. A., Crawford, A. J., Cornford, S. L., Bevan, S. L., Zwinger, T., Gladstone, R., Alley, K., Pettit, E., and Bassis, J. (2022). Rapid fragmentation of Thwaites Eastern Ice Shelf. *The Cryosphere*, 16(6):2545–2564.

Bentley, C. R., Crary, A. P., Ostenso, N. A., and Thiel, E. C. (1960). Structure of West Antarctica. *Science*, 131(3394):131–136.

Berg, B. and Bassis, J. (2022). Crevasse advection increases glacier calving. *Journal of Glaciology*, 68(271):977–986.

Bindschadler, R. (1993). Siple Coast Project research of Crary Ice Rise and the mouths of Ice Streams B and C, West Antarctica: review and new perspectives. *Journal of Glaciology*, 39(133):538–552.

Bindschadler, R., Vornberger, P., Blankenship, D., Scambos, T., and Jacobel, R. (1996). Surface velocity and mass balance of Ice Streams D and E, West Antarctica. *Journal of Glaciology*, 42(142):461–475.

Bindschadler, R. A., Roberts, E. P., and Iken, A. (1990). Age of Crary Ice Rise, Antarctica, Determined from Temperature-Depth Profiles. *Annals of Glaciology*, 14:13–16.

Bingham, R. G., Ferraccioli, F., King, E. C., Larter, R. D., Pritchard, H. D., Smith, A. M., and Vaughan, D. G. (2012). Inland thinning of West Antarctic Ice Sheet steered along subglacial rifts. *Nature*, 487(7408):468–471.

Bingham, R. G. and Siegert, M. J. (2007). Radar-derived bed roughness characterization of Institute and Möller ice streams, West Antarctica, and comparison with Siple Coast ice streams. *Geophysical Research Letters*, 34:L21504.

Bo, S., Siegert, M. J., Mudd, S. M., Sugden, D., Fujita, S., Xiangbin, C., Yunyun, J., Xueyuan, T., and Yuansheng, L. (2009). The Gamburtsev mountains and the origin and early evolution of the Antarctic Ice Sheet. *Nature*, 459(7247):690–693.

Bogorodsky, V. V., Bentley, C. R., and Gudmandsen, P. E. (1985). *Radioglaciology*. Springer Dordrecht, Dordrecht, Holland.

Bons, P. D., Jansen, D., Mundel, F., Bauer, C. C., Binder, T., Eisen, O., Jessell, M. W., Llorens, M.-G., Steinbach, F., Steinhage, D., and Weikusat, I. (2016). Converging flow and anisotropy cause large-scale folding in Greenland's ice sheet. *Nature Communications*, 7:11427.

Booth, A. M., Roering, J. J., and Perron, J. T. (2009). Automated landslide mapping using spectral analysis and high-resolution topographic data: Puget Sound lowlands, Washington, and Portland Hills, Oregon. *Geomorphology*, 109(3-4):132–147.

Bougamont, M., Christoffersen, P., Price, S. F., Fricker, H. A., Tulaczyk, S., and Carter, S. P. (2015). Reactivation of Kamb Ice Stream tributaries triggers century-scale reorganization of Siple Coast ice flow in West Antarctica. *Geophysical Research Letters*, 42(20):8471–8480.

Bougamont, M., Tulaczyk, S., and Joughin, I. (2003). Numerical investigations of the slowdown of Whillans Ice Stream, West Antarctica: is it shutting down like Ice Stream C? *Annals of Glaciology*, 37:239–246.

Brondex, J., Gillet-Chaulet, F., and Gagliardini, O. (2019). Sensitivity of centennial mass loss projections of the Amundsen basin to the friction law. *The Cryosphere*, 13(1):177–195.

Bueler, E. and Brown, J. (2009). Shallow shelf approximation as a "sliding law" in a thermomechanically coupled ice sheet model. *Journal of Geophysical Research: Earth Surface*, 114:F03008.

Carter, S. P., Blankenship, D. D., Peters, M. E., Young, D. A., Holt, J. W., and Morse, D. L. (2007). Radar-based subglacial lake classification in Antarctica. *Geochemistry, Geophysics, Geosystems*, 8(3):Q03016.

Catania, G., Conway, H., Raymond, C., and Scambos, T. (2005). Surface morphology and internal layer stratigraphy in the downstream end of Kamb Ice Stream, West Antarctica. *Journal of Glaciology*, 51(174):423–431.

Catania, G., Hulbe, C., and Conway, H. (2010). Grounding-line basal melt rates determined using radar-derived internal stratigraphy. *Journal of Glaciology*, 56(197):545–554.

Catania, G., Hulbe, C., Conway, H., Scambos, T., and Raymond, C. (2012). Variability in the mass flux of the Ross ice streams, West Antarctica, over the last millennium. *Journal of Glaciology*, 58(210):741–752.

Catania, G. A., Conway, H., Raymond, C. F., and Scambos, T. A. (2006a). Evidence for floatation or near floatation in the mouth of Kamb Ice Stream, West Antarctica, prior to stagnation. *Journal of Geophysical Research: Earth Surface (2003–2012)*, 111:F01005.

Catania, G. A., Conway, H. B., Gades, A. M., Raymond, C. F., and Engelhardt, H. (2003). Bed reflectivity beneath inactive ice streams in West Antarctica. *Annals of Glaciology*, 36:287–291.

Catania, G. A., Scambos, T. A., Conway, H., and Raymond, C. F. (2006b). Sequential stagnation of Kamb Ice Stream, West Antarctica. *Geophysical Research Letters*, 33:L14502.

Chen, G. (1998). *GPS kinematics positioning for airborne laser altimetry at Long Valley*. PhD thesis, Massachusetts Institute of Technology.

Christian, J. E., Robel, A. A., Proistosescu, C., Roe, G., Koutnik, M., and Christianson, K. (2020). The contrasting response of outlet glaciers to interior and ocean forcing. *The Cryosphere*, 14(7):2515–2535.

Christianson, K., Bushuk, M., Dutrieux, P., Parizek, B. R., Joughin, I. R., Alley, R. B., Shean, D. E., Abrahamsen, E. P., Anandakrishnan, S., Heywood, K. J., Kim, T., Lee, S. H., Nicholls, K., Stanton, T., Truffer, M., Webber, B. G. M., Jenkins, A., Jacobs, S., Bindschadler, R., and Holland, D. M. (2016a). Sensitivity of Pine Island Glacier to observed ocean forcing. *Geophysical Research Letters*, 43(20):10,817–10,825.

Christianson, K., Jacobel, R. W., Horgan, H. J., Alley, R. B., Anandakrishnan, S., Holland, D. M., and DallaSanta, K. J. (2016b). Basal conditions at the grounding zone of Whillans Ice Stream, West Antarctica, from ice-penetrating radar. *Journal of Geophysical Research: Earth Surface*, 121(11):1954–1983.

Clark, J. A. and Lingle, C. S. (1977). Future sea-level changes due to West Antarctic ice sheet fluctuations. *Nature*, 269(5625):206–209.

Clarke, T. S., Liu, C., Lord, N. E., and Bentley, C. R. (2000). Evidence for a recently abandoned shear margin adjacent to ice stream B2, Antarctica, from ice-penetrating radar measurements. *Journal of Geophysical Research: Solid Earth*, 105(B6):13409–13422.

Clyne, E. R., Anandakrishnan, S., Muto, A., Alley, R. B., and Voigt, D. E. (2020). Interpretation of topography and bed properties beneath Thwaites Glacier, West Antarctica using seismic reflection methods. *Earth and Planetary Science Letters*, 550:116543.

Colgan, W., Rajaram, H., Abdalati, W., McCutchan, C., Mottram, R., Moussavi, M. S., and Grigsby, S. (2016). Glacier crevasses: Observations, models, and mass balance implications. *Reviews of Geophysics*, 54(1):119–161.

Colgan, W., Steffen, K., McLamb, W. S., Abdalati, W., Rajaram, H., Motyka, R., Phillips, T., and Anderson, R. (2011). An increase in crevasse extent, West Greenland: Hydrologic implications. *Geophysical Research Letters*, 38:L18502.

Conway, H., Catania, G., Raymond, C. F., Gades, A. M., Scambos, T. A., and Engelhardt, H. (2002). Switch of flow direction in an Antarctic ice stream. *Nature*, 419(6906):465–467.

Conway, H., Hall, B. L., Denton, G. H., Gades, A. M., and Waddington, E. D. (1999). Past and Future Grounding-Line Retreat of the West Antarctic Ice Sheet. *Science*, 286(5438):280–283.

Crawford, A. J., Benn, D. I., Todd, J., Åström, J. A., Bassis, J. N., and Zwinger, T. (2021). Marine ice-cliff instability modeling shows mixed-mode ice-cliff failure and yields calving rate parameterization. *Nature Communications*, 12:2701.

Cuffey, K. M. and Paterson, W. S. B. (2010). *The Physica of Glaciers*. Elsevier, Oxford, United Kingdom.

Dalziel, I. W. D. and Lawver, L. A. (2001). The Lithospheric Setting of the West Antarctic Ice Sheet. In *The West Antarctic Ice Sheet: Behavior and Environment*, volume 77 of *Antarctic Research Series*, pages 29–44. American Geophysical Union.

DeConto, R. M. and Pollard, D. (2016). Contribution of Antarctica to past and future sea-level rise. *Nature*, 531(7596):591–597.

Elsworth, C. W. and Suckale, J. (2016). Rapid ice flow rearrangement induced by subglacial drainage in West Antarctica. *Geophysical Research Letters*, 43(22):11,697–11,707.

Ely, J. C., Clark, C. D., Spagnolo, M., Stokes, C. R., Greenwood, S. L., Hughes, A. L., Dunlop, P., and Hess, D. (2016). Do subglacial bedforms comprise a size and shape continuum? *Geomorphology*, 257:108–119.

Ershadi, M. R., Drews, R., Martín, C., Eisen, O., Ritz, C., Corr, H., Christmann, J., Zeising, O., Humbert, A., and Mulvaney, R. (2022). Polarimetric radar reveals the spatial distribution of ice fabric at domes and divides in East Antarctica. *The Cryosphere*, 16(5):1719–1739.

Fahnestock, M. A., Scambos, T. A., Bindschadler, R. A., and Kvaran, G. (2000). A millen-

nium of variable ice flow recorded by the Ross Ice Shelf, Antarctica. *Journal of Glaciology*, 46(155):652–664.

Fischer, M. P., Alley, R. B., and Engelder, T. (1995). Fracture toughness of ice and firn determined from the modified ring test. *Journal of Glaciology*, 41(138):383–394.

Fleurian, B. d., Werder, M. A., Beyer, S., Brinkerhoff, D. J., Delaney, I., Dow, C. F., Downs, J., Gagliardini, O., Hoffman, M. J., Hooke, R. L., Seguinot, J., and Sommers, A. N. (2018). SHMIP The subglacial hydrology model intercomparison Project. *Journal of Glaciology*, 64(248):897–916.

Flowerdew, M., Millar, I., Curtis, M., Vaughan, A., Horstwood, M., Whitehouse, M., and Fanning, C. (2007). Combined U-Pb geochronology and Hf isotope geochemistry of detrital zircons from early Paleozoic sedimentary rocks, Ellsworth-Whitmore Mountains block, Antarctica. *GSA Bulletin*, 119(3-4):275–288.

Fowler, A. C. (1986). A sliding law for glaciers of constant viscosity in the presence of subglacial cavitation. *Proceedings of the Royal Society of London. A. Mathematical and Physical Sciences*, 407(1832):147–170.

Fretwell, P., Pritchard, H. D., Vaughan, D. G., Bamber, J. L., Barrand, N. E., Bell, R., Bianchi, C., Bingham, R. G., Blankenship, D. D., Casassa, G., Catania, G., Callens, D., Conway, H., Cook, A. J., Corr, H. F. J., Damaske, D., Damm, V., Ferraccioli, F., Forsberg, R., Fujita, S., Gim, Y., Gogineni, P., Griggs, J. A., Hindmarsh, R. C. A., Holmlund, P., Holt, J. W., Jacobel, R. W., Jenkins, A., Jokat, W., Jordan, T., King, E. C., Kohler, J., Krabill, W., Riger-Kusk, M., Langley, K. A., Leitchenkov, G., Leuschen, C., Luyendyk, B. P., Matsuoka, K., Mouginot, J., Nitsche, F. O., Nogi, Y., Nost, O. A., Popov, S. V., Rignot, E., Rippin, D. M., Rivera, A., Roberts, J., Ross, N., Siegert, M. J., Smith, A. M., Steinhage, D., Studinger, M., Sun, B., Tinto, B. K., Welch, B. C., Wilson, D., Young, D. A., Xiangbin, C., and Zirizzotti, A. (2013). Bedmap2: improved ice bed, surface and thickness datasets for Antarctica. *The Cryosphere*, 7(1):375–393.

Fricker, H. A., Scambos, T., Bindschadler, R., and Padman, L. (2007). An Active Subglacial Water System in West Antarctica Mapped from Space. *Science*, 315(5818):1544–1548.

Friedl, P., Weiser, F., Fluhrer, A., and Braun, M. H. (2019). Remote sensing of glacier and ice sheet grounding lines: A review. *Earth-Science Reviews*, 201:102948.

Fujita, S., Maeno, H., and Matsuoka, K. (2006). Radio-wave depolarization and scattering within ice sheets: a matrix-based model to link radar and ice-core measurements and its application. *Journal of Glaciology*, 52(178):407–424.

Gades, A. M., Raymond, C. F., Conway, H., and Jacobel, R. W. (2000). Bed properties of Siple Dome and adjacent ice streams, West Antarctica, inferred from radio-echo sounding measurements. *Journal of Glaciology*, 46(152):88–94.

Gagliardini, O., Zwinger, T., Gillet-Chaulet, F., Durand, G., Favier, L., Fleurian, B. d., Greve, R., Malinen, M., Martín, C., Råback, P., Ruokolainen, J., Sacchettini, M., Schäfer, M., Seddik, H., and Thies, J. (2013). Capabilities and performance of Elmer/Ice, a new-generation ice sheet model. *Geoscientific Model Development*, 6(4):1299–1318.

Gandy, N., Gregoire, L. J., Ely, J. C., Cornford, S. L., Clark, C. D., and Hodgson, D. M. (2019). Exploring the ingredients required to successfully model the placement, generation, and evolution of ice streams in the British-Irish Ice Sheet. *Quaternary Science Reviews*, 223:105915.

Gerber, T. A., Hvidberg, C. S., Rasmussen, S. O., Franke, S., Sinnl, G., Grinsted, A., Jansen, D., and Dahl-Jensen, D. (2021). Upstream flow effects revealed in the EastGRIP ice core using Monte Carlo inversion of a two-dimensional ice-flow model. *The Cryosphere*, 15(8):3655–3679.

Gibson, L. J. and Ashby, M. F. (1999). *Cellular Solids, Structure and Property*. Cambridge University Press, Cambridge, United Kingdom.

Gogineni, S., Chuah, T., Allen, C., Jezek, K., and Moore, R. K. (1998). An improved coherent radar depth sounder. *Journal of Glaciology*, 44(148):659–669.

Goldberg, D. N., Heimbach, P., Joughin, I., and Smith, B. (2015). Committed retreat of Smith, Pope, and Kohler Glaciers over the next 30 years inferred by transient model calibration. *The Cryosphere*, 9(6):2429–2446.

Gray, L., Joughin, I., Tulaczyk, S., Spikes, V. B., Bindschadler, R., and Jezek, K. (2005). Evidence for subglacial water transport in the West Antarctic Ice Sheet through three-dimensional satellite radar interferometry. *Geophysical Research Letters*, 32:L03501.

Haefeli, R. (1967). Some Results of the International Glaciological Expedition to Greenland 1957-1960: Concerning the Rheological Behaviour of Snow and Ice. In *Physics of Snow and Ice: proceedings*, volume 1 of *2*, pages 983–991.

Hall, B., Bromley, G., Stone, J., and Conway, H. (2016). Holocene ice recession at Polygon Spur, Reedy Glacier, Antarctica. *The Holocene*, 27(1):122–129.

Haran, T., Klinger, M., Bohlander, J., Fahnestock, M., Painter, T., and Scambos, T. (2018). MEaSUREs MODIS Mosaic of Antarctica 2013-2014 (MOA2014) Image Map, Version 1.

Harbor, J. and Warburton, J. (1993). Relative Rates of Glacial and Nonglacial Erosion in Alpine Environments. *Arctic and Alpine Research*, 25(1):1–7.

Haseloff, M. and Sergienko, O. V. (2018). The effect of buttressing on grounding line dynamics. *Journal of Glaciology*, 64(245):417–431.

Hillebrand, T. R., Conway, H., Koutnik, M., Martín, C., Paden, J., and Winberry, J. P. (2021). Radio-echo sounding and waveform modeling reveal abundant marine ice in former rifts and basal crevasses within Crary Ice Rise, Antarctica. *Journal of Glaciology*, 67(264):641–652.

Hills, B. H., Christianson, K., and Holschuh, N. (2020). A framework for attenuation method selection evaluated with ice-penetrating radar data at South Pole Lake. *Annals of Glaciology*, 61(81):176–187.

Hindmarsh, R. C. A., Vieli, G. J. C. L., Raymond, M. J., and Gudmundsson, G. H. (2006). Draping or overriding: The effect of horizontal stress gradients on internal layer ar-

chitecture in ice sheets. *Journal of Geophysical Research: Earth Surface (2003–2012)*, 111:F02018.

Hoffman, A. O., Christianson, K., Holschuh, N., Case, E., Kingslake, J., and Arthern, R. (2022). The Impact of Basal Roughness on Inland Thwaites Glacier Sliding. *Geophysical Research Letters*, 49:e2021GL096564.

Hoffman, A. O., Christianson, K., Shapero, D., Smith, B. E., and Joughin, I. (2020). Brief Communication: Heterogenous thinning and subglacial lake activity on Thwaites Glacier, West Antarctica. *The Cryosphere*, 14:4603–4609.

Hogan, K. A., Larter, R. D., Graham, A. G. C., Arthern, R., Kirkham, J. D., Minzoni, R. T., Jordan, T. A., Clark, R., Fitzgerald, V., Wåhlin, A. K., Anderson, J. B., Hillenbrand, C.-D., Nitsche, F. O., Simkins, L., Smith, J. A., Gohl, K., Arndt, J. E., Hong, J., and Wellner, J. (2020). Revealing the former bed of Thwaites Glacier using sea-floor bathymetry: implications for warm-water routing and bed controls on ice flow and buttressing. *The Cryosphere*, 14(9):2883–2908.

Holschuh, N., Christianson, K., Conway, H., Jacobel, R. W., and Welch, B. C. (2018). Persistent tracers of historic ice flow in glacial stratigraphy near Kamb Ice Stream, West Antarctica. *The Cryosphere*, 12(9):2821–2829.

Holschuh, N., Christianson, K., Paden, J., Alley, R. B., and Anandakrishnan, S. (2020). Linking postglacial landscapes to glacier dynamics using swath radar at Thwaites Glacier, Antarctica. *Geology*, 48:268–272.

Holschuh, N., Lilien, D. A., and Christianson, K. (2019). Thermal Weakening, Convergent Flow, and Vertical Heat Transport in the Northeast Greenland Ice Stream Shear Margins. *Geophysical Research Letters*, 46(14):8184–8193.

Holschuh, N., Pollard, D., Alley, R., and Anandakrishnan, S. (2014). Evaluating Marie Byrd Land stability using an improved basal topography. *Earth and Planetary Science Letters*, 408:362–369.

Horgan, H. J., Hulbe, C., Alley, R. B., Anandakrishnan, S., Goodsell, B., Taylor-Offord, S., and Vaughan, M. J. (2017). Poststagnation Retreat of Kamb Ice Stream's Grounding Zone. *Geophysical Research Letters*, 44(19):9815–9822.

Howat, I. M., Porter, C., Smith, B. E., Noh, M.-J., and Morin, P. (2019). The Reference Elevation Model of Antarctica. *The Cryosphere*, 13(2):665–674.

Hughes, T. J. (1981). The weak underbelly of the West Antarctic ice sheet. *Journal of Glaciology*, 27(97):518–525.

Hulbe, C. and Fahnestock, M. (2007). Century-scale discharge stagnation and reactivation of the Ross ice streams, West Antarctica. *Journal of Geophysical Research: Earth Surface (2003–2012)*, 112:F03S27.

Hulbe, C. L. and Fahnestock, M. A. (2004). West Antarctic ice-stream discharge variability: mechanism, controls and pattern of grounding-line retreat. *Journal of Glaciology*, 50(171):471–484.

Hunter, P., Meyer, C., Minchew, B., Haseloff, M., and Rempel, A. (2021). Thermal controls on ice stream shear margins. *Journal of Glaciology*, 67(263):435–449.

Huth, A., Duddu, R., and Smith, B. (2021). A Generalized Interpolation Material Point Method for Shallow Ice Shelves. 2: Anisotropic Nonlocal Damage Mechanics and Rift Propagation. *Journal of Advances in Modeling Earth Systems*, 13(8):e2020MS002292.

Jacobel, R. W., Scambos, T. A., Nereson, N. A., and Raymond, C. F. (2000). Changes in the margin of Ice Stream C, Antarctica. *Journal of Glaciology*, 46(152):102–110.

Jacobel, R. W., Welch, B. C., Osterhouse, D., Pettersson, R., and MacGregor, J. A. (2009). Spatial variation of radar-derived basal conditions on Kamb Ice Stream, West Antarctica. *Annals of Glaciology*, 50(51):10–16.

Jacobel, R. W., Welch, B. C., Steig, E. J., and Schneider, D. P. (2005). Glaciological and climatic significance of Hercules Dome, Antarctica: An optimal site for deep ice core drilling. *Journal of Geophysical Research: Earth Surface (2003–2012)*, 110:F01015.

Jacobs, S. S., Hellmer, H. H., and Jenkins, A. (1996). Antarctic Ice Sheet melting in the southeast Pacific. *Geophysical Research Letters*, 23(9):957–960.

Jacobsen, H. P. and Raymond, C. F. (1998). Thermal effects on the location of ice stream margins. *Journal of Geophysical Research*, 103(B6):12111–12122.

Jelitto, H. and Schneider, G. (2018). A geometric model for the fracture toughness of porous materials. *Acta Materialia*, 151:443–453.

Jenkins, A., Dutrieux, P., Jacobs, S. S., McPhail, S. D., Perrett, J. R., Webb, A. T., and White, D. (2010). Observations beneath Pine Island Glacier in West Antarctica and implications for its retreat. *Nature Geoscience*, 3(7):468–472.

Jenkins, A., Shoosmith, D., Dutrieux, P., Jacobs, S., Kim, T. W., Lee, S. H., Ha, H. K., and Stammerjohn, S. (2018). West Antarctic Ice Sheet retreat in the Amundsen Sea driven by decadal oceanic variability. *Nature Geoscience*, 11(10):733–738.

Jezek, K., Wu, X., Gogineni, P., Rodríguez, E., Freeman, A., Rodriguez-Morales, F., and Clark, C. D. (2011). Radar images of the bed of the Greenland Ice Sheet. *Geophysical Research Letters*, 38:L01501.

Jezek, K. C. (1999). Glaciological properties of the Antarctic ice sheet from RADARSAT-1 synthetic aperture radar imagery. *Annals of Glaciology*, 29:286–290.

Jezek, K. C., Curlander, J. C., Carsey, F., Wales, C., and Barry, R. G. (2013). RAMP AMM-1 SAR Image Mosaic of Antarctica, Version 2.

Jordan, T. A., Ferraccioli, F., and Forsberg, R. (2022a). An embayment in the East Antarctic basement constrains the shape of the Rodinian continental margin. *Communications Earth & Environment*, 3(1):52.

Jordan, T. A., Martin, C., Ferraccioli, F., Matsuoka, K., Corr, H., Forsberg, R., Olesen, A., and Siegert, M. (2018). Anomalously high geothermal flux near the South Pole. *Scientific Reports*, 8(1):16785.

Jordan, T. A., Riley, T. R., and Siddoway, C. S. (2020a). The geological history and evolution of West Antarctica. *Nature Reviews Earth & Environment*, 1(2):117–133.

Jordan, T. M., Cooper, M. A., Schroeder, D. M., Williams, C. N., Paden, J. D., Siegert, M. J., and Bamber, J. L. (2017). Self-affine subglacial roughness: consequences for radar scattering and basal water discrimination in northern Greenland. *The Cryosphere*, 11(3):1247–1264.

Jordan, T. M., Martín, C., Brisbourne, A. M., Schroeder, D. M., and Smith, A. M. (2022b). Radar Characterization of Ice Crystal Orientation Fabric and Anisotropic Viscosity Within an Antarctic Ice Stream. *Journal of Geophysical Research: Earth Surface*, 127:e2022JF006673.

Jordan, T. M., Schroeder, D. M., Elsworth, C. W., and Siegfried, M. R. (2020b). Estimation of ice fabric within Whillans Ice Stream using polarimetric phase-sensitive radar sounding. *Annals of Glaciology*, 61(81):74–83.

Joughin, I. (2018, updated 2019). MEaSUREs Greenland Monthly Ice Sheet Velocity Mosaics from SAR and Landsat, Version 1.

Joughin, I. and Alley, R. B. (2011). Stability of the West Antarctic ice sheet in a warming world. *Nature Geoscience*, 4(8):506–513.

Joughin, I., Bindschadler, R. A., King, M. A., Voigt, D., Alley, R. B., Anandakrishnan, S., Horgan, H., Peters, L., Winberry, P., Das, S. B., and Catania, G. (2005). Continued deceleration of Whillans Ice Stream, West Antarctica. *Geophysical Research Letters*, 32:L22501.

Joughin, I., MacAyeal, D. R., and Tulaczyk, S. (2004). Basal shear stress of the Ross ice streams from control method inversions. *Journal of Geophysical Research: Solid Earth*, 109:B09405.

Joughin, I., Shapero, D., Smith, B., Dutrieux, P., and Barham, M. (2021). Ice-shelf retreat drives recent Pine Island Glacier speedup. *Science Advances*, 7(24):eabg3080.

Joughin, I., Smith, B. E., and Abdalati, W. (2010). Glaciological advances made with interferometric synthetic aperture radar. *Journal of Glaciology*, 56(200):1026–1042.

Joughin, I., Smith, B. E., and Howat, I. (2018). Greenland ice mapping project: ice flow velocity variation at sub-monthly to decadal timescales. *The Cryosphere*, 12(7):2211–2227.

Joughin, I., Smith, B. E., and Medley, B. (2014). Marine Ice Sheet Collapse Potentially Under Way for the Thwaites Glacier Basin, West Antarctica. *Science*, 344(6185):735–738.

Joughin, I., Smith, B. E., and Schoof, C. G. (2019). Regularized coulomb friction laws for ice sheet sliding: Application to pine island glacier, antarctica. *Geophysical Research Letters*, 46:4764–4771.

Joughin, I. and Tulaczyk, S. (2002). Positive Mass Balance of the Ross Ice Streams, West Antarctica. *Science*, 295(5554):476–480.

Joughin, I., Tulaczyk, S., Bamber, J. L., Blankenship, D., Holt, J. W., Scambos, T., and Vaughan, D. G. (2009). Basal conditions for Pine Island and Thwaites Glaciers, West Antarctica, determined using satellite and airborne data. *Journal of Glaciology*, 55(190):245–257.

Joughin, I., Tulaczyk, S., Bindschadler, R., and Price, S. F. (2002). Changes in west Antarctic ice stream velocities: Observation and analysis. *Journal of Geophysical Research: Solid Earth*, 107(B11):2289, EPM 3–1–EPM 3–22.

Karner, G. D., Studinger, M., and Bell, R. E. (2005). Gravity anomalies of sedimentary basins and their mechanical implications: Application to the Ross Sea basins, West Antarctica. *Earth and Planetary Science Letters*, 235(3-4):577–596.

King, E. C., Hindmarsh, R. C. A., and Stokes, C. R. (2009). Formation of mega-scale glacial lineations observed beneath a West Antarctic ice stream. *Nature Geoscience*, 2(8):585–588.

King, M. (2004). Rigorous GPS data-processing strategies for glaciological applications. *Journal of Glaciology*, 50(171):601–607.

Kingslake, J., Hindmarsh, R. C. A., Aðalgeirsdóttir, G., Conway, H., Corr, H. F. J., Gillet-Chaulet, F., Martín, C., King, E. C., Mulvaney, R., and Pritchard, H. D. (2014). Full-depth englacial vertical ice sheet velocities measured using phase-sensitive radar. *Journal of Geophysical Research: Earth Surface*, 119(12):2604–2618.

Kingslake, J., Scherer, R. P., Albrecht, T., Coenen, J., Powell, R. D., Reese, R., Stansell, N. D., Tulaczyk, S., Wearing, M. G., and Whitehouse, P. L. (2018). Extensive retreat and re-advance of the West Antarctic Ice Sheet during the Holocene. *Nature*, 558(7710):430–434.

Korotkikh, E. V., Mayewski, P. A., Handley, M. J., Sneed, S. B., Introne, D. S., Kurbatov, A. V., Dunbar, N. W., and McIntosh, W. C. (2011). The last interglacial as represented in the glaciochemical record from Mount Moulton Blue Ice Area, West Antarctica. *Quaternary Science Reviews*, 30(15-16):1940–1947.

Kyrke-Smith, T. M., Gudmundsson, G. H., and Farrell, P. E. (2018). Relevance of Detail in Basal Topography for Basal Slipperiness Inversions: A Case Study on Pine Island Glacier, Antarctica. *Frontiers in Earth Science*, 6:33.

Lai, C.-Y., Kingslake, J., Wearing, M. G., Chen, P.-H. C., Gentine, P., Li, H., Spergel, J. J., and Wessem, J. M. v. (2020). Vulnerability of Antarctica's ice shelves to meltwater-driven fracture. *Nature*, 584(7822):574–578.

Lhermitte, S., Sun, S., Shuman, C., Wouters, B., Pattyn, F., Wuite, J., Berthier, E., and Nagler, T. (2020). Damage accelerates ice shelf instability and mass loss in Amundsen Sea Embayment. *Proceedings of the National Academy of Sciences*, 117(40):24735–24741.

Lilien, D. A., Hills, B. H., Driscol, J., Jacobel, R., and Christianson, K. (2020). ImpDAR: an open-source impulse radar processor. *Annals of Glaciology*, 61(81):114–123.

Lisiecki, L. E. and Raymo, M. E. (2005). A Pliocene-Pleistocene stack of 57 globally distributed benthic δ18O records. *Paleoceanography*, 20:PA1003.

Lomonaco, R., Albert, M., and Baker, I. (2011). Microstructural evolution of fine-grained

layers through the firn column at summit, greenland. *Journal of Glaciology*, 57(204):755–762.

Lowry, D. P., Golledge, N. R., Bertler, N. A. N., Jones, R. S., and McKay, R. (2019). Deglacial grounding-line retreat in the Ross Embayment, Antarctica, controlled by ocean and atmosphere forcing. *Science Advances*, 5(8):eaav8754.

Lucchitta, B., Mullins, K., Allison, A., and Ferrigno, J. G. (1993). Antarctic glacier-tongue velocities from landsat images: first results. *Annals of Glaciology*, 17:356–366.

MacAyeal, D. R. (1989). Large-scale ice flow over a viscous basal sediment: Theory and application to ice stream B, Antarctica. *Journal of Geophysical Research: Solid Earth*, 94(B4):4071–4087.

MacGregor, J. A., Catania, G. A., Conway, H., Schroeder, D. M., Joughin, I., Young, D. A., Kempf, S. D., and Blankenship, D. D. (2013). Weak bed control of the eastern shear margin of Thwaites Glacier, West Antarctica. *Journal of Glaciology*, 59(217):900–912.

MacGregor, J. A., Li, J., Paden, J. D., Catania, G. A., Clow, G. D., Fahnestock, M. A., Gogineni, S. P., Grimm, R. E., Morlighem, M., Nandi, S., Seroussi, H., and Stillman, D. E. (2015). Radar attenuation and temperature within the Greenland Ice Sheet. *Journal of Geophysical Research: Earth Surface*, 120(6):983–1008.

Maiti, S. K., Ashby, M. F., and Gibson, L. J. (1984). Fracture toughness of brittle cellular solids. *Scripta Metallurgy*, 18:213–217.

Mantelli, E., Bertagni, M. B., and Ridolfi, L. (2016). Stochastic ice stream dynamics. *Proceedings of the National Academy of Sciences*, 113(32):E4594–E4600.

Marsh, O., Price, D., Courville, Z., and Floricioiu, D. (2021). Crevasse and rift detection in Antarctica from TerraSAR-X satellite imagery. *Cold Regions Science and Technology*, 187:103284.

Matsuoka, K., Gades, A., Conway, H., Catania, G., and Raymond, C. F. (2009a). Radar

signatures beneath a surface topographic lineation near the outlet of Kamb Ice Stream and Engelhardt Ice Ridge, West Antarctica. *Annals of Glaciology*, 50(51):98–104.

Matsuoka, K., Hindmarsh, R. C., Moholdt, G., Bentley, M. J., Pritchard, H. D., Brown, J., Conway, H., Drews, R., Durand, G., Goldberg, D., Hattermann, T., Kingslake, J., Lenaerts, J. T., Martín, C., Mulvaney, R., Nicholls, K. W., Pattyn, F., Ross, N., Scambos, T., and Whitehouse, P. L. (2015). Antarctic ice rises and rumples: Their properties and significance for ice-sheet dynamics and evolution. *Earth-Science Reviews*, 150:724–745.

Matsuoka, K., MacGregor, J. A., and Pattyn, F. (2012). Predicting radar attenuation within the Antarctic ice sheet. *Earth and Planetary Science Letters*, 359:173–183.

Matsuoka, K., Morse, D., and Raymond, C. F. (2010). Estimating englacial radar attenuation using depth profiles of the returned power, central West Antarctica. *Journal of Geophysical Research: Earth Surface*, 115:F02012.

Matsuoka, K., Wilen, L., Hurley, S. P., and Raymond, C. F. (2009b). Effects of Birefringence Within Ice Sheets on Obliquely Propagating Radio Waves. *IEEE Transactions on Geoscience and Remote Sensing*, 47(5):1429–1443.

McCarthy, C., Savage, H., and Nettles, M. (2017). Temperature dependence of ice-on-rock friction at realistic glacier conditions. *Philosophical Transactions of the Royal Society A: Mathematical, Physical and Engineering Sciences*, 375(2086):20150348.

McClung, D. and Schaerer, P. A. (2006). *The Avalanche Handbook*. The Mountaineers Books, Seattle, WA, USA.

Meier, M., Lundstrom, S., Stone, D., Kamb, B., Engelhardt, H., Humphrey, N., Dunlap, W. W., Fahnestock, M., Krimmel, R. M., and Walters, R. (1994). Mechanical and hydrologic basis for the rapid motion of a large tidewater glacier: 1. Observations. *Journal of Geophysical Research: Solid Earth*, 99(B8):15219–15229.

Meyer, C. R. and Minchew, B. M. (2018). Temperate ice in the shear margins of the Antarctic Ice Sheet: Controlling processes and preliminary locations. *Earth and Planetary Science Letters*, 498:17–26.

Minchew, B. M. and Meyer, C. R. (2020). Dilation of subglacial sediment governs incipient surge motion in glaciers with deformable beds. *Proceedings of the Royal Society A*, 476(2238):20200033.

Moholdt, G., Padman, L., and Fricker, H. A. (2014). Basal mass budget of Ross and Filchner-Ronne ice shelves, Antarctica, derived from Lagrangian analysis of ICESat altimetry. *Journal of Geophysical Research: Earth Surface*, 119(11):2361–2380.

Moore, J. C., Gladstone, R., Zwinger, T., and Wolovick, M. (2018). Geoengineer polar glaciers to slow sea-level rise. *Nature*, 555(7696):303–305.

Morlighem, M. (2011). *Ice sheet properties inferred by combining numerical modeling and remote sensing data*. PhD thesis, Ecole Centrale Paris.

Morlighem, M., Rignot, E., Binder, T., Blankenship, D., Drews, R., Eagles, G., Eisen, O., Ferraccioli, F., Forsberg, R., Fretwell, P., Goel, V., Greenbaum, J. S., Gudmundsson, H., Guo, J., Helm, V., Hofstede, C., Howat, I., Humbert, A., Jokat, W., Karlsson, N. B., Lee, W. S., Matsuoka, K., Millan, R., Mouginot, J., Paden, J., Pattyn, F., Roberts, J., Rosier, S., Ruppel, A., Seroussi, H., Smith, E. C., Steinhage, D., Sun, B., Broeke, M. R. v. d., Ommen, T. D. v., Wessem, M. v., and Young, D. A. (2020). Deep glacial troughs and stabilizing ridges unveiled beneath the margins of the Antarctic ice sheet. *Nature Geoscience*, 13(2):132–137.

Morris, E. M. and Wingham, D. J. (2014). Densification of polar snow: Measurements, modeling, and implications for altimetry. *Journal of Geophysical Research: Earth Surface*, 119(2):349–365.

Mouginot, J., Rignot, E., and Scheuchl, B. (2019). Continent-Wide, Interferometric SAR Phase, Mapping of Antarctic Ice Velocity. *Geophysical Research Letters*, 46:9710–9718.

Mouginot, J., Rignot, E., Scheuchl, B., and Millan, R. (2017). Comprehensive Annual Ice Sheet Velocity Mapping Using Landsat-8, Sentinel-1, and RADARSAT-2 Data. *Remote Sensing*, 9(4):364.

Muto, A., Anandakrishnan, S., and Alley, R. B. (2013). Subglacial bathymetry and sediment layer distribution beneath the Pine Island Glacier ice shelf, West Antarctica, modeled using aerogravity and autonomous underwater vehicle data. *Annals of Glaciology*, 54(64):27–32.

Muto, A., Anandakrishnan, S., Alley, R. B., Horgan, H. J., Parizek, B. R., Koellner, S., Christianson, K., and Holschuh, N. (2019). Relating bed character and subglacial morphology using seismic data from Thwaites Glacier, West Antarctica. *Earth and Planetary Science Letters*, 507:199–206.

Muto, A., Peters, L. E., Gohl, K., Sasgen, I., Alley, R. B., Anandakrishnan, S., and Riverman, K. L. (2016). Subglacial bathymetry and sediment distribution beneath Pine Island Glacier ice shelf modeled using aerogravity and in situ geophysical data: New results. *Earth and Planetary Science Letters*, 433:63–75.

Nereson, N. and Raymond, C. (2001). The elevation history of ice streams and the spatial accumulation pattern along the Siple Coast of West Antarctica inferred from ground-based radar data from three inter-ice-stream ridges. *Journal of Glaciology*, 47(157):303–313.

Ng, F. and Conway, H. (2004). Fast-flow signature in the stagnated Kamb Ice Stream, West Antarctica. *Geology*, 32(6):481–484.

NISAR (2018). *NASA-ISRO SAR (NISAR) Mission Science Users' Handbook*. NASA Jet Propulsion Laboratory, Pasadena, CA, USA.

Nye, J. F. (1959). A Method of Determining the Strain-Rate Tensor at the Surface of a Glacier. *Journal of Glaciology*, 3(25):409–419.

Orsi, A. J., Cornuelle, B. D., and Severinghaus, J. P. (2012). Little Ice Age cold interval in West Antarctica: Evidence from borehole temperature at the West Antarctic Ice Sheet (WAIS) Divide. *Geophysical Research Letters*, 39:L09710.

Oswald, G. K. A. and Robin, G. d. Q. (1973). Lakes Beneath the Antarctic Ice Sheet. *Nature*, 245(5423):251–254.

Paden, J., Akins, T., Dunson, D., Allen, C., and Gogineni, P. (2010). Ice-sheet bed 3-D tomography. *Journal of Glaciology*, 56(195):3–11.

Pankhurst, R. J., Storey, B. C., Millar, I. L., Macdonald, D., and Vennum, W. R. (1988). Cambrian-Ordovician magmatism in the Thiel Mountains, Transantarctic Mountains, and implications for the Beardmore orogeny. *Geology*, 16(3):246–249.

Paxman, G. J. G., Jamieson, S. S. R., Ferraccioli, F., Jordan, T. A., Bentley, M. J., Ross, N., Forsberg, R., Matsuoka, K., Steinhage, D., Eagles, G., and Casal, T. G. (2019). Subglacial Geology and Geomorphology of the Pensacola-Pole Basin, East Antarctica. *Geochemistry, Geophysics, Geosystems*, 20(6):2786–2807.

Perol, T. and Rice, J. R. (2015). Shear heating and weakening of the margins of West Antarctic ice streams. *Geophysical Research Letters*, 42(9):3406–3413.

Plouff, D. (1976). Gravity and Magnetic Fields of Polygonal Prisms and Application to Magnetic Terrain Corrections. *Geophysics*, 41(4):727–741.

Pollard, D. and DeConto, R. M. (2009). Modelling West Antarctic ice sheet growth and collapse through the past five million years. *Nature*, 458(7236):329–332.

Press, W. H., Teukolsky, S. A., Vetterling, W. T., and Flannery, B. P. (2007). *Numerical recipes 3rd edition: The art of scientific computing.* Cambridge University Press, Cambridge, United Kingdom.

Rathmann, N. M., Lilien, D. A., Grinsted, A., Gerber, T. A., Young, T. J., and Dahl-Jensen, D. (2022). On the Limitations of Using Polarimetric Radar Sounding to Infer the Crystal Orientation Fabric of Ice Masses. *Geophysical Research Letters*, 49:e2021GL096244.

Raymo, M. E. and Mitrovica, J. X. (2012). Collapse of polar ice sheets during the stage 11 interglacial. *Nature*, 483(7390):453–456.

Raymond, C. (1996). Shear margins in glaciers and ice sheets. *Journal of Glaciology*, 42(140):90–102.

Raymond, C., Catania, G. A., Nereson, N., and Veen, C. v. d. (2006). Bed radar reflectivity across the north margin of Whillans Ice Stream, West Antarctica, and implications for margin processes. *Journal of Glaciology*, 52(176):3–10.

Raymond, C. F. (1983). Deformation in the Vicinity of Ice Divides. *Journal of Glaciology*, 29(103):357–373.

Raymond, C. F. (2000). Energy balance of ice streams. *Journal of Glaciology*, 46(155):665–674.

Reese, R., Gudmundsson, G. H., Levermann, A., and Winkelmann, R. (2018). The far reach of ice-shelf thinning in antarctica. *Nature Climate Change*, 8(1):53–57.

Retzlaff, R. and Bentley, C. R. (1993). Timing of stagnation of Ice Stream C, West Antarctica, from short-pulse radar studies of buried surface crevasses. *Journal of Glaciology*, 39(133):553–561.

Riel, B., Minchew, B., and Bischoff, T. (2021). Data-Driven Inference of the Mechanics of Slip Along Glacier Beds Using Physics-Informed Neural Networks: Case Study on Rutford Ice Stream, Antarctica. *Journal of Advances in Modeling Earth Systems*, 13(11):e2021MS002621.

Rignot, E., Echelmeyer, K., and Krabill, W. (2001). Penetration depth of interferometric synthetic-aperture radar signals in snow and ice. *Geophysical Research Letters*, 28(18):3501–3504.

Rignot, E., Mouginot, J., Morlighem, M., Seroussi, H., and Scheuchl, B. (2014). Widespread, rapid grounding line retreat of Pine Island, Thwaites, Smith, and Kohler glaciers, West Antarctica, from 1992 to 2011. *Geophysical Research Letters*, 41(10):3502–3509.

Rignot, E., Mouginot, J., Scheuchl, B., Broeke, M. v. d., Wessem, M. J. v., and Morlighem, M. (2019). Four decades of Antarctic Ice Sheet mass balance from 1979–2017. *Proceedings of the National Academy of Sciences*, 116(4):1095–1103.

Rist, M. A., Sammonds, P. R., Murrell, S. A. F., Meredith, P. G., Doake, C. S. M., Oerter, H., and Matsuki, K. (1999). Experimental and theoretical fracture mechanics applied to Antarctic ice fracture and surface crevassing. *Journal of Geophysical Research: Solid Earth*, 104(B2):2973–2987.

Rist, M. A., Sammonds, P. R., Oerter, H., and Doake, C. S. M. (2002). Fracture of Antarctic shelf ice. *Journal of Geophysical Research: Solid Earth*, 107(B1):ECV 2–1–ECV 2–13.

Robel, A. A., Roe, G. H., and Haseloff, M. (2018). Response of Marine-Terminating Glaciers to Forcing: Time Scales, Sensitivities, Instabilities, and Stochastic Dynamics. *Journal of Geophysical Research: Earth Surface*, 123(9):2205–2227.

Robin, G. d. Q., Evans, S., and Bailey, J. T. (1969). Interpretation of Radio Echo Sounding in Polar Ice Sheets. *Philosophical Transactions of the Royal Society of London, Series A*, 265(1166):437–505.

Rohling, E. J., Grant, K., Bolshaw, M., Roberts, A. P., Siddall, M., Hemleben, C., and Kucera, M. (2009). Antarctic temperature and global sea level closely coupled over the past five glacial cycles. *Nature Geoscience*, 2(7):500–504.

Ronneberger, O., Fischer, P., and Brox, T. (2015). Medical Image Computing and Computer-Assisted Intervention – MICCAI 2015, 18th International Conference, Munich, Germany, October 5-9, 2015, Proceedings, Part III. *Lecture Notes in Computer Science*, pages 234–241.

Rose, K. C., Ferraccioli, F., Jamieson, S. S., Bell, R. E., Corr, H., Creyts, T. T., Braaten, D., Jordan, T. A., Fretwell, P. T., and Damaske, D. (2013). Early East Antarctic Ice Sheet growth recorded in the landscape of the Gamburtsev Subglacial Mountains. *Earth and Planetary Science Letters*, 375:1–12.

Ross, N., Jordan, T. A., Bingham, R. G., Corr, H. F., Ferraccioli, F., Brocq, A. L., Rippin, D. M., Wright, A. P., and Siegert, M. J. (2014). The Ellsworth Subglacial Highlands: Inception and retreat of the West Antarctic Ice Sheet. *Geological Society of America Bulletin*, 126(1-2):3–15.

Rossetti, F., Storti, F., Busetti, M., Lisker, F., Vincenzo, G. D., Läufer, A. L., Rocchi, S., and Salvini, F. (2006). Eocene initiation of Ross Sea dextral faulting and implications for East Antarctic neotectonics. *Journal of the Geological Society*, 163(1):119–126.

Salvini, F., Brancolini, G., Busetti, M., Storti, F., Mazzarini, F., and Coren, F. (1997). Cenozoic geodynamics of the Ross Sea region, Antarctica: Crustal extension, intraplate strike-slip faulting, and tectonic inheritance. *Journal of Geophysical Research: Solid Earth*, 102(B11):24669–24696.

Scambos, T., Bell, R., Alley, R., Anandakrishnan, S., Bromwich, D., Brunt, K., Christianson, K., Creyts, T., Das, S., DeConto, R., Dutrieux, P., Fricker, H., Holland, D., MacGregor, J., Medley, B., Nicolas, J., Pollard, D., Siegfried, M., Smith, A., Steig, E., Trusel, L., Vaughan, D., and Yager, P. (2017). How much, how fast?: A science review and outlook for research on the instability of Antarctica's Thwaites Glacier in the 21st century. *Global and Planetary Change*, 153:16–34.

Scheuchl, B., Mouginot, J., and Rignot, E. (2012). Ice velocity changes in the Ross and Ronne sectors observed using satellite radar data from 1997 and 2009. *The Cryosphere*, 6(5):1019–1030.

Schoof, C. (2002). Basal perturbations under ice streams: form drag and surface expression. *Journal of Glaciology*, 48(162):407–416.

Schoof, C. (2007). Ice sheet grounding line dynamics: Steady states, stability, and hysteresis. *Journal of Geophysical Research: Earth Surface*, 112:F03S28.

Schroeder, D. M., Bingham, R. G., Blankenship, D. D., Christianson, K., Eisen, O., Flowers, G. E., Karlsson, N. B., Koutnik, M. R., Paden, J. D., and Siegert, M. J. (2020). Five decades of radioglaciology. *Annals of Glaciology*, 61(81):1–13.

Schulson, E. M., Baker, I., Robertson, C. D., Bolon, R. B., and Harnimon, R. J. (1989). Fractography of ice. *Journal of Materials Science Letters*, 8(10):1193–1194.

Scott, J. B., Smith, A. M., Bingham, R. G., and Vaughan, D. G. (2010). Crevasses triggered

on Pine Island Glacier, West Antarctica, by drilling through an exceptional melt layer. *Annals of Glaciology*, 51(55):65–70.

Seroussi, H., Morlighem, M., Rignot, E., Mouginot, J., Larour, E., Schodlok, M., and Khazendar, A. (2014). Sensitivity of the dynamics of Pine Island Glacier, West Antarctica, to climate forcing for the next 50 years. *The Cryosphere*, 8(5):1699–1710.

Shabtaie, S., Whillans, I. M., and Bentley, C. R. (1987). The morphology of ice streams A, B, and C, west Antarctica, and their environs. *Journal of Geophysical Research: Solid Earth*, 92(B9):8865–8883.

Shackleton, N. J., Sánchez-Goñi, M. F., Pailler, D., and Lancelot, Y. (2003). Marine Isotope Substage 5e and the Eemian Interglacial. *Global and Planetary Change*, 36(3):151–155.

Shapero, D., Badgeley, J., and Hoffman, A. (2020). icepack: glacier flow modeling with the finite element method in Python.

Shapero, D. R., Joughin, I. R., Poinar, K., Morlighem, M., and Gillet-Chaulet, F. (2016). Basal resistance for three of the largest Greenland outlet glaciers. *Journal of Geophysical Research: Earth Surface*, 121(1):168–180.

Shepherd, A., Gilbert, L., Muir, A. S., Konrad, H., McMillan, M., Slater, T., Briggs, K. H., Sundal, A. V., Hogg, A. E., and Engdahl, M. E. (2019). Trends in Antarctic Ice Sheet Elevation and Mass. *Geophysical Research Letters*, 46(14):8174–8183.

Shepherd, A., Ivins, E. R., A, G., Barletta, V. R., Bentley, M. J., Bettadpur, S., Briggs, K. H., Bromwich, D. H., Forsberg, R., Galin, N., Horwath, M., Jacobs, S., Joughin, I., King, M. A., Lenaerts, J. T. M., Li, J., Ligtenberg, S. R. M., Luckman, A., Luthcke, S. B., McMillan, M., Meister, R., Milne, G., Mouginot, J., Muir, A., Nicolas, J. P., Paden, J., Payne, A. J., Pritchard, H., Rignot, E., Rott, H., Sørensen, L. S., Scambos, T. A., Scheuchl, B., Schrama, E. J. O., Smith, B., Sundal, A. V., Angelen, J. H. v., Berg, W. J. v. d., Broeke, M. R. v. d., Vaughan, D. G., Velicogna, I., Wahr, J., Whitehouse, P. L., Wingham, D. J., Yi, D., Young, D., and Zwally, H. J. (2012). A Reconciled Estimate of Ice-Sheet Mass Balance. *Science*, 338(6111):1183–1189.

Shreve, R. L. (1972). Movement of Water in Glaciers *. *Journal of Glaciology*, 11(62):205–214.

Siegert, M. J., Taylor, J., Payne, A. J., and Hubbard, B. (2004a). Macro-scale bed roughness of the siple coast ice streams in West Antarctica. *Earth Surface Processes and Landforms*, 29(13):1591–1596.

Siegert, M. J., Welch, B., Morse, D., Vieli, A., Blankenship, D. D., Joughin, I., King, E. C., Vieli, G. J.-M. C. L., Payne, A. J., and Jacobel, R. (2004b). Ice Flow Direction Change in Interior West Antarctica. *Science*, 305(5692):1948–1951.

Siegfried, M. R., Fricker, H. A., Carter, S. P., and Tulaczyk, S. (2016). Episodic ice velocity fluctuations triggered by a subglacial flood in West Antarctica. *Geophysical Research Letters*, 43(6):2640–2648.

Siegfried, M. R., Fricker, H. A., Roberts, M., Scambos, T. A., and Tulaczyk, S. (2014). A decade of West Antarctic subglacial lake interactions from combined ICESat and CryoSat-2 altimetry. *Geophysical Research Letters*, 41(3):891–898.

Smith, B., Fricker, H. A., Gardner, A. S., Medley, B., Nilsson, J., Paolo, F. S., Holschuh, N., Adusumilli, S., Brunt, K., Csatho, B., Harbeck, K., Markus, T., Neumann, T., Siegfried, M. R., and Zwally, H. J. (2020). Pervasive ice sheet mass loss reflects competing ocean and atmosphere processes. *Science*, 368(6496):1239–1242.

Smith, B. E., Bentley, C. R., and Raymond, C. F. (2005). Recent elevation changes on the ice streams and ridges of the Ross Embayment from ICESat crossovers. *Geophysical Research Letters*, 32:L21S09.

Smith, B. E., Fricker, H. A., Joughin, I. R., and Tulaczyk, S. (2009). An inventory of active subglacial lakes in Antarctica detected by ICESat (2003–2008). *Journal of Glaciology*, 55(192):573–595.

Smith, B. E., Gourmelen, N., Huth, A., and Joughin, I. (2017). Connected subglacial lake drainage beneath Thwaites Glacier, West Antarctica. *The Cryosphere*, 11(1):451–467.

Smith, B. E., Lord, N. E., and Bentley, C. R. (2002). Crevasse ages on the northern margin of Ice Stream C, West Antarctica. *Annals of Glaciology*, 34:209–216.

Smith, T. R., Schulson, M. E., and Schulson, E. M. (1990). The fracture toughness of porous ice with and without particles. In *Proceedings of the Ninth International Conference on Offshore Mechanics and Arctic Engineering*, volume 4 of *Antarctic Research Series*, pages 241–247. American Society of Mechanical Engineers.

SNAP (2022). SNAP - ESA Sentinel Application Platform, S1TBX.

Spagnolo, M., Clark, C. D., Ely, J. C., Stokes, C. R., Anderson, J. B., Andreassen, K., Graham, A. G. C., and King, E. C. (2014). Size, shape and spatial arrangement of mega-scale glacial lineations from a large and diverse dataset. *Earth Surface Processes and Landforms*, 39(11):1432–1448.

Spector, P., Stone, J., Cowdery, S. G., Hall, B., Conway, H., and Bromley, G. (2017). Rapid early-Holocene deglaciation in the Ross Sea, Antarctica. *Geophysical Research Letters*, 44(15):7817–7825.

Steen-Larsen, H. C., Waddington, E. D., and Koutnik, M. R. (2010). Formulating an inverse problem to infer the accumulation-rate pattern from deep internal layering in an ice sheet using a Monte Carlo approach. *Journal of Glaciology*, 56(196):318–332.

Steig, E. J., Huybers, K., Singh, H. A., Steiger, N. J., Ding, Q., Frierson, D. M. W., Popp, T., and White, J. W. C. (2015). Influence of West Antarctic Ice Sheet collapse on Antarctic surface climate. *Geophysical Research Letters*, 42(12):4862–4868.

Stone, J. O., Balco, G. A., Sugden, D. E., Caffee, M. W., III, L. C. S., Cowdery, S. G., and Siddoway, C. (2003). Holocene Deglaciation of Marie Byrd Land, West Antarctica. *Science*, 299(5603):99–102.

Storey, B. C., Macdonald, D. I. M., Dalziel, I. W. D., Isbell, J. L., and Millar, I. L. (1996). Early Paleozoic sedimentation, magmatism, and deformation in the Pensacola Mountains, Antarctica: The significance of the Ross orogeny. *Geological Society of America Bulletin*, 108(6):685–707.

Suckale, J., Platt, J. D., Perol, T., and Rice, J. R. (2014). Deformation-induced melting in the margins of the West Antarctic ice streams. *Journal of Geophysical Research: Earth Surface*, 119(5):1004–1025.

Taylor, J., Siegert, M. J., Payne, A. J., and Hubbard, B. (2004). Regional-scale bed roughness beneath ice masses: measurement and analysis. *Computers & Geosciences*, 30(8):899–908.

Todd, C., Stone, J., Conway, H., Hall, B., and Bromley, G. (2010). Late Quaternary evolution of Reedy Glacier, Antarctica. *Quaternary Science Reviews*, 29(11-12):1328–1341.

Trey, H., Cooper, A. K., Pellis, G., Vedova, B. d., Cochrane, G., Brancolini, G., and Makris, J. (1999). Transect across the West Antarctic rift system in the Ross Sea, Antarctica. *Tectonophysics*, 301(1-2):61–74.

Turney, C. S. M., Fogwill, C. J., Golledge, N. R., McKay, N. P., Sebille, E. v., Jones, R. T., Etheridge, D., Rubino, M., Thornton, D. P., Davies, S. M., Ramsey, C. B., Thomas, Z. A., Bird, M. I., Munksgaard, N. C., Kohno, M., Woodward, J., Winter, K., Weyrich, L. S., Rootes, C. M., Millman, H., Albert, P. G., Rivera, A., Ommen, T. v., Curran, M., Moy, A., Rahmstorf, S., Kawamura, K., Hillenbrand, C.-D., Weber, M. E., Manning, C. J., Young, J., and Cooper, A. (2020). Early Last Interglacial ocean warming drove substantial ice mass loss from Antarctica. *Proceedings of the National Academy of Sciences*, 117(8):3996–4006.

Ultee, L. and Bassis, J. (2016). The future is Nye: an extension of the perfect plastic approximation to tidewater glaciers. *Journal of Glaciology*, 62(236):1143–1152.

USGS (2021). Lidar for Yosemite National Park. USGS 3D Elevation Program (3DEP).

Van Liefferinge, B. and Pattyn, F. (2013). Using ice-flow models to evaluate potential sites of million year-old ice in antarctica. *Climate of the Past*, 9(5):2335–2345.

Vaughan, D. G. (1993). Relating the occurrence of crevasses to surface strain rates. *Journal of Glaciology*, 39(132):255–266.

Vaughan, D. G., Corr, H. F. J., Doake, C. S. M., and Waddington, E. D. (1999). Distortion of isochronous layers in ice revealed by ground-penetrating radar. *Nature*, 398(6725):323–326.

Veen, C. J. v. d. (1999). Crevasses on glaciers. *Polar Geography*, 23(3):213–245.

Venturelli, R. A., Siegfried, M. R., Roush, K. A., Li, W., Burnett, J., Zook, R., Fricker, H. A., Priscu, J. C., Leventer, A., and Rosenheim, B. E. (2020). Mid-Holocene Grounding Line Retreat and Readvance at Whillans Ice Stream, West Antarctica. *Geophysical Research Letters*, 47:e2020GL08847.

Vieli, G. J.-M. C. L., Martín, C., Hindmarsh, R. C. A., and Lüthi, M. P. (2018). Basal freeze-on generates complex ice-sheet stratigraphy. *Nature Communications*, 9(1):4669.

Vieli, G.-M. L., Hindmarsh, R., and Siegert, M. (2007). Three-dimensional flow influences on radar layer stratigraphy. *Annals of Glaciology*, 46:22–28.

Waite, A. H. and Schmidt, S. (1962). Gross Errors in Height Indication from Pulsed Radar Altimeters Operating over Thick Ice or Snow. In *Proceedings of the Ninth International Conference on Offshore Mechanics and Arctic Engineering*, volume 5(60) of *Proceedings of the Institute of Radio Engineers*, pages 1515–1520. Institute of Electrical and Electronics Engineers.

Weertman, J. (1957). On the Sliding of Glaciers. *Journal of Glaciology*, 3(21):33–38.

Weertman, J. (1964). The Theory of Glacier Sliding. *Journal of Glaciology*, 5(39):287–303.

Welch, B. C. and Jacobel, R. W. (2003). Analysis of deep-penetrating radar surveys of West Antarctica, US-ITASE 2001. *Geophysical Research Letters*, 30(8):1444, 27–1–27–4.

Welch, B. C. and Jacobel, R. W. (2005). Bedrock topography and wind erosion sites in East Antarctica: observations from the 2002 US-ITASE traverse. *Annals of Glaciology*, 41:92–96.

Welch, P. D. (1967). The Use of Fast Fourier Transform for the Estimation of Power Spectra: Method Based on Time Averaging Over Short, Modified Periodograms. *IEEE Transactions on Acoustics, Speech, and Signal Processing*, 15:70–73.

Winberry, J. P., Anandakrishnan, S., Alley, R. B., Bindschadler, R. A., and King, M. A. (2009). Basal mechanics of ice streams: Insights from the stick-slip motion of Whillans Ice Stream, West Antarctica. *Journal of Geophysical Research: Earth Surface (2003–2012)*, 114:F01016.

Winberry, J. P., Anandakrishnan, S., Alley, R. B., Wiens, D. A., and Pratt, M. J. (2014). Tidal pacing, skipped slips and the slowdown of Whillans Ice Stream, Antarctica. *Journal of Glaciology*, 60(222):795–807.

Winebrenner, D. P., Smith, B. E., Catania, G. A., Conway, H. B., and Raymond, C. F. (2003). Radio-frequency attenuation beneath Siple Dome,West Antarctica, from wide-angle and profiling radar observations. *Annals of Glaciology*, 37:226–232.

Wingham, D. J., Siegert, M. J., Shepherd, A., and Muir, A. S. (2006). Rapid discharge connects Antarctic subglacial lakes. *Nature*, 440(7087):1033–1036.

Winter, K., Ross, N., Ferraccioli, F., Jordan, T. A., Corr, H. F. J., Forsberg, R., Matsuoka, K., Olesen, A. V., and Casal, T. G. (2018). Topographic Steering of Enhanced Ice Flow at the Bottleneck Between East and West Antarctica. *Geophysical Research Letters*, 45(10):4899–4907.

Young, D. A., Wright, A. P., Roberts, J. L., Warner, R. C., Young, N. W., Greenbaum, J. S., Schroeder, D. M., Holt, J. W., Sugden, D. E., Blankenship, D. D., Ommen, T. D. v., and Siegert, M. J. (2011). A dynamic early East Antarctic Ice Sheet suggested by ice-covered fjord landscapes. *Nature*, 474(7349):72–75.

Young, T. J., Martín, C., Christoffersen, P., Schroeder, D. M., Tulaczyk, S. M., and Dawson, E. J. (2021a). Rapid and accurate polarimetric radar measurements of ice crystal fabric orientation at the Western Antarctic Ice Sheet (WAIS) Divide ice core site. *The Cryosphere*, 15(8):4117–4133.

Young, T. J., Schroeder, D. M., Jordan, T. M., Christoffersen, P., Tulaczyk, S. M., Culberg, R., and Bienert, N. L. (2021b). Inferring Ice Fabric From Birefringence Loss in Airborne Radargrams: Application to the Eastern Shear Margin of Thwaites Glacier, West Antarctica. *Journal of Geophysical Research: Earth Surface*, 126:e2020JF006023.

Zoet, L. K. and Iverson, N. R. (2020). A slip law for glaciers on deformable beds. *Science*, 368(6486):76–78.

Zwally, H. J., Abdalati, W., Herring, T., Larson, K., Saba, J., and Steffen, K. (2002). Surface melt-induced acceleration of greenland ice-sheet flow. *Science*, 297(5579):218–222.

Appendix A

SUPPLEMENT OF "BRIEF COMMUNICATION: HETEROGENOUS THINNING AND SUBGLACIAL LAKE ACTIVITY ON THWAITES GLACIER, WEST ANTARCTICA"

A.1 Introduction

Here we provide additional information on the glaciostatic hydropotential time series, water routing, and describe the diagnostic model simulations we use to interrogate the influence of lake fill-drain cycles on basal resistance and ice sliding velocity.

A.2 Lake volume change

We applied the same SAR LOS methods to measure vertical displacements on the lakes identified by Smith et al. (2017) to estimate lake volume change on the lakes identified in the western Haynes Glacier shear margin (Fig. A.1) We also created average lake volume change estimates from the gridded CryoSat-2 time series (Fig. A.2). We note that ice velocity changes are not detectable in SAR data outside of lake polygons (Fig. A.3). This suggests that the velocity signals observed with GNSS are below the detection threshold of the SAR data and/or very spatially limited in extent.

A.3 Hydropotential, water routing, and lake volume change

From the CryoSat-2 elevation change time series, we construct quarterly models of glaciostatic hydraulic potential. We first calculate a reference elevation model associated with the drained lakes. In the lake polygons, anomalous height change relative to background thinning is linked to filling and draining of subglacial water. Following Shreve (1972), we estimate the glaciostatic hydropotential as

$$\phi_g = P_q + \rho_{water} g z \tag{A.1}$$

where the water pressure at each quarter, P_q, is assumed to be near the sum of the overburden stress of ice and lake water thickness, H_q and h_q, respectively:

$$P_q = \rho_{ice} g H_q + \rho_{water} g h_q \tag{A.2}$$

We then derive subglacial water fluxes multiplying the flow accumulation associated with the hydraulic potential time series by the distributed basal-melt field derived by Joughin et al. (2009). We assume the melt rates are stationary relative to the ongoing thinning and derive water routing beneath Thwaites Glacier (Fig. A.4) (see Supplement Movie 1 in Hoffman et al., 2020). The water routing between the lakes remains relatively constant, despite local elevation changes as the lakes fill and drain and a general increase the hydraulic potential difference between the lakes as the lower reaches of Thwaites Glacier thin.

A.4 Inversions of basal friction

Modelled ice temperature depends on the inferred basal shear stress and ice viscosity because of their combined effect on frictional and strain heating near the bed. Ice viscosity is best described by a temperature-dependent Arrhenius relation, which makes simultaneous inferences of ice rheology and basal friction difficult to separate from snapshot observations of ice thickness and velocity. In our diagnostic inversions for bed friction and the enhancement factor, we use the ice-flow model icepack (Shapero et al., 2020) to solve the weak form of the shallow-shelf equations (Bueler and Brown, 2009), modified to include frictional energy dissipation:

$$F(u) = \int_\Omega \tau \left(\left(u_0^{\frac{1}{m}+1} + |u|^{\frac{1}{m}+1} \right)^{\frac{m}{m}+1} - u_0 \right) dx. \tag{A.3}$$

This functional describes the stress accommodation of the bed assuming a regularized Coulomb friction law (Joughin et al., 2019). We iteratively refine our proxies for bed resistance, $\tau = \tau_0 e^\beta$, and the fluidity in Glen's flow law, $A = A_0 e^\theta$, using the Gauss-Newton method to perturb parameters β and θ to minimize the objective functional:

$$E(u) = \int_\Omega \left(\frac{u - u_{obs}}{\sigma} \right)^2 dx, \tag{A.4}$$

where u are the modelled velocities and σ are the standard deviations of the measured SAR velocities, u_{obs}. In our iterative inversion scheme, we first calculate the depth-averaged enhancement factor from the 3D temperatures derived by Van Liefferinge and Pattyn (2013) and use this initial estimate to infer an initial basal shear stress field. For the floating eastern Thwaites Ice Shelf, where we do not have independently modelled ice temperatures, we assume a constant viscosity before advecting the initial temperature solution through the shelf (∼20 years of spin up). We do not include the rifted western Thwaites Ice Shelf in our model domain because we find it provides almost no backstress to grounded ice, which is in agreement with previous work (Lucchitta et al., 1993; Reese et al., 2018). Because almost all relative motion is accommodated by sliding in the shallow-shelf equations, our procedure overestimates shear stress at the ice-bed interface; however, our interest in differences between two representative model periods (before and after the lakes drain) makes this model assumption less impactful. Figure A.5 shows the results of these simulations where deviations of shear stress inside the lake are smaller than outside the lake. This suggests that the lake fill-drain cycles have only minimal and/or temporary effects on ice dynamics both locally and for the broader basin.

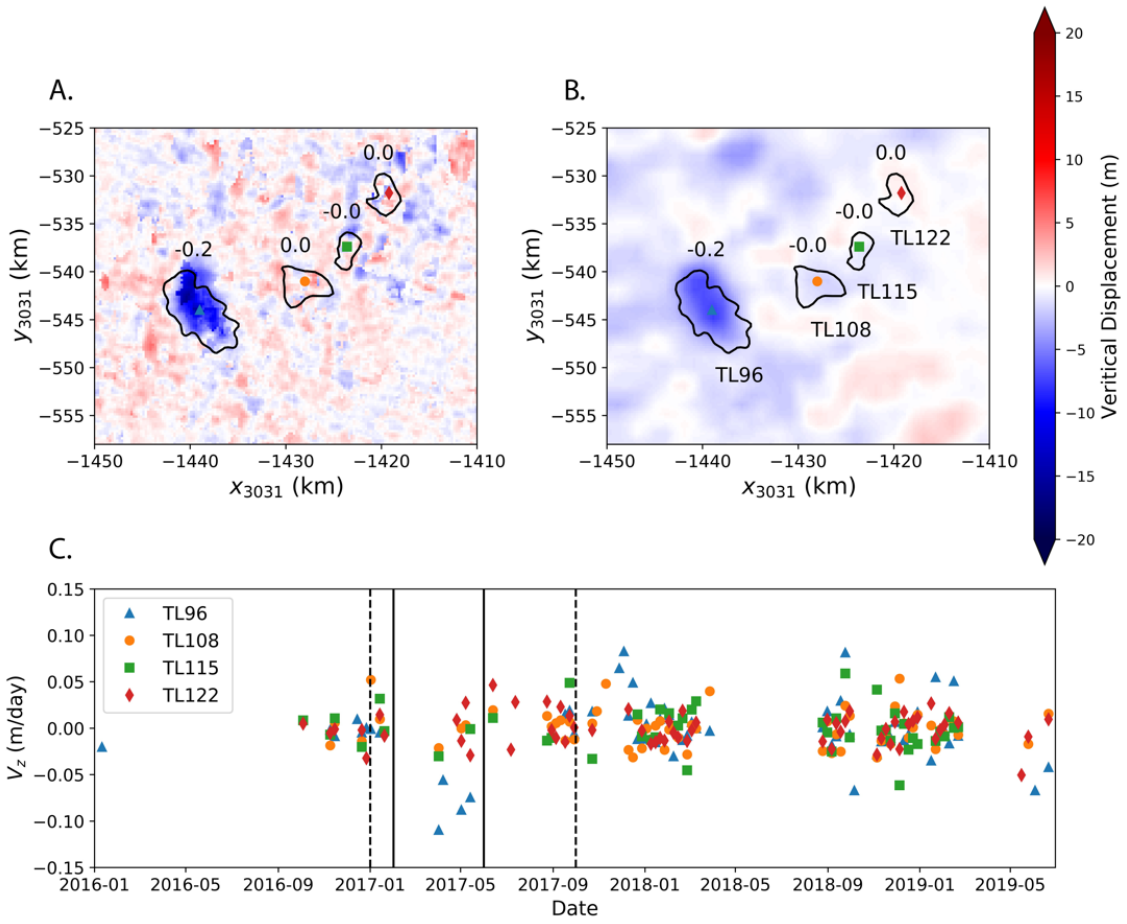

Figure A.1: Surface elevation-change time series over the Haynes Glacier lakes showing the 2017 drainage event from (A) vertical displacement computed from integrated vertical displacement rates (V_z) from Sentinel-1 SAR data and (B) swath-processed radar altimetry in a polar stereographic projection (EPSG:3031). Water volume (km^3) associated with observed vertical displacement is labelled for each lake. (C) Time series of uplift rates (V_z) from SAR LOS results (coloured dots, left abscissa; locations marked in panels A and B) and horizontal speed from GNSS observations (right abscissa). Solid lines represent period over which SAR vertical displacements (V_z) were integrated to produce the vertical displacements shown in panel A. Dotted lines represent the quarters of gridded CryoSat-2 data differenced to create panel B.

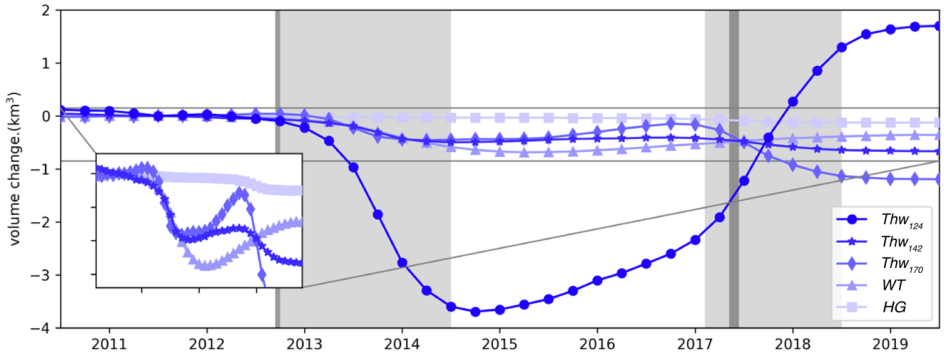

Figure A.2: Volume change for all observed subglacial lakes over the complete observation period derived from CryoSat-2 data by subtracting an average thinning rate outside the lake from the average elevation change in the lake and multiplying by the lake area.

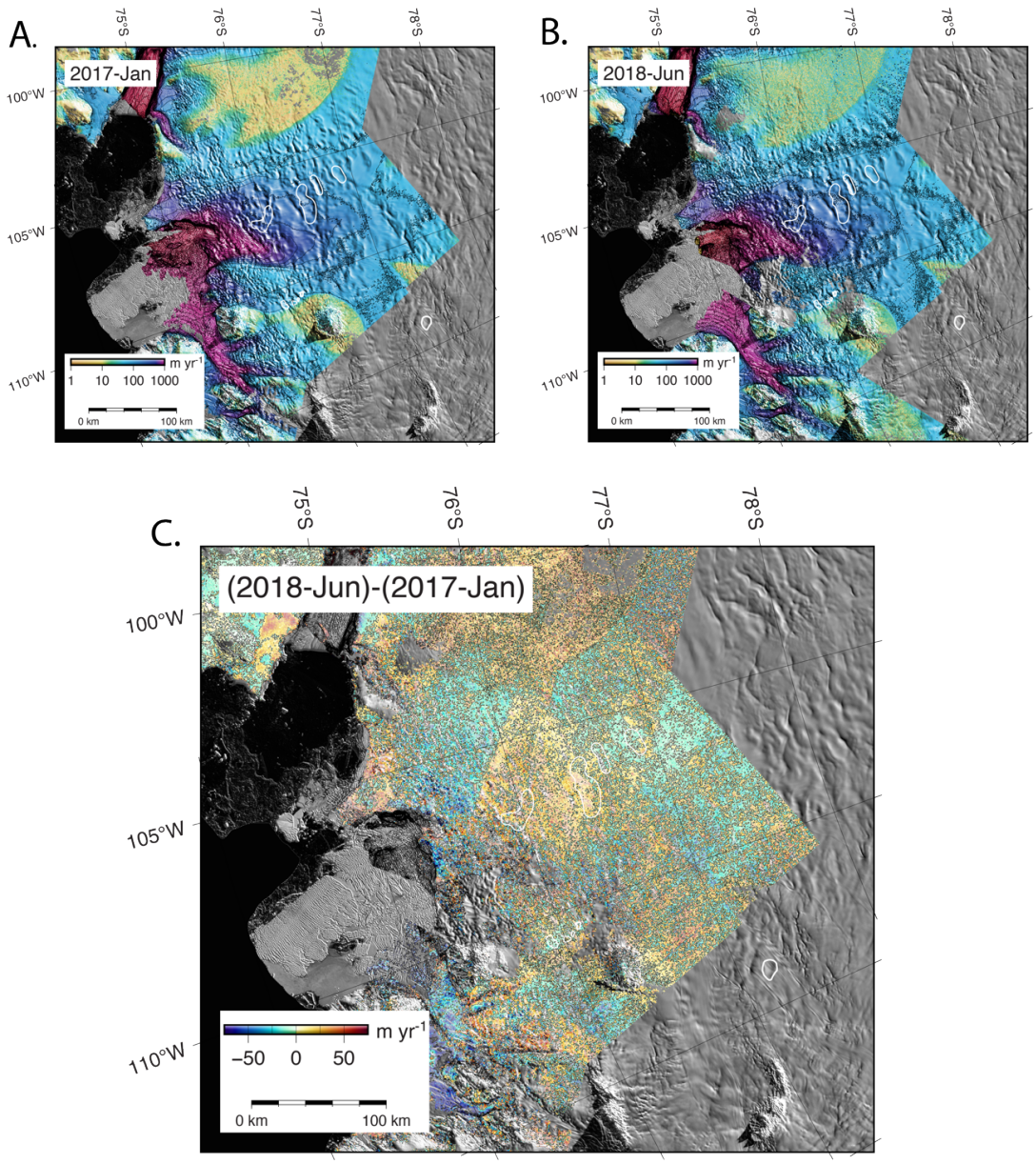

Figure A.3: Distributed velocities from SAR image pairs with centre acquisition dates (A) 01/2017 and (B) 01/2018 with (C) velocity difference (01/2018-01/2017). There are no detectable changes in velocity associated with the drainage of lakes Thw_{142} and Thw_{170} into lake Thw_{124} or the Haynes Glacier lake drainage.

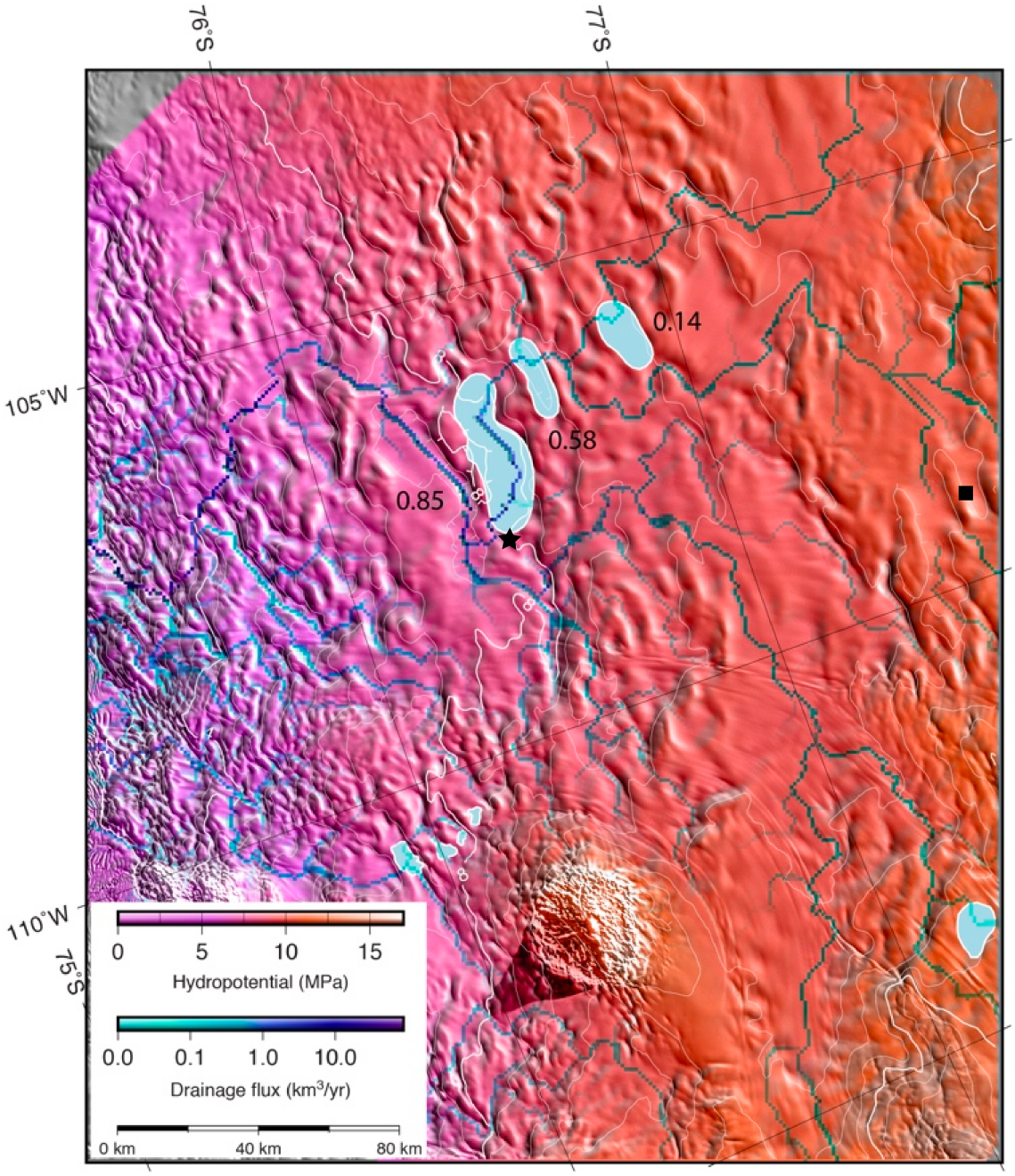

Figure A.4: Average water flux assuming static hydropotential and basal-melt rates (Joughin et al., 2009). Supplement Move SV1 in Hoffman et al. (2020) shows weak sensitivity for water rerouting as the glacier thins and the lakes fill and drain. The cumulative water fluxes (km^3/yr) into lakes $Thw_{124,142,170}$ are printed with each lake. Black star and square indicate sites of LTHW and UTHW GNSS.

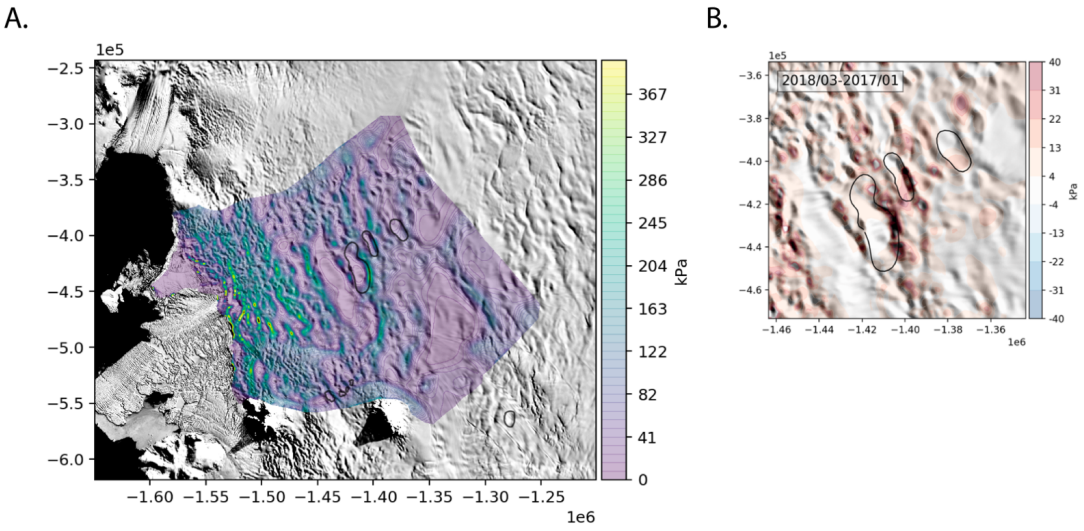

Figure A.5: Static inversion for basal resistance field for 2017 catchment geometry (A) before the Haynes Glacier and Thwaites Glacier drainage events and (B) difference in inferred basal resistance between two static inversions from 2017 and 2018 (before and after the 2017 drainage cascade) for lakes $\text{Thw}_{124,142,170}$.

Appendix B

SUPPORTING INFORMATION FOR "THE IMPACT OF BASAL ROUGHNESS ON INLAND THWAITES GLACIER SLIDING"

B.1 Analytic slip length calculation

In glacier sliding theory, slip length (L) is defined as:

$$L = \frac{\eta}{\beta} \tag{B.1}$$

where η is ice viscosity and β is the basal drag coefficient. If the slip length is larger than the ice thickness, the basal drag is too small to induce shear in the ice column, and ice slides over the substrate at a uniform velocity with depth (plug flow). If the slip length is smaller than the ice thickness, then basal drag can induce substantial shearing through the ice column, esulting in a depth-variable velocity profile. Slip length is thus a useful metric for distinguishing the ice-flow regime.

We compare slip lengths calculated from our modeled parameter fields to slip lengths calculated using analytic theory for form drag for ice flow over an undulating bed that requires only bed roughness power spectra as an input (Schoof, 2002). Similar to Hogan et al. (2020), we approximate one sided periodograms of the along-flow bed roughness profiles derived from the radar swath topographies (Holschuh et al., 2020) using an inverse square power law (equivalent to a random-walk elevation profile), where the periodogram component (P_n) associated with each frequency band can be fit by:

$$P_n = A f_n^{-2} \tag{B.2}$$

where A is a fit coefficient with units of length and $f_n = n/a$ is the center frequency of a frequency band of width $1/a$, a is the length of the fit window, and $n = 1 \ldots N$ with N being the total number of components in the periodogram (here $N = 256$). Following

Schoof (2002) and Hogan et al. (2020), for sufficiently high wavenumbers ($k_n \gg 1/H$ where H is ice thickness) the basal drag components are given by:

$$\beta_n = 16\eta\pi^3 A a^{-1} f_n. \tag{B.3}$$

The total form drag coefficient can then be approximated by:

$$\beta = \sum_{n=1}^{N} \beta_n = 16\eta\pi^3 A a^{-2} \sum_{n=1}^{N} n = 8\eta\pi^3 A a^{-2} N\,(N+1) \tag{B.4}$$

and if $\lambda_n \ll a$ so $N \gg 1$, then

$$\beta = 8\eta\pi^3 A \lambda_N^{-2}. \tag{B.5}$$

Applying the definition of slip length then gives:

$$L = \frac{\lambda_N^2}{8\pi^3 A}. \tag{B.6}$$

We apply this analytic theory to our swath topographies to calculate the slip lengths associated with form drag. First, we extract bed topography at 25 m posting from the radar swath topography point cloud (Holschuh et al., 2020) at each point in the point cloud along 6.4-km long flowlines (distance chosen to be similar to Hogan et al. (2020)) determined using the simulation reference surface velocity field. After removing the linear trend from the bed elevation profile and applying a Hamming window, we calculate the one-sided periodogram using Welch's method (Welch, 1967). The inverse square power law coefficient was calculated using non-linear least squares fitting. The slip length calculated following Equation B.6 is plotted at the center point of each flowline.

B.2 Consistency with observed subglacial lake activity?

An active subglacial lake boundary (lake Thw_{124}; Smith et al., 2017) identified from satellite altimetry lies partially within the lower Thwaites grid. The inferred shear stress inside the lake boundary is nonzero. Satellite observations suggest variability in the lake fill-drain levels on Thwaites Glacier (Hoffman et al., 2020), so volume change estimates of lakes on Thwaites

Glacier derived from satellite altimetry are difficult to relate to changes in lake geometry. Because the lake geometry is unknown for the observational period used to constrain the snap-shot inversions, we do not know how much of the lake is buoyantly supporting the overlying ice. This lake had drained prior to the epoch of the surface observations used to constrain the inversion, so the non-zero drag may be evidence of ice regrounding; however, independent GNSS observations suggest that ice velocity is insensitive to lake fill-drain cycles, which would predict low shear stress values in the vicinity of the Thwaites lakes independent of whether the lake is full or empty (Hoffman et al., 2020). The nonzero drag inside the lake could also represent resistance from topographic pinning points that may always protrude above the reported lake depth (Smith et al., 2017; Hoffman et al., 2020), which at $\sim$ 20 m, is below the root mean square amplitude of subglacial roughness in the boundary of the lake and motivates further study of lake influence on ice-sheet mechanics and glacier sliding. In the two-dimensional spectral variance of 6.0-km windowed bed topography, we see the first indication from independent subglacial datasets of spatial changes in bed properties consistent with the Thw_{124} lake position. Over the lake outline boundary, the bed appears to be substantially smoother than the surrounding topography (Fig. 3.3a). The SAR focused radargrams, however, show no unambiguous evidence of an ice-lake interface. This suggests that there may not be dielectric contrast across the lake interface that is distinguishable from a wet sediment interface and/or that this interface is very rough.

B.3 Simulations over a uniformly sloped bed topography

Fitting a plane to the high-resolution topographies, we can simulate ice flow over a flat bed for each grid. From these simulations, we can relate the basal drag to the more the more traditional horizontal shear stress (a global variable) and compare again the resistance and normal pressure fields. The patterns of the inferred resistance fields are similar to the smoothed topographies. The cost per node for each grid is substantially higher than the isotropically smoothed experiments.

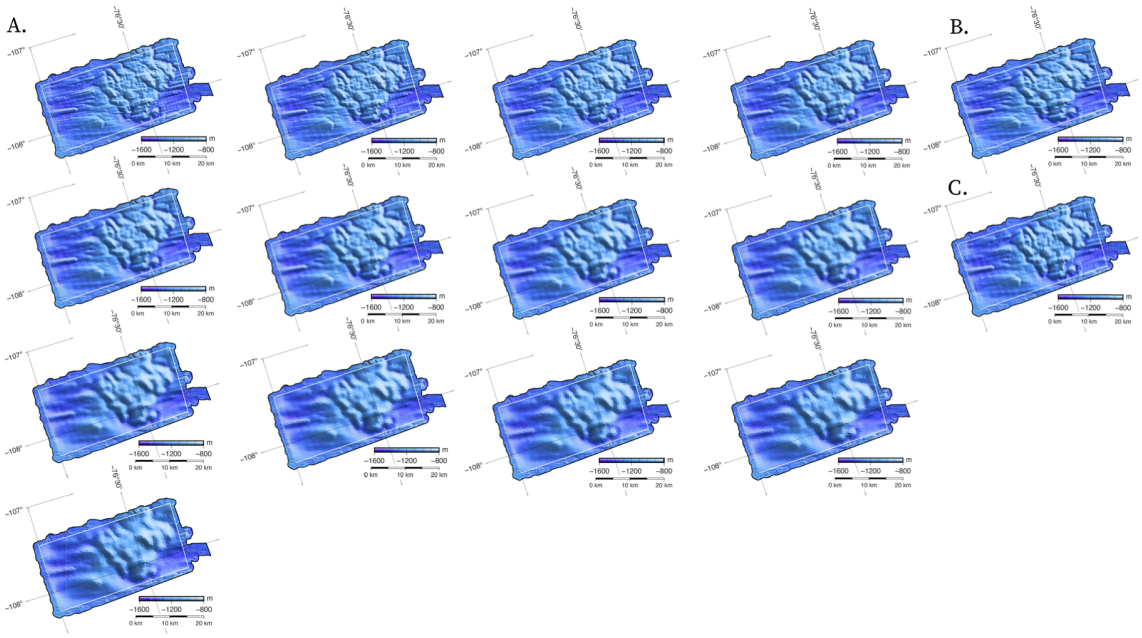

Figure B.1: The (A) topographies of the isotropically filtered grids for lower Thwaites Glacier, and the (B) along-flow and (C) transverse anisotropically filtered topographies for the lower Thwaites Glacier grid.

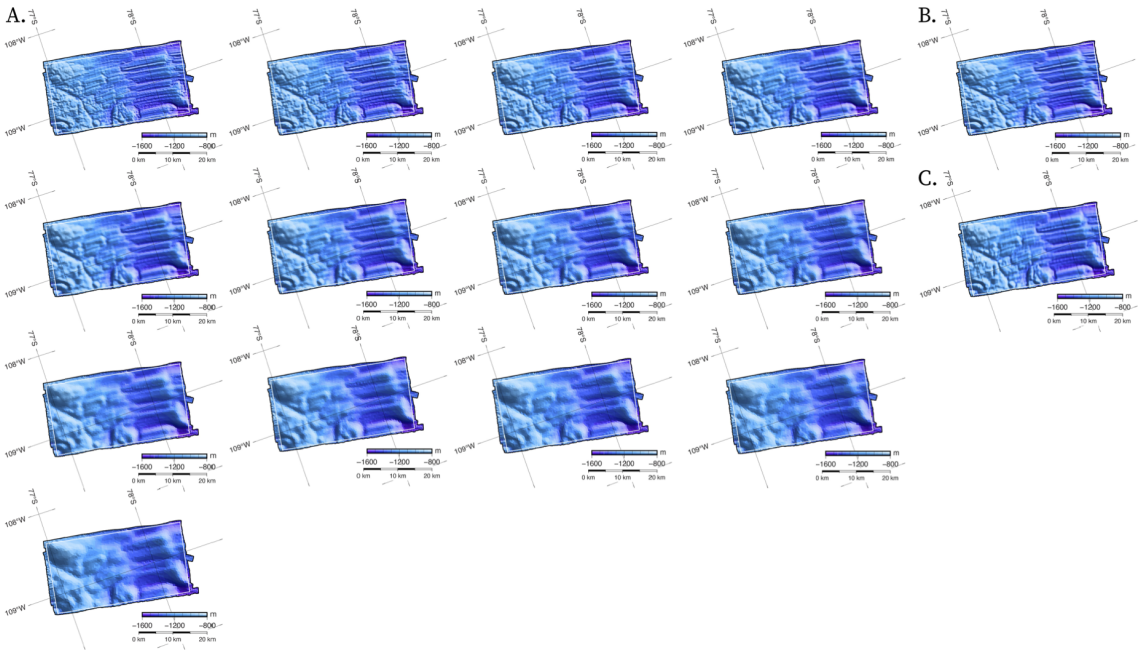

Figure B.2: The (A) topographies of the isotropically filtered grids for upper Thwaites Glacier, and the (B) along-flow and (C) transverse anisotropically filtered topographies for the upper Thwaites Glacier grid.

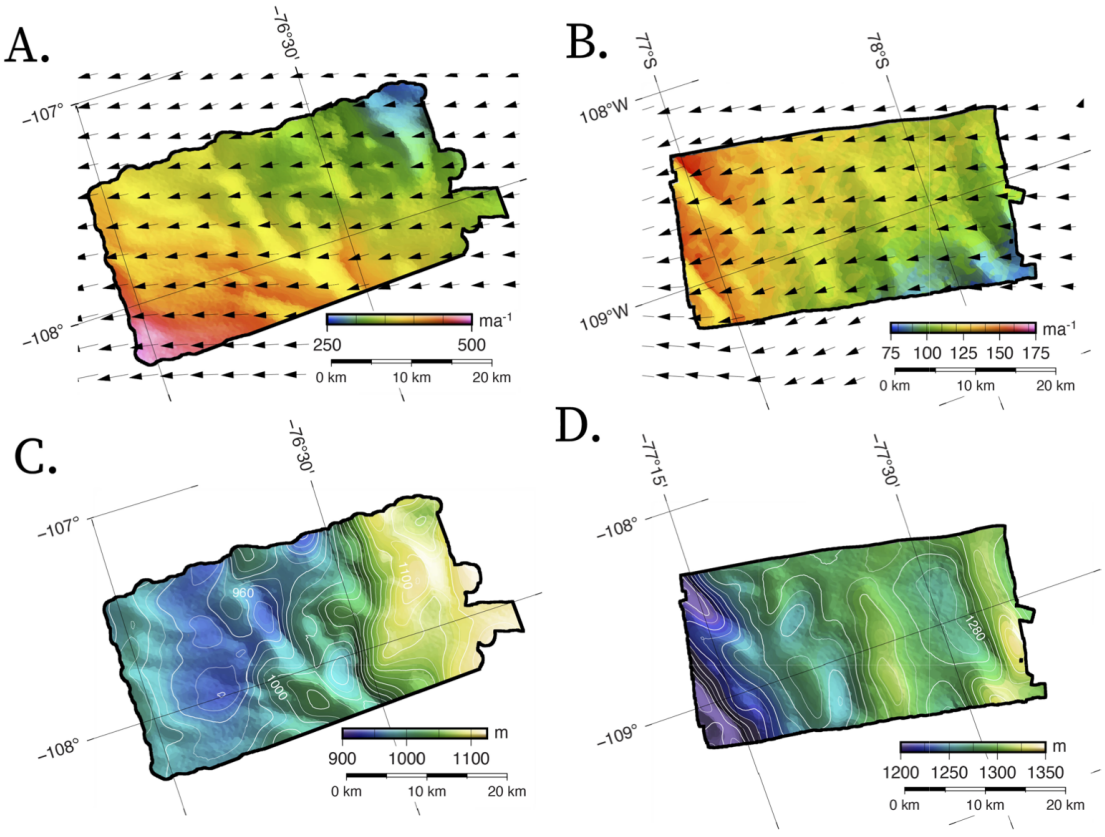

Figure B.3: The (A,B) surface velocity and (C,D) surface elevation for the lower and upper Thwaites grids. Note, color maps are scaled uniquely for each grid.

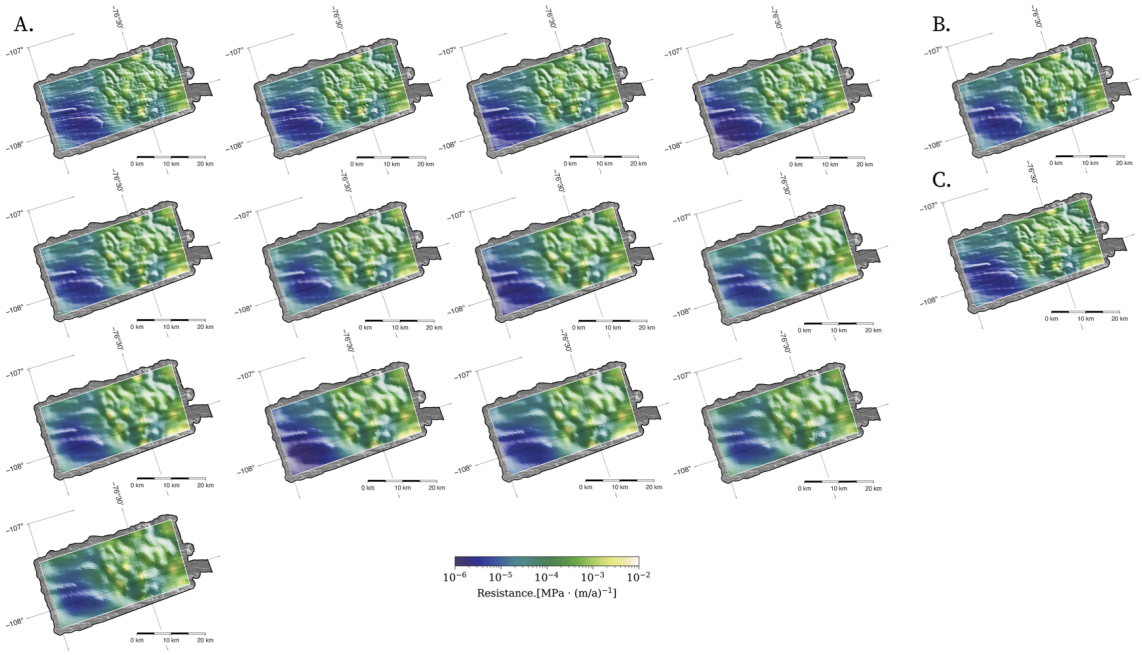

Figure B.4: The (A) inferred friction coefficient of each of the isotropically filtered lower Thwaites grid simulations, and (B) along-flow and (C) transverse anisotropically filtered inferred friction coefficient simulations for the lower Thwaites Glacier grids.

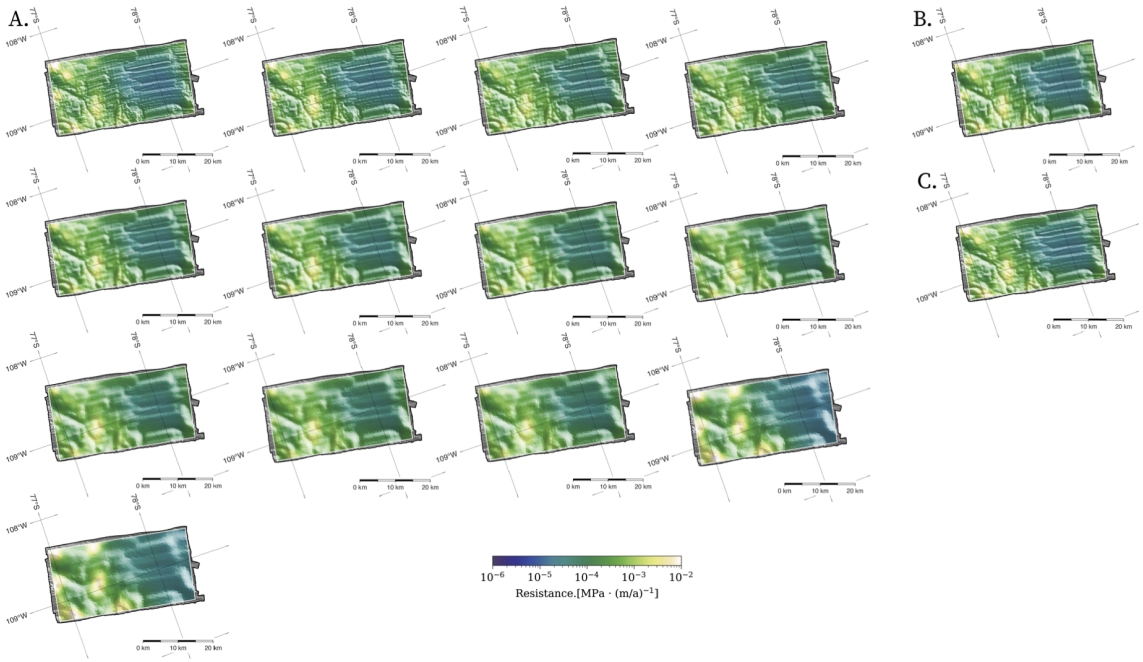

Figure B.5: The (A) inferred friction coefficient of each of the isotropically filtered upper Thwaites grid simulations, and (B) along-flow and (C) transverse anisotropically filtered inferred friction coefficient simulations for the upper Thwaites Glacier grids.

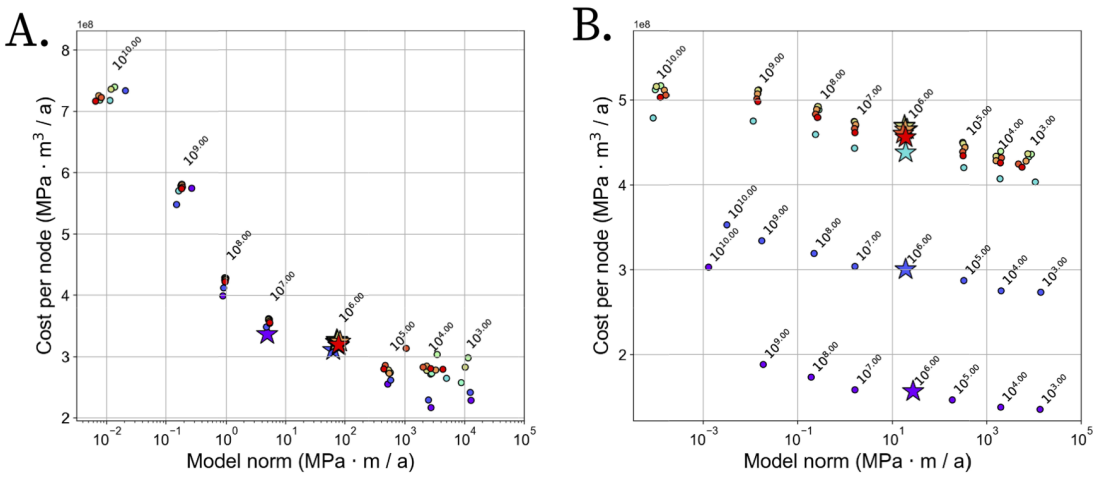

Figure B.6: The Tikhonov regularization curves (cost function plotted against the mean square gradient of beta for $\log_{10}\lambda = 10e^3, 10e^4, 10e^5, \ldots 10e^{10}$) for the (A) lower Thwaites and the (B) upper Thwaites grids where rainbow colors indicate model grid resolution (purple is highest resolution, blue second highest, etc.). Between $10e^6$ and $10e^7$, the cost function increases dramatically, and the L-curve method would select a value in this range as the appropriate regularization parameter (indicated with a star). For both the lower Thwaites and upper Thwaites grids, the highest resolution model domain minimizes the most cost per node.

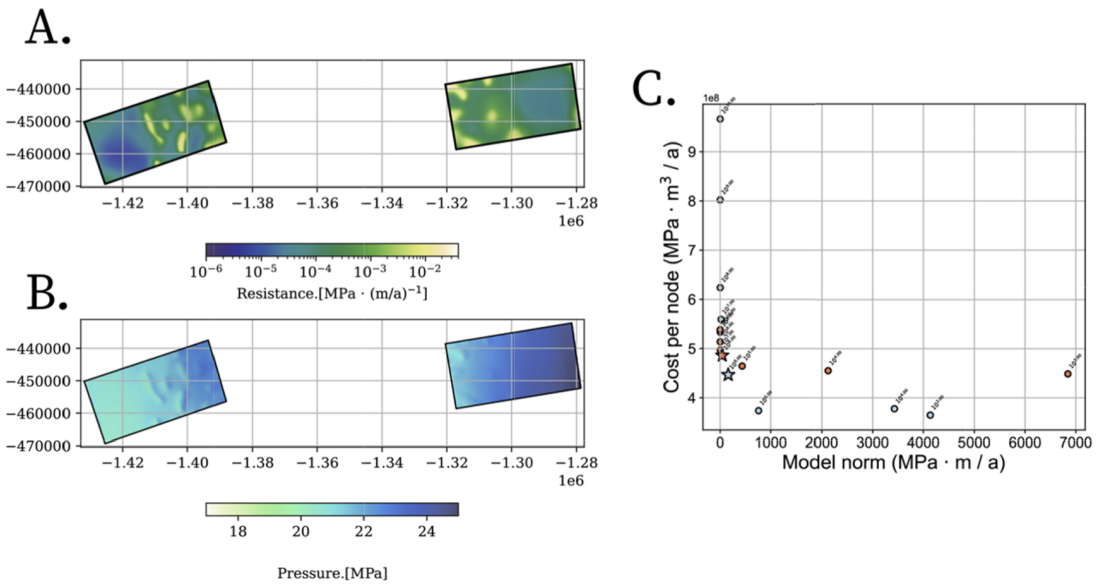

Figure B.7: (A) The basal resistance fields, (B) the normal pressure fields and the (C) Tikhonov regularization curves (cost function plotted against the mean square gradient of beta for $\log_{10}\lambda = 10e^3, 10e^4, 10e^5, \ldots 10e^{10}$) for the lower Thwaites (light blue) and the upper Thwaites (coral) flat grids. Again, near $10e^6$ the cost function increases dramatically, and the L-curve method would select a value in this range as the appropriate regularization parameter (indicated with a star). The fields in (A) and (B) are the fields associated with this choice of regularization. The cost per node for both simulations were 15% (lower Thwaites) and 5% (upper Thwaites) greater than the most isotropically smoothed experiments.

Table B.1: Table of model parameters used across all full-Stokes simulations.

Parameter	Value	Units	Description
A_0	$3.985e^{-13}$	$\text{MPa}^{-3}\cdot\ \text{yr}^{-1}$	Spatially uniform rate factor
Q	$60e^3$	J	Spatially uniform activation energy (Cuffey and Paterson, 2010)
R	8.314	$\text{J/mol}\cdot\text{K}$	Ideal gas constant
λ	$10e^6$	-	Tikhonov regularization coefficients
n	3	-	Glen's flow law exponent
m	1	-	Basal sliding relation exponent

Appendix C

SUPPLEMENT OF "LATE HOLOCENE STABILIZATION OF CONWAY ICE RIDGE"

C.1 Radar attenuation and corrected bed-returned power

We cannot directly measure ice temperature, fabric, or damage using radar data. We can calculate attenuation rates, which are linked to ice temperature, englacial chemistry, and the englacial reflector geometry. We empirically correct power for geometric spreading and englacial attenuation. Following many other authors (Bogorodsky et al., 1985; Winebrenner et al., 2003; Jacobel et al., 2009; Matsuoka et al., 2012; MacGregor et al., 2015; Christianson et al., 2016b; Hills et al., 2020), we use a simplified form of the radar power equation to describe the radar returned power in terms of its constitutive components:

$$P_r = P_t \frac{A^2 R q}{4\pi(2z)^2 B} e^{-2\alpha z} \tag{C.1}$$

where P_r is the power recorded at the receiver antenna, P_t is the transmitted power, A is the antenna gain, R is the power reflection coefficient, q is refractive focusing, z is the one-way travel path to the reflector of interest, B is birefringence losses, α is the dielectric absorption coefficient (attenuation cofficient), and $4\pi(2z)^2$ is spherical spreading, which assumes the target is large relative to the first Fresnel zone. If we assume the source and near surface terms (refractive focusing) do not vary spatially, we can group them as one source term $S = P_t A^2 q$. Then if we correct the received power for spherical spreading, $P_c = P_r 4\pi(2z)^2$, neglect birefringence losses for which corrections require polarimetric radar data unavailable for this site (Fujita et al., 2006; Matsuoka et al., 2009b), and linearize the equation in log-space (decibels, [dB]), we have:

$$[P_c] = [S] + [R] - 2Nz \tag{C.2}$$

where $[X] = 10\log_{10}(X)$ and $N = \alpha(10\log_{10}(e))$ is the one-way attenuation rate in

dB/km (Winebrenner et al., 2003).

Following equation C.2, we can use linear regression to determine the englacial attenuation rate if we correct the returned power for spherical spreading, assume that the source terms do not vary, and assume that each reflector has a power reflection coefficient (R) that is not spatially variable and that reflectivity does not vary between reflectors. Here, we conduct two regressions. First, we fit all reflectors within a moving depth-constrained vertical windows (100 m) that does not span the entire ice thickness. This results in depth-variable (or interval) attenuation rate. Second, we extract the bright reflectors (reflectors with P_c in the top 10% of all received data in a moving depth-constrained vertical window, again 100 m) throughout the entire ice column and calculate the attenuation rate using a single linear regression through the full ice thickness (Matsuoka et al., 2010). We choose bright reflectors here because they are more likely to be representative of true dielectric constants in the ice, especially deeper in the column where signal-to-noise ratio is low (Matsuoka et al., 2010). For both methods, we define the full thickness as ∼100 m below the surface to 85% of the ice thickness to avoid the direct arrival and low signal-to-noise deep in the ice column.

Radar attenuation results are difficult to interpret because they may include processes that reduce the amplitude of the radar wave that are not associated with radar attenuation, including destructive interference and backscatter from steeply sloping layers that is not incident upon the receiving antenna. For these data, trends in attenuation rates are not constant between the two field seasons, suggesting that they may be related to data quality and confounding issues listed above rather than physical properties, such as ice temperature or chemistry. In the 2001–2002 data, apparent low attenuation rates are often a result of low signal-to-noise ratios in the radar data, i.e., there simply are few or no bright reflectors present. Radar quality, especially deeper layer resolution, are substantially improved in the 2003–2004 field season compared to earlier data, so we focus interpretation on these data. Despite these improvements, many signals in the data are related to bright layer packets, layer slopes, and lack of signal due to deformed layers. Thus, we are hesitant to interpret attenuation results as indicative of ice temperature variability. We are similarly hesitant to interpret corrected bed power because it relies on accurate determination of attenuation. For data collected in the 2003-2004 field season, attenuation rates appear to be

higher on the north side of the ridge and lower on south side. This result is mainly due to more disrupted layers on the north side of the ridge due to more disrupted layers, which is consistent with more recent rapid flow on this portion of the ridge. We applied attenuation rate and geometric spreading corrections to bed returned power, but did not find patterns in the data that could be separated from attenuation rates signals, which we do not interpret for the same reasons we are hesitant to interpret attenuation rates.

C.2 Bed roughness

We use a discrete Fourier transform to determine the spectral power associated bed topography as a function of wavelength. Specifically, we calculate the discrete Fourier periodogram to determine the power associated with each constituent wavelength of topography:

$$P(k_x) = \frac{1}{N_x^2}|Z(k_x)|^2 \tag{C.3}$$

where

$$Z(k_x) = \sum_{n=0}^{N_x-1} z(n\Delta x)e^{-2\pi i \frac{k_x n}{N_x}}. \tag{C.4}$$

$Z(k_x)$ is the discrete Fourier transform of a data set $z(x)$, in this case depth to the bed, x is along-track distance, n is an index in z, and the transform has N_x evenly sampled nodes in frequency space at wavenumbers (spatial frequencies) k_x. Our processing follows the workflow of Booth et al. (2009) for spectral analysis of high-resolution topographic data. It is similar to other implementations in glaciology (Taylor et al., 2004; Bingham and Siegert, 2007), but our workflow uses different window sizes, more high-resolved bed data, and can be organically extended to multiple dimensions. We use the sum of the periodogram over all wavenumbers to represent the total energy associated with bed roughness at the center of each moving window. We note that we can also filter the energy by wavelength to sample frequency bands by only summing periodogram components for a subset of wavenumbers. We apply this discrete Fourier transform in a moving 1000-m window. We first detrend the data, apply a Hann window to minimize spectral leakage, set the DC-component to be zero to account for any offsets due to applying the Hann window, and then scale the

output periodogram so that the sum of the periodogram equals the variance of the detrended windowed elevation sample to correct for any reduction in variance caused by the windowing. This results in a spatially-distributed map of the total bed roughness power, which we plot at the center coordinates for each of the moving windows in every radar profile (Fig. 5.8b, C.2).

C.3 Analytic velocity calculations

C.3.1 Deformation velocity

If we assume that the bed-parallel shear stress is the dominant deformation mechanism in the ice column and equate the basal shear stress to the gravitational driving stress at the ice-sheet base, we can write the along-flow surface velocity (u_{surf}) as (Cuffey and Paterson, 2010):

$$u_{surf} = \frac{2A\tau_d^n h}{n+1} = \frac{A}{2} h \tau_d^3 \tag{C.5}$$

where $A = 3.5 \times 10^{-25}$ Pa^{-3}yr^{-1} is the rheological constant for an ice column with a mean temperature of -10°C, $n = 3$ is the flow law exponent, h is the ice thickness, and $\tau_d = \rho g h \sin\theta$ is the gravitational driving stress, with ice density $\rho = 917$ kg/m^{-3}, $g = 9.81$ m/s^2 , and surface slope θ. We use the velocity field of Joughin et al. (2002) to extract flowlines centered on each GNSS stake position that are 5 km long. Along each extracted flowline, we linearly interpolate surface elevation and ice thickness at 100 m intervals from BedMachine Antarctica (Morlighem et al., 2020). We calculate slope along the flowline using a robust linear regression (minimizing the L1-norm) and calculate average thickness using the arithmetic mean. Deformation velocities are then calculated following Equation C.5.

C.3.2 Strain rates

We calculated strain rates following the standardized implementation of Alley et al. (2018). This work applies the definition of the surface strain rate tensor given by Nye (1959) and the rotation to the local flow direction from Bindschadler et al. (1996). Input for the strain rate calculations was the Cartesian velocity fields in a polar stereographic projection (EPSG:3031)

provided by Joughin et al. (2002). Strain rates in the local flow direction (longitudinal, shear, and transverse) are plotted in Figure C.4.

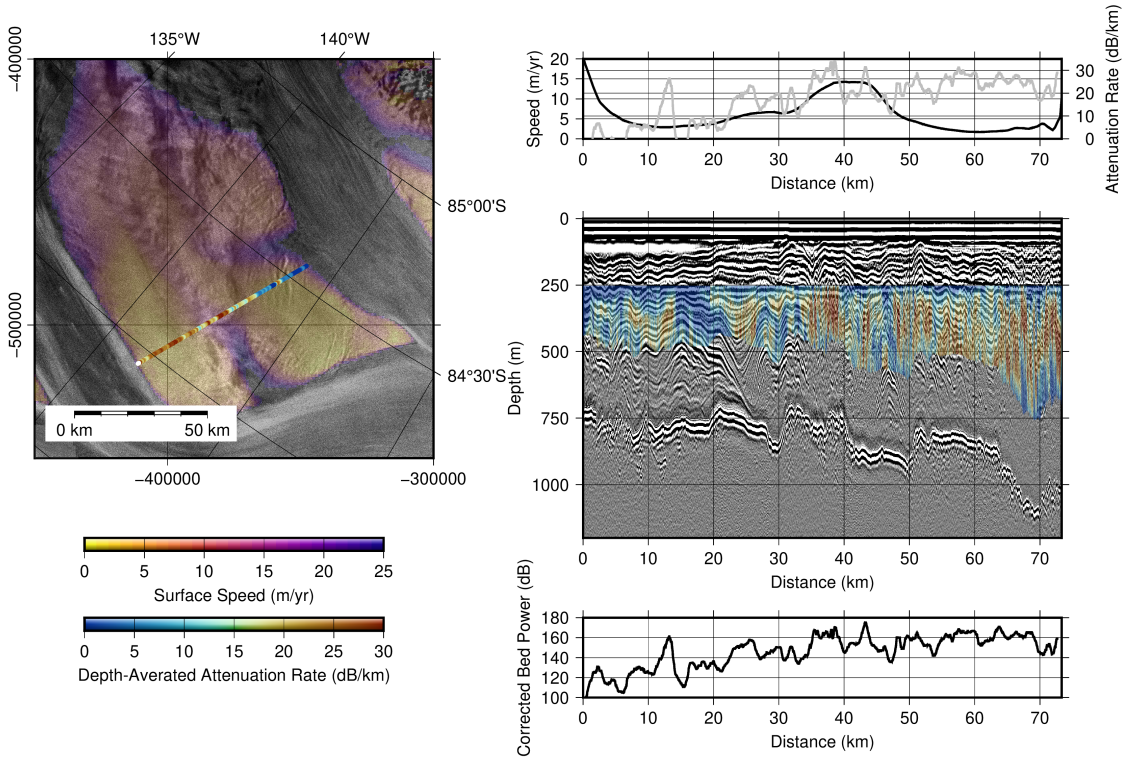

Figure C.1: Attenuation rate and bed reflectivity along northern radar profile across Ridge A.

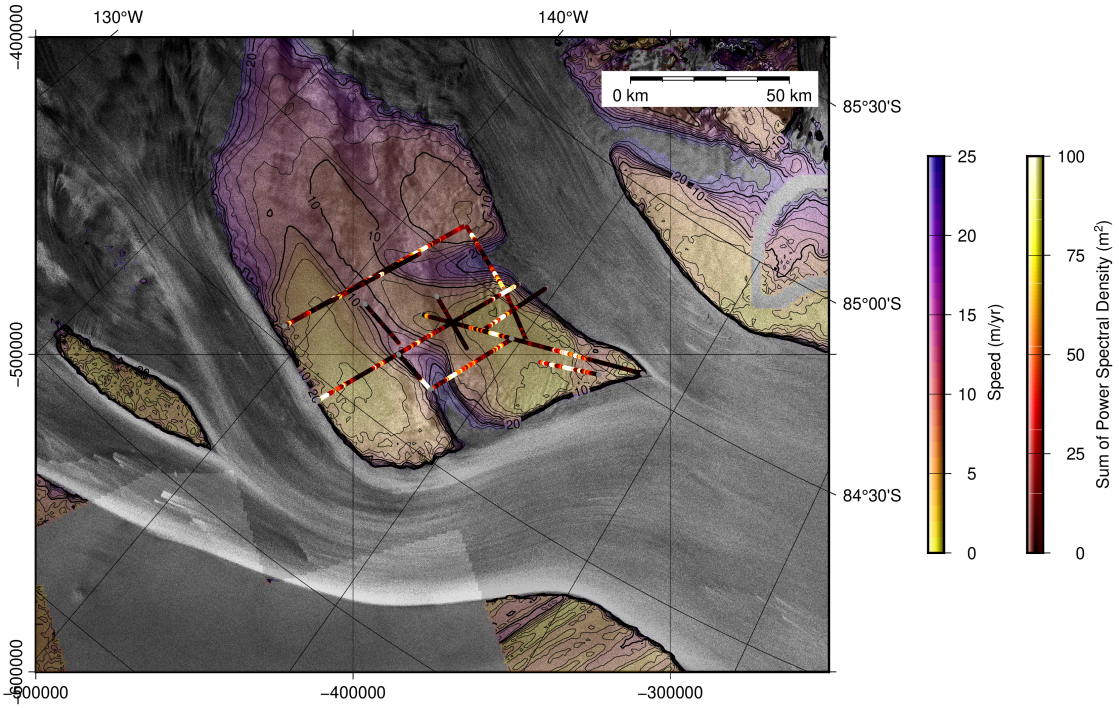

Figure C.2: Map of sum of power spectral density across all wavelengths in 1000-m moving window for the entire Conway Ridge radar survey plotted over SAR velocity data (Joughin et al., 2002) and RADARSAT-1 SAR imagery (Jezek, 1999; Jezek et al., 2013). Velocity contours (black) are plotted with a 2 m/yr interval. Velocities above 25 m/yr and grounding lines are masked in the velocity field.

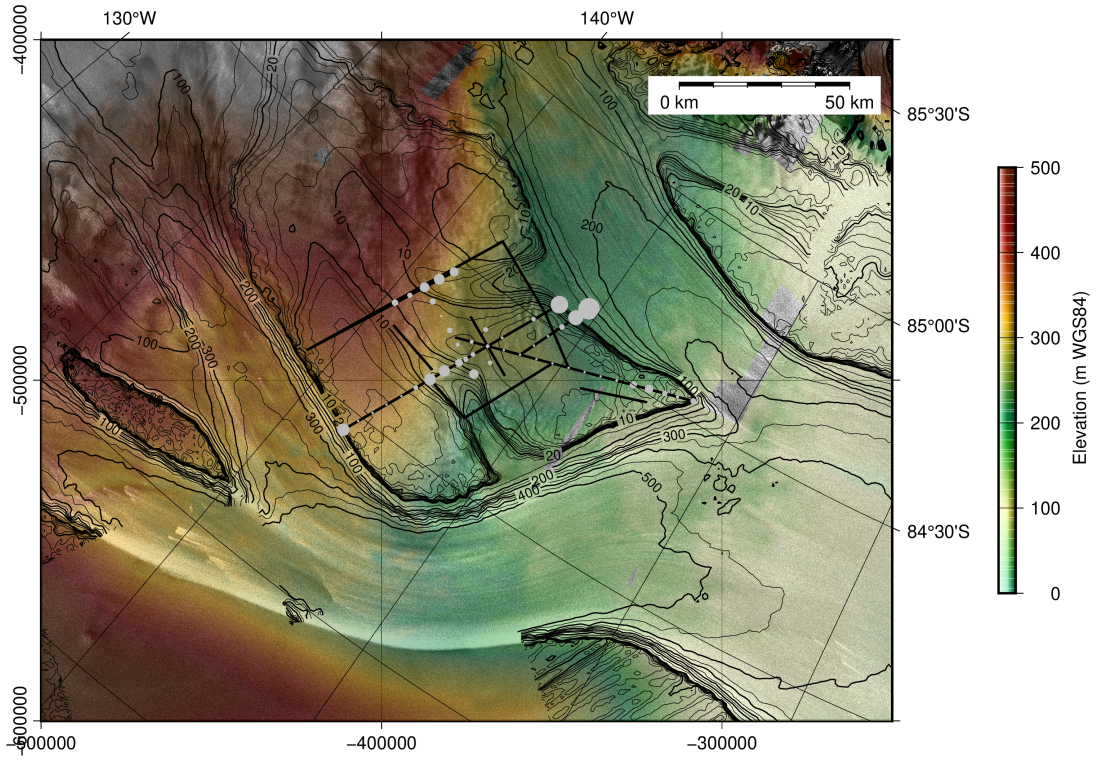

Figure C.3: Difference between measured velocity and analytic deformation velocity (gray dots, larger sizes indicate larger differeces, i.e., faster flow than expected from deformation) at GNSS stakes. Dot sizes are limited to velocity differences between 0.2 and 20 m/yr. Background imagery is RADARSAT-1 mosaic and Reference Elevation Model of Antarctica elevation. Black lines mark radar profiles. Contours represent ice speed. Speed contour interval is 2 m/yr below 25 m/yr speeds and 50 m/yr above 25 m/yr speeds.

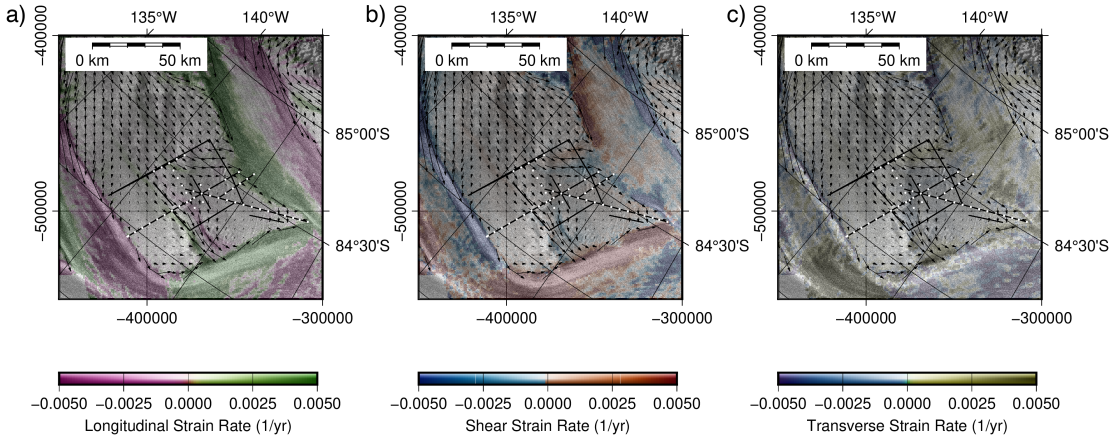

Figure C.4: Analytic calculations of strain rates using veocity fields of Joughin et al. (2002). A) Longitudinal, b) shear, and c) transverse strain rates plotted over RADARSAT-1 SAR mosaic (Jezek, 1999; Jezek et al., 2013). Vectors are the velocity field from Joughin et al. (2002). Black lines indicate locations or radar profiles and white dots mark locations of GNSS stakes.

Appendix D

SUPPLEMENT OF "INLAND MIGRATION OF PINE ISLAND AND THWAITES GLACIER SURFACE CREVASSES IN THE AMUNDSEN SEA EMBAYMENT"

D.1 Inland crevasse position back-tracing

The flow history of the inland crevasses we observe on Thwaites Glacier were back-traced using an interpolated average surface velocity when the largest Thwaites lake was most recently empty (2015-2017). Implicit in the back-tracing approach is the assumption that any change in the morphology of these crevasses is due to advection and not fracture development due to changes in stress accumulated as the features advected from where they formed. We present the particle flow paths with positions associated with the only documented drainage of Thwaites Lake 124 (Smith et al., 2017) in addition to positions dating back 60 years.

D.2 Plotting of principal surface stress failure envelopes

Surface observations of ice motion can be used to determine strain rates, and strain-rate measurements can be converted to stress using a constitutive relation. Nye (1959) outlined the method for conversion from surface strain rates to surface stress in one of the first applications of the constitutive relation for snow and ice. Here, we briefly summarize this calculation with some changes in convention following more recent authors and choose a form that is defined in terms of effective viscosity that could be used for either ice and firn (Vaughan, 1993; Bindschadler et al., 1996; Veen, 1999; Alley et al., 2018).

Assuming a two-dimensional Cartesian coordinate system, the magnitudes of the principal surface strain rates are related to the directional surface strain rates by (Nye, 1959):

$$\dot{\epsilon}_{1surf} = \frac{1}{2}\left(\dot{\epsilon}_x + \dot{\epsilon}_y\right) - \sqrt{\frac{1}{4}\left(\dot{\epsilon}_x - \dot{\epsilon}_y\right)^2 + \dot{\epsilon}_{xy}^2} \tag{D.1}$$

$$\dot{\epsilon}_{2surf} = \frac{1}{2}\left(\dot{\epsilon}_x + \dot{\epsilon}_y\right) + \sqrt{\frac{1}{4}\left(\dot{\epsilon}_x - \dot{\epsilon}_y\right)^2 + \dot{\epsilon}_{xy}^2} \tag{D.2}$$

where we have assigned the first principal strain rate as the larger principal strain rate. The measured principal surface strain rates can then be used to calculate the principal surface stress magnitudes following Glen's flow law (Nye, 1959; Vaughan, 1993; Veen, 1999):

$$\sigma_{1surf} = 2\eta\dot{\epsilon}_{1surf} + \eta\dot{\epsilon}_{2surf} \tag{D.3}$$

$$\sigma_{2surf} = \eta\dot{\epsilon}_{1surf} + 2\eta\dot{\epsilon}_{2surf} \tag{D.4}$$

where $\eta = \frac{1}{2}A^{-1/n}\dot{\epsilon}_e^{-(n-1)/n}$ is the effective viscosity of the ice, $\dot{\epsilon}_e$ is the effective strain rate, and $n = 3$ is the flow law exponent. A is the temperature (and likely flow-history) dependent creep parameter; here we set $A = 5.2 \times 10^{-25}$ s^{-1} Pa^{-3}, which is appropriate for ice at a temperature of -10°C (Cuffey and Paterson, 2010). Alternatively, we can consider any one of a number of constitutive relations for firn (Ambach and Eisner, 1986; Ambach et al., 1993, 1995; Arthern et al., 2010; Morris and Wingham, 2014). Many of these relations depend on parameters that are unknown for this study, namely firn density and temperature depth profiles and rate parameters. We choose an empirically determined firn shear viscosity of 4.9×10^9 KPa s from measurements of polar firn in Greenland at a temperature of -10°C and density of 700 kg/m^3 (Haefeli, 1967).

By the von Mises failure criterion, if

$$\sigma_t^2 < \sigma_{1surf}^2 + \sigma_{2surf}^2 - \sigma_{1surf}\sigma_{2surf} \tag{D.5}$$

then crevassing should occur, where σ_t is the tensile strength to ice. We note that this failure criterion, depends critically on the value for the tensile strength of ice, which is temperature and flow history dependent. The conversion between surface strain rates and surface stresses has a similar temperature and flow history dependence through the effective

viscosity and flow law, but the temperature relationship is somewhat better established from both laboratory and field studies.

To evaluate the applicability of analytic failure theory, we create maps of the two principal surface stresses from the surface strain rates following the methods outlined above. We then plot crevasse locations as a function of surface stresses, where x-axis is the first principal stress and the y-axis is the second principal stress (Fig. 6.3). In this basis space, the tensile strength corresponding to the von Mises failure criterion should appear as an ovaloid curve that demarks crevassed pixels from uncrevassed pixels. We create crevasse failure maps for each quarter of data from 2015 to 2022 for Thwaites Glacier and plot the crevasse locations in the surface stress basis space (Fig. 6.3). The prominent ovaloid shape that is produced in this plot (we have not assumed this form) is roughly consistent with expectations from the von Mises criterion. The spread of values, however, suggest that assuming a single critical tensile strength is not appropriate.

D.3 Possible opening event during 2012 lake drainage

Heat maps of crevasse detection and effective stress indicate that crevassing on Thwaites Glacier is generally concentrated in areas where a critical stress threshold would predict crevasse formation (Fig. 6.3–6.4). Notable exceptions to this rule are three crevasses in the interior region of Thwaites Glacier. Throughout the time series, these three features remain in comparatively low effective stress environments compared to crevasses detected downstream (Fig. 6.1). Using the ice velocity from 2015–2017, we back-trace these features and identify the 2012 lake drainage event as a potential source mechanism for their formation. During cascading lake drainage events, such as the event observed in 2012, the static hydropotential routes water through a basin below a ridge that controls the downstream margin of Thwaites Lake 124. During the lake drainage event (4.6 years before the scene shown in Figure 6.1), the three inland Thwaites crevasses were located on the stoss side of a surface high, near a local maximum in the effective stress field. Though these features were not near the lake when it began to drain in 2012, we hypothesize that the drainage may have contributed to changes in stress that promoted the opening of these features. This could happen either via the observed downstream acceleration following the lake drainage event

or local changes in the interior basal resistance that evolved with the morphology of the subglacial hydrology system. These observations of inland crevasses should be considered in fieldwork safety planning in areas where effective stress approaches the yield strength of ice and locations where englacial stresses can change rapidly.